HU ISSN 1586–2070

JOURNAL OF COMPUTATIONAL AND APPLIED MECHANICS

A Publication of the University of Miskolc

VOLUME 3, NUMBER 1 (2002)

MISKOLC UNIVERSITY PRESS

HU ISSN 1586–2070

JOURNAL OF COMPUTATIONAL AND APPLIED MECHANICS

A Publication of the University of Miskolc

VOLUME 3, NUMBER 1 (2002)

MISKOLC UNIVERSITY PRESS

EDITORIAL BOARD

LOCAL EDITORIAL COUNCIL

T. CZIBERE, I. KOZÁK, I. PÁCZELT, G. PATKÓ, G. SZEIDL

Journal of Computational and Applied Mechanics, Vol. 3., No. 1., (2002), pp. 3–4

PREFACE

A professional life dedicated to Mechanics
Professor Gyula Béda is 70 years old

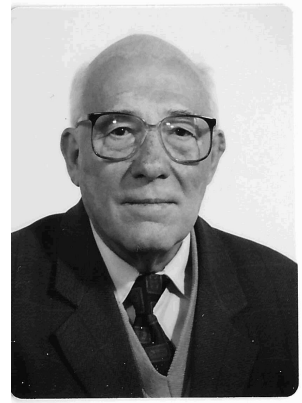

South of Budapest, by the Danube bank, in the small city of Ráckeve, the 3rd Finno-Ugric Conference on Mechanics had a Béda Session. This session was dedicated to my predecessor, Professor Gyula Béda, the former head of the Department of Applied Mechanics at the former Technical University of Budapest. In 2001, this conference gave the opportunity to celebrate his 70th birthday, when his colleagues, friends, former and present students gathered from Budapest, Miskolc, Bratislava, Vienna, Karlsruhe, Tallinn, Kiev, Blacksburg, Cleveland, and so on.

Professor Béda was awarded his degree in mechanical engineering in Miskolc in 1953, and started his academic carrier there, at the Department of Mechanics. Soon, he had become a promising young researcher in the famous Sályi-school at the Department of Mechanics. In 1967, he accepted a professorship at the Department of Applied Mechanics at the Technical University of Budapest, where he became the head of the department, in 1970. This led to substantial changes both in his professional life and in that of the department. The new theoretical approach introduced by him in teaching and research in Mechanics, like the application of tensor calculus or the theory of differential equations, met with the essential engineering traditions represented by the name of Professor Muttnyánszky, and the internationally most respected research work of Professor Reuss in plasticity. While he renewed all the basic courses in Mechanics from Statics to Vibrations, and introduced new courses like Continuum Mechanics and Analytical Mechanics, Professor Béda also started building a postgraduate school in the sense of the modern university structure of our present days.

When Professor Béda served as a Dean of the Faculty of Mechanical Engineering for 9 years, he had the opportunity and the courage to introduce a new specialization in mechanical engineering. With the aid of the Department of Mathematics, the so-called mathematical-engineering school selected the best students in mathematics with a definite interest in applying their knowledge in the hard-core problems of mechanical engineering. Through these undergraduate and doctoral students, he exerted an important influence on the mechanical engineering education in Budapest.

He served as a head of department for 25 years, and apart from the 9-year service as a dean, he also directed the mathematics departments for 8 years to lead them into a unified Institute of Mathematics in 1995. He was the leader of an academic research group on Continuum Mechanics till his recent retirement at the age of 70.

His best professional research results are related to Continuum Mechanics, but he is always open for discussion on basic theoretical problems in any field from fluid mechanics to thermodynamics – and his colleagues and students still use this openness either during lunchtime discussions or international seminars at the department. His 4 research books and 10 textbooks represent his activity, while the book Continuum Mechanics published in English with his respected colleagues and friends, Professor Kozák and Professor Verhás, has received a very positive feedback worldwide. The international reputation of his research activity is also represented by his membership in the ICF Council, conference and seminar invitations, and many other national professional institutions and journal editorial boards.

In the present issue of the journal, 6 papers are dedicated to Professor Gyula Béda. The scientific papers by P. Béda, S. R. Choi, J. P. Gyékényesi, I. Kozák, T. Szabó, I. Páczelt, A. Baksa, G. Stépán, S. Thangjitham and R. Heller were presented at the above mentioned conference to celebrate Professor Béda's 70th birthday. With this volume, all of his former and present students, colleagues an co-workers wish him good health and many more active years to come with research and education work at the university.

Gábor Stépán
Head of the Department of Applied Mechanics
Budapest University of Technology and Economics

Budapest, 6th June, 2002.

Journal of Computational and Applied Mechanics, Vol. 3., No. 1., (2002), pp. 5–13

A DYNAMIC THEORY OF MATERIAL INSTABILITY

Peter Béda
Research Group on the Dynamics of Machines and Vehicles
Hungarian Academy of Sciences and Budapest University of Technology and Economics
Műegyetem rkp. 3, 1111 BUDAPEST, Hungary

[Received: April 12, 2002]

Dedicated to my father, Professor Gyula Béda, on the occasion of his seventieth birthday

Abstract. In continuum mechanics dynamical effects are usually connected to waves. Such studies lead to the wave dynamical theory of constitutive equations. In stability analysis, the terms of the theory of dynamical systems are valuable tools. Most of the material instability investigations published deal with small deformations and static or quasi-static loading conditions. To study dynamical effects and finite deformations as well we need first of all appropriate constitutive equations. In order to take second gradient dependent materials widely used for numeric investigations of post-localization into account we shall assume that a jump exists in the derivative of the acceleration field and this singular surface propagates with finite velocities (generalized wave). From that assumption conditions are obtained for example for the second order derivatives of the variables of the constitutive equations. In material instability problems we prescribe that the loss of stability should be a generic one in terms of the theory of dynamical systems. There are two main points. Firstly, in the generic case the multiplicity of the critical eigenvalue should be one or at least finite, moreover the two basic types of stability loss should not be coexistent. Secondly, we would require a finite dimensional critical eigenspace. These lead to further conditions for the constitutive equations.

Mathematical Subject Classification: 74H14
Keywords: material instability, dynamical systems, finite deformations

1. Introduction

In recent years several new results of the theory of dynamical systems [1, 19] have already been successfully used in various fields of mechanics [7, 18]. This paper is to analyze material instability by considering solid continua as dynamical systems [6, 8]. This kind of investigation is closely related to perturbation analysis [8, 20]. In the theory of dynamical systems the definition of material stability/instability is based on the Lyapunov stability concept of the theory of dynamical systems (see [12] for details), for this reason we call it "dynamic material instability". The linear concept of the stability loss of a state of the system means that the real part of certain eigenvalues of the linear operator describing its behavior changes its sign.

The eigenvectors connected to them are called in applications the critical eigenmodes [9].

Unfortunately, for the classical setting [14, 15] it is not possible to obtain specific critical eigenmodes at the onset of material instability. On the other hand, in the finite element calculation of material instability problems the classical formulation of the basic equations of solid continua results in a definite mesh dependence [11, 16, 17]. These are very similar phenomena. In those papers mesh dependence was eliminated by the inclusion of rate dependence or nonlocality (second gradient effects) into the constitutive equations. Most of the investigations published deal with small deformation and static or quasi-static loading conditions. If dynamical effects are to be taken into account, we need appropriate constitutive equations. Such materials were studied by postulating the existence of a (second order) acceleration wave with finite wave speed [2]. This approach is called the wave dynamical theory of constitutive equations [3, 4, 6]. However, such constitutive theory based on second order waves cannot treat the cases of non-locality like second gradient materials [11, 20].

The aim of the paper is to study non-local material instability problems in case of finite deformation. We assume for the solid body that a generalized wave exists in the derivative of the acceleration field and this singular surface propagates forwards and backwards with finite velocities. From that assumption conditions are obtained for the second order derivatives of the variables of the constitutive equations [5]. Additionally we prescribe that the loss of stability should be a generic [1] one in terms of the theory of dynamical systems [19], which is essential in dealing with instability problems. There are two main points here. One is quite practical: a numerical solution of the material instability problems in the non-generic case may suffer serious technical difficulties (loss of convergence, mesh sensitivity [11] etc.). The other is of theoretical significance. By modelling physical phenomena we should have a set of equations which is typical (or generic), that is, differs only a little from the "exact unknown mathematical model".

The second section presents the set of the fundamental equations of the solid continuum assuming large deformations. It consists of the Cauchy equations of motion, the kinematic equation (for large displacements) and the constitutive equations. Such physically objective quantities are the Lie derivative of the stress gradient tensor, the Lie derivative of the (Euler) strain gradient tensor and the second covariant derivative of the stress and strain tensors.

In the next section we perform a material instability investigation for finite displacements with an appropriate constitutive equation in a uniaxial case. In this section the wave speed equation is a scalar third order algebraic one and should have real nonzero solutions [2]. By using the dynamical systems theory we should have a generic behavior (as it is defined in the theory of dynamical systems [8]) at the loss of stability because of the aforementioned general modelling concept of physical phenomena. There are two different ways for the loss of stability of a dynamical system [18]. These are the so-called static and dynamic bifurcations and should be completely different phenomena.

2. The set of basic equations for finite deformations

First of all we need the equations of motion

$$t^{kp}_{\ ;p} + q^k = \rho \dot{v}^k, \qquad t^{kp} = t^{pk}\,. \tag{2.1}$$

Here, and in all further equations and expressions Roman indices run from 1 to 3.

For finite deformation

$$v_{ij} = L_v\left(a_{ij}\right), \tag{2.2}$$

where

$$L_v a_{ij} \equiv \dot{a}_{ij} + a_{ip} v^p_{\ ;j} + a_{pj} v^p_{\ ;i}\,.$$

The notations are: q^k denotes body force, ρ is mass density, $X^K_{\ ,p}$ is the deformation gradient, g_{pq}, G_{KL} are metric tensors in the current and the initial configurations, v^i and $v^i_{\ ;j}$ are velocity and velocity gradient, v_{ij} is the deformation rate tensor. Cauchy stress tensor is denoted by t^{pk} and

$$a_{ik} = \frac{1}{2}\left(g_{ik} - X^K_{\ ,i} X^L_{\ ,k} G_{KL}\right)$$

denotes Euler strain tensor, respectively. A semicolon means covariant derivative and an overdot indicates material time derivative:

$$\dot{v}^i = \frac{\partial v^i}{\partial \tau} + v^k v^i_{\ ;k}$$

where τ denotes time. Note that the brackets used to distinguish Lie derivative can have upper and lower indices as in (2.2), we use them to show clearly for which variable it is applied. (For example $L_v\left(t^{kp}_{\ \ ;\ell}\right)$ is the Lie derivative of the covariant derivative of the stress tensor t^{kp} and not the covariant derivative of the Lie derivative.) Assume that the constitutive equation has the form

$$f_\alpha\left(L_v\left(t^{kp}_{\ \ ;\ell}\right), L_v\left(a_{ij;\ell}\right), t^{kp}_{\ \ ;\ell m}, a_{ij;\ell m}\right) = 0, \tag{2.3}$$

where $\alpha = 1, 2, \ldots, 6$. We use physically objective quantities such as

– the Lie derivative of the stress gradient tensor

$$L_v\left(t^{kp}_{\ \ ;\ell}\right) = \left(t^{kp}_{\ \ ;\ell}\right)^{\cdot} - t^{qp}_{\ \ ;\ell} v^k_{\ ;q} - t^{kq}_{\ \ ;\ell} v^p_{\ ;q} + t^{kp}_{\ \ ;q} v^q_{\ ;\ell}$$

– the Lie derivative of the (Euler) strain gradient tensor

$$L_v\left(a_{ij;k}\right) = \left(a_{ij;k}\right)^{\cdot} + a_{qj;k} v^q_{\ ;i} + a_{iq;k} v^q_{\ ;j} + a_{ij;q} v^q_{\ ;k}$$

– the second covariant derivative of the stress tensor $t^{kp}_{\ \ ;\ell m}$,
– the second covariant derivative of the strain $a_{ij;\ell m}$.

The set of equations (2.1), (2.2) and (2.3) has as many scalar variables as the number of equations in the set thus it can be considered to be the set of fundamental equations. We remark that the continuity equation for ρ can also be taken into account, but it is not necessary for the following calculations.

In the next section we perform several simplifications. One is the assumption that a uniaxial case is considered. Then, instead of the tensorial variables t^{pk}, a^{ij}, v^i, the scalar variables a, t, v can be used. They denote the first component (the x component) of the corresponding tensorial variables and depend obviously on x only. Additionally, we restrict the form of the constitutive equation to a quasi-linear one.

3. **Material instability in the uniaxial case**

Now we perform a material instability investigation of state S^0 of the solid body by considering finite displacements in the uniaxial case with an appropriate constitutive equation of type (2.3)

$$L_v\left(t_{,x}\right) + K_1 L_v\left(a_{,x}\right) + K_2 t_{,xx} + K_3 a_{,xx} = 0 \tag{3.1}$$

where partial derivatives of a function g are denoted by $g_{,x} = \frac{\partial g}{\partial x}$, or $g_{,\tau} = \frac{\partial g}{\partial \tau}$ and coefficients K_1, K_2, K_3 are considered to be piecewise constants. Let us substitute the uniaxial forms of the Lie derivatives into (3.1). After some rearrangements

$$\dot{t}_{,x} = t_{,x} v_{,x} - K_1\left(\dot{a}_{,x} + 3a_{,x} v_{,x}\right) - K_2 t_{,xx} - K_3 a_{,xx} \tag{3.2}$$

where the uniaxial material time derivatives are $\dot{v} = v_{,\tau} + v v_{,x}$ and $\dot{a} = a_{,\tau} + v a_{,x}$.

The wave dynamical theory of constitutive equations [4] leads to the following third degree polynomial equation

$$\rho c^3 - \rho K_2 c^2 - K_1(2a-1)c + K_3(2a-1) = 0, \tag{3.3}$$

which should have real nonzero wave-speed solutions c [2]. Assume that S^0 is described by values a_0, t_0, v_0 of the field variables. Then these values should satisfy the nonlinear system of fundamental equations formed by (3.2) and the uniaxial forms of (2.1) and (2.2):

$$\dot{v} = \frac{1}{\rho} t_{,x}, \quad \dot{a} = v_{,x} - 2a v_{,x}\,. \tag{3.4}$$

Lyapunov stability investigates the response of a mechanical system to arbitrary small perturbations, thus the perturbed quantities $a_0 + \Delta a, t_0 + \Delta t, v_0 + \Delta v$ should be substituted into (3.2) and (3.4). Note that the use of small perturbations is not a restriction in the sense of stability because of its local nature [12, 18, 19]. Having done the necessary calculations and by linearizing the set of equations (3.2) and (3.4) at S^0 a system of differential equations is obtained for the perturbations

$$\begin{aligned} v_{,\tau\tau} &= C_1 v + C_2 a_{,x} + C_3 a + C_4 v_{,x} + \\ &\quad + C_5 v_{,xx} + C_6 a_{,xx} + C_7 v_{,x\tau}\,, \\ a_{,\tau} &= D_1 v + D_2 a_{,x} + D_3 a + D_4 v_{,x} \end{aligned} \tag{3.5}$$

where Δ is omitted for the sake of simplicity and the following notations are used:

$$C_1 = -2v_{0,x\tau} - 2v_{0,xx}v_0 \ , \qquad C_2 = \frac{2K_1}{\rho}v_{0,x} \ ,$$
$$C_3 = \frac{2K_1}{\rho}v_{0,xx} \ , \qquad C_4 = \frac{2K_1}{\rho}a_{0,x} - K_2 \ ,$$
$$C_5 = v_0^2 - \frac{K_1}{\rho} + \frac{2K_1}{\rho}a_0 \ , \qquad C_6 = -\frac{K_3}{\rho}, C_7 = 2v_0 \ ,$$
$$D_1 = -a_{0,x} \ , \qquad D_2 = -v_0 \ , \qquad D_3 = -2v_{0,x} \ , \qquad D_4 = -2a_0 + 1 \ .$$

Let us introduce new variables $y_1 = a, y_2 = v, y_3 = v_{,\tau}$ a vector $y = [y_1, y_2, y_3]$ and an operator

$$\mathbf{H} := \begin{bmatrix} H_1 & H_2 & 0 \\ 0 & 0 & 1 \\ H_3 & H_4 & H_5 \end{bmatrix},$$

where the elements

$$H_1 = D_2\frac{\partial}{\partial x} + D_3, \qquad H_2 = D_4\frac{\partial}{\partial x} + D_1, \qquad H_3 = C_6\frac{\partial^2}{\partial x^2} + C_2\frac{\partial}{\partial x} + C_3,$$
$$H_4 = C_5\frac{\partial^2}{\partial x^2} + C_4\frac{\partial}{\partial x} + C_1, \qquad H_5 = C_7\frac{\partial}{\partial x}$$

are differential operators. Then a dynamical system

$$\frac{\partial}{\partial \tau}y = \mathbf{H}y. \tag{3.6}$$

can be attached to (3.5) [8]. The characteristic equation of (3.6) reads

$$\lambda y = \mathbf{H}y. \tag{3.7}$$

and the linear Lyapunov stability condition of state S^0 is: $\mathrm{Re}\lambda \leq 0$ for all eigenvalues of (3.7). Stability boundary is at $\mathrm{Re}\lambda = 0$. The loss of stability can be classified as a static bifurcation (or divergence) type instability ($\mathrm{Re}\lambda = 0$, $\mathrm{Im}\lambda = 0$) or a dynamic one ($\mathrm{Re}\lambda = 0$, $\mathrm{Im}\lambda \neq 0$) [12]. To find the eigenvalues of equation (3.7) requires the solution of a boundary value problem, which may cause serious difficulties and needs numerical computations.

To continue using analytic methods we should perform simplifications: the use of small periodic perturbations. While stability is considered here as a local property of a state the small perturbation technique is quite obvious, but not its periodicity. It is really a restriction, but used widely in the engineering literature of the linear case [20]. (A detailed study on that restriction is presented in [8].) While perturbations are small, $a_\tau = v_x$ and then equations (3.5) can be transformed into the velocity field,

$$v_{,\tau\tau\tau} = C_1v_{,\tau} + C_2v_{,xx} + C_3v_{,x} + C_4v_{,x\tau} + C_5v_{,xx\tau} + C_6v_{,xxx} + C_7v_{,x\tau\tau} \ ,$$
$$v_{x\tau} = D_1v_{,\tau} + D_2v_{,xx} + D_3v_{,x} + D_4v_{,x\tau} \ . \tag{3.8}$$

By assuming periodic perturbations

$$v = \exp(i\omega x) \tag{3.9}$$

in a similar way as it was done in the general case with (3.7) the characteristic equation results in a set of algebraic equations

$$\begin{aligned} \lambda^3 &= C_1\lambda - C_2\omega^2 - C_5\omega^2\lambda^2\,, \\ 0 &= C_3 + C_4\lambda - C_6\omega^2 + C_7\lambda^2\,, \\ 0 &= D_1\lambda - D_2\omega^2\,, \\ \lambda &= D_3 + D_4\lambda\,, \end{aligned} \tag{3.10}$$

and the static bifurcation condition is the existence of a $\lambda = 0$ solution of (3.10). Then we obtain the following relations

$$D_3 = 0, \iff \frac{\partial v_0}{\partial x} = 0, \tag{3.11}$$

$$D_2 = 0, \iff v_0 = 0, \tag{3.12}$$

$$C_2 = 0, \iff K_2\frac{\partial v_0}{\partial x} = 0, \tag{3.13}$$

and finally equations

$$C_3 = 0, \iff K_1\frac{\partial^2 v_0}{\partial x^2} = 0, \tag{3.14}$$

and

$$C_6 = 0, \iff K_3 = 0, \tag{3.15}$$

or

$$C_3 - C_6\omega^2 = 0, \iff 2K_1\frac{\partial^2 v_0}{\partial x^2} + K_3\omega^2 = 0, \tag{3.16}$$

should be satisfied. Obviously (3.11) implies (3.13), thus there is a static bifurcation if

A: (3.11), (3.12), (3.14) and (3.15), or
B: (3.11), (3.12), and (3.16) are valid.

Case **A** does not meet the conditions originated by wave dynamics: there is a zero wave speed solution c of (3.3). If $K_3 = 0$ from (3.15) is substituted into (3.3)

$$\left(\rho c^2 - \rho K_2 c - K_1(2a-1)\right)c = 0$$

is obtained thus $c = 0$ is a solution. In the classical material instability concept [14, 15] it means localization. On the other hand, if (3.15) holds, the constitutive equation (3.1) has no second strain gradient dependent term, which corresponds to the fact that there is a stationary singular surface (a localization zone of zero width). Thus we have exactly the classical result of Rice [15]. However, in case **B** from equation (3.16)

$$\omega^2 = -\frac{2K_1}{K_3}\frac{\partial^2 v_0}{\partial x^2},$$

if $\frac{2K_1}{K_3}\frac{\partial^2 v_0}{\partial x^2} < 0$. This means that there is a critical eigenfunction to the zero eigenvalue, that is, we have a critical periodic perturbation (3.9)

$$v_{cr} = \exp\left(ix\sqrt{-\frac{2K_1}{K_3}\frac{\partial^2 v_0}{\partial x^2}}\right)$$

at which state S^0 undergoes a static bifurcation.

Let us now study the dynamic bifurcation case. Then we need $\lambda^2 < 0$ solution of equation (3.10). The conditions are (3.11), (3.12) and

$$C_5 = 0 \iff v_0^2 - \frac{K_1}{\rho} + \frac{2K_1}{\rho}a_0 = 0\,, \tag{3.17}$$

$$C_4 = 0 \iff \frac{2K_1}{\rho}a_{0,x} - K_2 = 0\,, \tag{3.18}$$

$$D_1 = 0 \iff a_{0,x} = 0\,, \tag{3.19}$$

$$D_4 = 1 \iff a_0 = 0\,. \tag{3.20}$$

Then from (3.17), (3.12) and (3.20)

$$K_1 = 0, \tag{3.21}$$

and from (3.18) and (3.19)

$$K_2 = 0. \tag{3.22}$$

Moreover, the second equation of (3.10) and (3.18) with (3.12) imply (3.15)

$$K_3 = 0.$$

Finally from the first equation of (3.10) substituting (3.12), (3.11) and (3.17) we have

$$\lambda^2 = -2\frac{\partial^2 v_0}{\partial x \partial \tau} \tag{3.23}$$

thus there is a dynamical bifurcation if conditions (3.11), (3.12), (3.15), (3.19), (3.20), (3.21), (3.22) are satisfied and

$$\frac{\partial^2 v_0}{\partial x \partial \tau} > 0. \tag{3.24}$$

Unfortunately this is not a generic dynamical bifurcation. We can easily see that (3.21) implies (3.14), consequently a dynamical bifurcation is coexistent with a static bifurcation of case **A**. Moreover, if (3.15), (3.21) and (3.22) are valid, equation (3.3) has a zero solution $c = 0$, that is, if at least one of conditions (3.19), (3.20), (3.22) or (3.24) fails (because then no coexistent dynamical bifurcation is present), we may speak about a stationary discontinuity as a static bifurcation type instability phenomenon. We remark that this result forms a bridge between the dynamical systems approach [8] and the wave dynamical theory because it can be obtained from both of them [10].

4. **Conclusions**

By using a second order constitutive equation of form (3.1) for finite deformations both types **A** and **B** of the static bifurcation instability are generic in the sense of dynamical systems theory because there is no coexistent dynamical bifurcation. Moreover, a nice (and useful [7]) property of the small deformation case of second strain gradient dependent materials was preserved: the dimension of the critical eigenspace at static bifurcation remains finite (case **B**). When this term (case **A**) is neglected, we cannot find a unique critical eigenfunction but a "stationary discontinuity": the jump (discontinuity surface in the higher derivatives of the field variables) stops at the conditions of instability.

Acknowledgement. This work was supported by the National Scientific Research Fund of Hungary (under contract OTKA T034535)

References

1. Arnold, V.I.: *Geometrical Methods in the Theory of Ordinary Differential Equations*, Springer, New York, 1983.
2. Béda, Gy.: *Methode zur Bestimmung der Materialgleichung*, Publ. of the Tech. Univ. for Heavy Ind., Miskolc, **12**, (1962), 271-286.
3. Béda, Gy.: *Possible constitutive equations of the moving plastic body*, Advances in Mech., **10**, (1987), 65-87.
4. Béda, Gy.: *Constitutive equations and nonlinear waves*, Nonlinear Analysis, Theory, Methods and Appl., **30**, (1997), 397-407.
5. Béda, Gy. and Béda, P.B.: *A study on constitutive relations of copper using the existence of acceleration waves and dynamical systems*, Proc. of Estonian Academy of Sci. Engin., **5**, (1999), 101-111.
6. Béda, P. B.: *Localization as instability of dynamical systems*, Material Instabilities, Eds.: R.C. Batra, H. Zbib, ASME Press, New York, 1994, 279-284.
7. Béda, P. B.: *Bifurcation and postbifurcation of rods*, Journal of Theoretical and Applied Mechanics, **34**, (1996), 91-100.
8. Béda, P. B.: *Material instability in dynamical systems*, European Journal of Mechanics, A/Solids, **16**, (1997), 501-513.
9. Béda, P. B.: *On rate and gradient dependence of solids as dynamical systems,* Arch. Mech., **51**, (1999), 229-241.
10. Béda, P. B. and Béda, Gy.: *Acceleration waves and dynamic material instability in constitutive relations for finite deformation,* Structural Failure and Plasticity, IMPLAST 2000, Eds.: X.L. Zhao and R.H. Grzebieta, Elsevier, Oxford, 2000, 585-590.
11. De Borst, R. Sluys, L.J., Mühlhaus, H-B. and Pamin, J.: *Fundamental issues in finite element analyses of localization of deformation*, Engineering Computations, **10**, (1993), 99-121.
12. Chetayev, N.G.: *The Stability of Motion*, Pergamon Press, New York, 1961.
13. Dobovsek, I.: *Adiabatic material instabilities in rate-dependent solids*, Arch. Mech., **46**, (1994), 893-936.

14. Hill, R.: *Acceleration waves in solids*, Journal of the Mech. and Phys. of Solids, **10**, (1962), 1-16.

15. Rice, J.R.: *The localization of plastic deformation, Theoretical and Applied Mechanics*, Ed.: W.T. Koiter, North-Holland, Amsterdam, 1976, 207-220.

16. Sluys, L.J.: *Wave propagation, localization and dispersion in softening solids*, Dissertation, Delft University of Technology, Delft, 1992.

17. Sluys, L.J. and De Borst, R.: *Wave propagation and localization in a rate-dependent cracked medium - model formulation and one-dimensional examples*, Int. J. Solids Structures, **29**, (1992) 2945-2958.

18. Troger, H. and Steindl, A.: *Nonlinear Stability and Bifurcation Theory, An Introduction for Scientists and Engineers*, Springer, Wien, New York, 1990.

19. Wiggins, S.: *Introduction to Applied Nonlinear Dynamical Systems and Chaos*, Springer, New York, 1990.

20. Zbib, H.M. and Aifantis, E.C.: *On the localization and postlocalization behavior of plastic deformation. I.* Res Mechanica, **23**, (1988), 261-277.

Journal of Computational and Applied Mechanics, Vol. 3., No. 1., (2002), pp. 15–26

EFFECT OF LOAD RATE ON ULTIMATE TENSILE STRENGTH OF CERAMIC MATRIX COMPOSITES AT ELEVATED TEMPERATURES

Sung R. Choi
Ohio Aerospace Institute
Brook Park, Ohio 44142, USA
Sung.R.Choi@grc.nasa.gov

John P. Gyekenyesi
National Aeronautics and Space Administration, Glenn Research Center
Cleveland, Ohio 44135 USA
John.P.Gyekenyesi@grc.nasa.gov

[Received: September 28, 2001]

Dedicated to Professor Gyula Béda on the occasion of his seventieth birthday

Abstract. Strength of three continuous fiber-reinforced ceramic composites, including SiC/CAS-II, SiC/MAS–5 and SiC/SiC, was determined as a function of test rate in air at 1100 to 1200 °C. All three composite materials exhibited a strong dependency of strength on test rate, similar to the behavior observed in many advanced monolithic ceramics at elevated temperatures. The application of the preloading technique as well as the prediction of life from one loading configuration (constant stress-rate) to another (constant stress loading) suggested that the overall macroscopic failure mechanism of the composites would be the one governed by a power-law type of damage evolution/accumulation, analogous to slow crack growth commonly observed in advanced monolithic ceramics. It was further found that constant stress-rate testing could be used as an alternative to life prediction test methodology even for composite materials, at least for a short range of lifetimes and when ultimate strength is used as the failure criterion.

Keywords: ceramic matrix composites, ultimate tensile strength, life prediction testing, slow crack growth/damage accumulation analysis

1. Introduction

The successful development and design of continuous fiber-reinforced ceramic composites (CFCCs) are dependent on a thorough understanding of basic properties such as fracture and delayed failure (slow crack growth, fatigue, or damage accumulation) behavior. Particularly, accurate evaluation of delayed failure behavior under specified loading/environment conditions is a prerequisite to ensure accurate life prediction of structural components.

This paper describes the effect of load rate on elevated-temperature ultimate tensile strength of three different Nicalon$^{\mathrm{TM}}$ fiber-reinforced ceramic composites. For

each composite material, strength was determined in air as a function of test rate at elevated temperature of 1100 ˚C (SiC/CAS and SiC/MAS) or 1200 ˚C (SiC/SiC). This type of testing, when used for monolithic ceramics, is called "constant stress-rate" or "dynamic fatigue" testing [1 to 3]. The loading rate dependency of strength was analyzed with the power-law (damage) propagation, conventionally utilized for monolithic ceramics and glass. Preloading tests were conducted to better understand the governing failure mechanism(s) of the materials. Finally, the result of elevated-temperature constant stress ("static fatigue" or "stress rupture") testing was obtained for each material and compared with that of constant stress rate testing. This was done to further verify the overall failure mechanism of the materials and to establish constant stress-rate testing as a means of life prediction test methodology for CFCCs. It should be noted that few studies on these subjects have been done for continuous fiber-reinforced ceramic composites at elevated temperatures, except some limited room-temperature study [4].

2. **Experimental procedure**

All the matrices of the three test composites were reinforced by ceramic-grade Nicalon^{TM} fibers with a fiber volume fraction of about 0.39. The nominal fiber diameters ranged from 10 to 15 μm. The three composite materials included Nicalon^{TM} unidirectionally (1D) fiber-reinforced calcium aluminosilicate (designated SiC/CAS-II), Nicalon^{TM} crossply (2D) magnesium aluminosilicate (designated SiC/MAS–5), and Nicalon^{TM} plain-woven (2D) silicon carbide composites. SiC/CAS-II and SiC/MAS–5 were fabricated by Corning, Inc., through hot-pressing followed by ceraming of the composites by a thermal process. The designation "–5" in SiC/MAS–5 indicates that the matrix was doped with 5 vol% fraction of borosilicate glass. The silicon carbide matrix in the SiC/SiC composites was fabricated by the DuPont Company through chemical vapor infiltration (CVI) into the fiber preform. SiC/CAS-II and SiC/MAS–5 laminates were 18 and 16 plies thick, respectively, with a nominal thickness of about 3 mm. The plain-woven laminates of the SiC/SiC composite were supplied in 12 plies (normally 3.5 mm) thick. More detailed information regarding the test composite materials can be found elsewhere [5]. The SiC/CAS-II material has been used in a previous, preliminary study on test rate-effect on tensile strength [6]. The dogboned tensile test specimens measuring 152.4 mm (length) × 12.7 mm (width) were machined from the composite laminates, with the gage section of about 30 mm long, 10 mm wide and 3.0 to 3.5 mm thick (as-furnished). The design of the dogboned tensile test specimen was the result of previous finite element analysis [7].

Monotonic tensile testing was conducted in air at 1100 ˚C for both SiC/CAS-II and SiC/MAS–5 and at 1200 ˚C for SiC/SiC, using a servohydraulic test frame (Model 8501, Instron, Canton, MA). A total of three to four different loading rates (in load control), corresponding to stress rates ranging from 50 to 0.005 MPa/s, were employed with typically 3 test specimens tested at each loading rate. Detailed experimental procedure on tensile testing and related induction-heating equipment can be found elsewhere [5]. Preloading or accelerated testing technique, applied primarily

to monolithic ceramics and glass [8,9], was also conducted at test temperatures using 0.5 MPa/s (for SiC/CAS-II) or 0.005 MPa/s (for SiC/MAS–5 and SiC/SiC) in an attempt to better understand the governing failure mechanism of the materials. Predetermined preloads, corresponding to about 80 to 90 percent of the failure strength determined at 0.5 or 0.005 MPa/s with zero preload (regular testing), were applied quickly to the test specimens prior to testing and their corresponding strengths were measured. Typically two to three test specimens were used in preload testing. Tensile testing was performed in accordance with ASTM Test Standard, ASTM C 1359 [10].

Constant stress ("static fatigue" or "stress rupture") tensile testing was also performed in air for the three composite materials using the same test specimen geometry, test fixture, test frame and same test temperatures that were used for monotonic tensile testing. The limited availability of test materials confined the testing to four to nine test specimens, depending on material. Four different static loads were applied to test specimens and their corresponding times to failure were determined.

3. **Results**

3.1. **Constant Stress-Rate Testing.** The results of monotonic tensile strength testing with different test rates are presented in Figure 1, where *ultimate strength* was plotted as a function of *applied stress rate* for each composite material using log-log scales. Each solid line in the figure indicates a best-fit regression line based on the log (*ultimate strength*) versus log (*applied stress rate*) relation. The decrease in ultimate strength with decreasing stress rate, which represents a susceptibility to damage accumulation or delayed failure, was significant for all the composite materials. The strength degradation was 51, 31 and 62 percent, respectively, for SiC/CAS-II, SiC/MAS–5 and SiC/SiC when the stress rate decreased from the highest to the lowest. Fracture patterns for the SiC/CAS-II composite showed some fiber pullout with jagged faceted matrix cracking often propagating along the test-specimen length, as shown in Figure 2(a). For a given stress rate, however, the difference in strength between different fracture patterns was not obvious. No appreciable difference in the mode of failure was observed for SiC/MAS–5 and SiC/SiC, where most specimens tested at either high or low stress rate exhibited relatively flat fracture surfaces (see Figure 2(b) and 2(c)), possibly called *brittle fracture*.

3.2. **Preload testing.** The results of preloading tests are also shown in Figure 1, where the ultimate strength with 80 to 90 percent preloads is compared with the regular testing results without preload. The difference in strength between the two preloads (0 and 80 to 90%) was negligibly small for each material: 211 MPa (no preload) and 209 MPa (for 85% preload) for SiC/CAS-II; 142 MPa (0 and 80% preload) for SiC/MAS–5; 77 MPa (no preload) and 80 MPa (90%) for SiC/SiC. Hence, the maximum strength difference, exhibited by SiC/SiC, was about 4 percent.

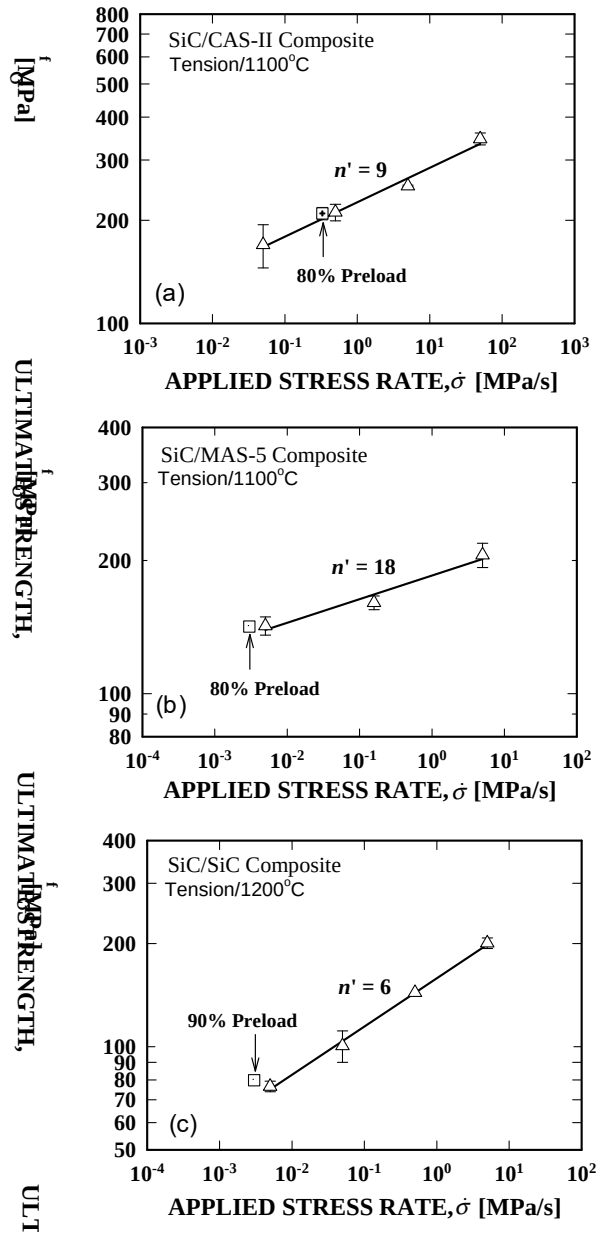

Figure 1. Results of ultimate tensile strength as a function of stress rate for (a) SiC/CAS II, (b) SiC/MAS 5, and (c) SiC/SiC composites at elevated temperatures in air. The solid lines represent the best-fit regression lines. Error bar indicates ±1.0 standard deviation. The results of preloading tests are also indicated.

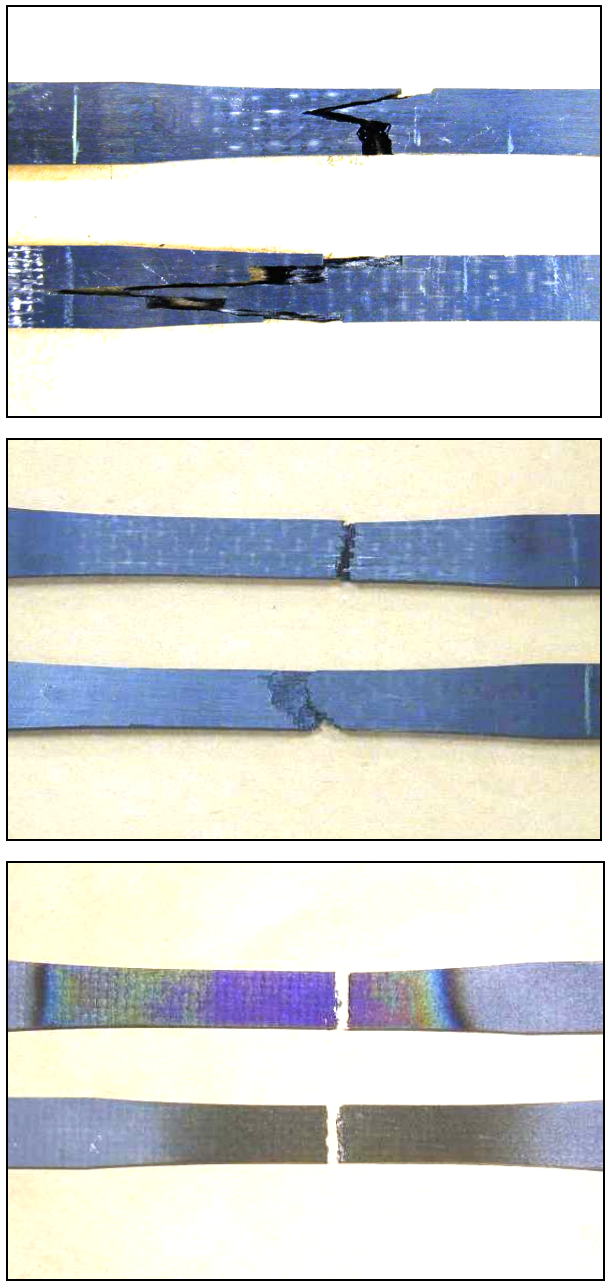

Figure 2. Fracture patterns for (a) SiC/CAS II, (b) SiC/MAS 5, and (c) SiC/SiC composites subjected to elevated temperature tensile testing. The upper and lower pictures for a given composite material indicate the specimen tested at the lowest and highest load rates, respectively.

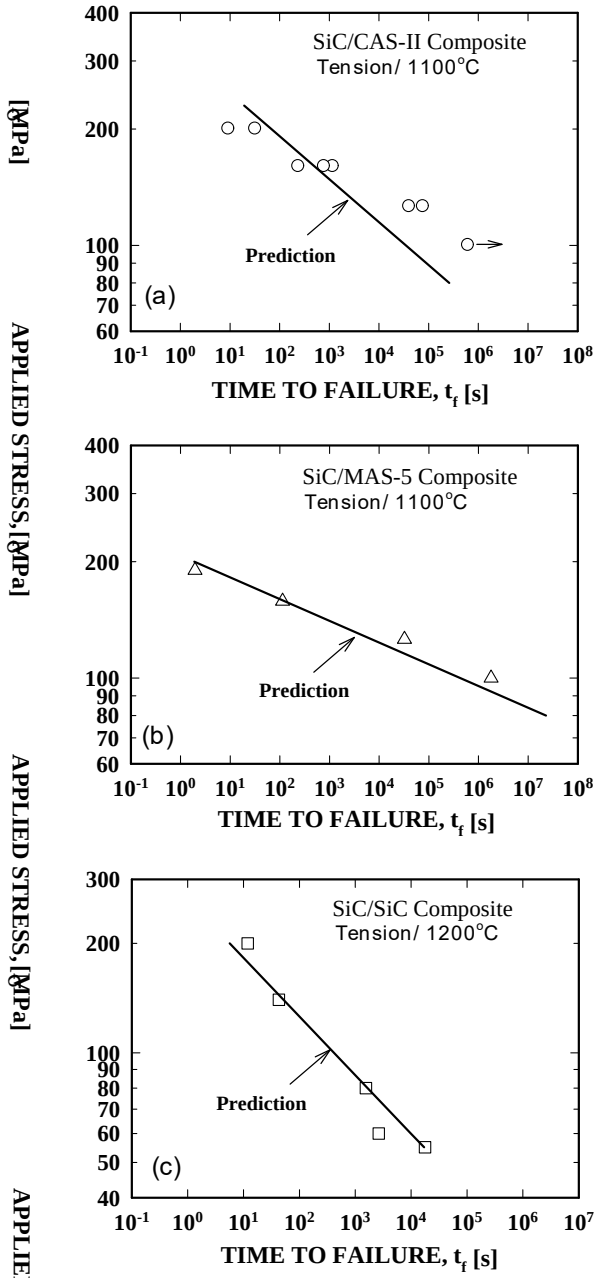

Figure 3. Results of constant stress ("static fatigue" or "stress rupture") testing for (a) SiC/CAS II, (b) SiC/MAS 5, and (c) SiC/SiC composites at elevated temperatures in air. The solid lines represent the predictions based on the results of constant stress rate testing (Figure 1).

This indicates that any significant damage that would control the ultimate strength of the material did not occur below the applied load level up to 80 to 90 percent of the fracture load. Conversely, the damage to control final failure would have occurred when applied load or test time was greater than 80 to 90 percent of fracture load or total test time. The theory explaining results of preload testing will be described in the discussion section.

3.3. **Constant stress ("stress rupture") testing.** A summary of results of constant stress or stress rupture testing at elevated temperatures is presented in Figure 3, where *time to failure* was plotted against *applied stress* for each composite material using log-log scales. A significant decrease in time to failure with increasing applied stress, which represents a susceptibility to damage accumulation or delayed failure, was evident for all the composite materials tested. Each solid line in Figure 3 indicates prediction results based on the constant stress-rate data (Figure 1), which will be discussed in a later section. The mode of fracture in constant stress testing was very similar to that in constant stress-rate testing. Brittle failure was exemplified for SiC/MAS–5 (2D) and SiC/SiC (2D), while somewhat jagged matrix cracking was observed for SiC/CAS-II (1D).

4. **Discussion**

The strength dependency on test rate exhibited by the three composite materials (Figure 1) is very similar to that observed in advanced monolithic ceramics at ambient or elevated temperatures. The strength degradation with decreasing stress rate has been known to be due to slow crack growth (delayed failure or fatigue) of an initial crack, typically governed by the following empirical power-law relation [1 to 3]:

$$\nu = A\,(K_I/K_{IC})^n \tag{4.1}$$

where v, K_I and K_{IC} are crack velocity, mode I stress intensity factor and fracture toughness, respectively. A and n are called slow crack growth (SCG) parameters. Based on this power-law relation, the strength (σ_f) can be derived as a function of applied stress rate ($\dot{\sigma}$) [1 to 3].

$$\sigma_f = D\,[\dot{\sigma}]^{\,1/n+1} \tag{4.2}$$

where D is another SCG parameter associated with inert strength, n and crack geometry.

Equation (4.2) can be expressed in a more convenient form by taking logarithms of both sides

$$\log \quad \sigma_f = \frac{1}{n+1}\ \log\ \dot{\sigma} + \log\ D \tag{4.3}$$

Constant stress-rate ("dynamic fatigue") testing based on Eqs. (4.2) or (4.3) has been established as ASTM Test Methods (C1368 [2] and C1465 [3]) to determine SCG parameters of advanced monolithic ceramics at ambient and elevated temperatures. It has been recommended to use units of MPa for σ_f nd MPa/s for [2 to 3]. As can be seen in Figure 1, the data fit to equation (4.3) is very reasonable with the correlation coefficients (r_{coef}) all greater than 0.980, indicating that the damage

evolution/accumulation or delayed failure of the composite materials would be adequately described by the power-law type relation, equation (4.1). Assuming this, the *apparent* parameters n' and D' for the composites were determined using a linear regression analysis based on equation (4.3) with the data in Figure 1. Values of n' = 9.0 and D' = 226, n' = 18 and D' = 185, and n' = 6 and D' = 158 were obtained for SiC/CAS-II, SiC/MAS–5 and SiC/SiC, respectively (The prime was used here for composite materials to distinguish them from monolithic ceramic counterparts.). It is noteworthy that the value of n', a measure of susceptibility to damage, was very low for both SiC/CAS-II and SiC/SiC, but intermediate for SiC/MAS–5. Typical monolithic silicon nitrides and silicon carbides at high temperatures $\geqslant$1200 $^{\circ}$C exhibit $n \geqslant 20$. Hence, compared with monolithic ceramics, the SiC/CAS-II and SiC/SiC composites exhibited a significantly higher susceptibility to damage evolution/accumulation.

The preload or accelerated test technique has been developed for monolithic ceramics in order to save test time in constant stress-rate testing [8, 9]. Based on *the power-law SCG* relation of equation (4.1 with some mathematical manipulation, strength of a test specimen under a preload (α) was derived as a function of preloading factor [2, 3, 8, 9]:

$$\sigma_{fp} = \sigma_f \left(1 + \alpha^{n+1}\right)^{\frac{1}{n+1}} \tag{4.4}$$

where σ_{fp} is strength with a preload and α is a preloading factor ($0 \leq \alpha \leq 1$ or $0 \leq \alpha \leq 100\%$ in percentage) in which a preload stress (applied to the test specimen) is normalized with respect to the strength with zero preload. Equation (4.4) indicates that strength with a preload is sensitive to the magnitude of preload particularly at lower n and higher α values. A theoretical prediction of ultimate strength as a function of preload, based on Eq. (4.4) with estimated values of n' from Figure 1, is shown in Figure 4. The prediction (solid lines) is in excellent agreement with the experimental data for all the three composite materials tested, as seen in the figure. This result obtained for the composite materials is also analogous to that observed in advanced monolithic ceramics and glass [8, 9]. Damage, mainly SCG, of monolithic ceramics occurs substantially close to 90 percent of total failure time because of their higher n ($\geqslant$20) value [8, 9]. The applicability of the preloading analysis for the composite materials strongly suggests that major damage evolution/accumulation process would be the one governed by the power-law relation (equation (4.1)) and that the damage would have occurred after a long incubation time, at least after 80 percent of total test time.

For the case that a single delayed failure mechanism (SCG) is predominant, a life prediction (for monolithic ceramics) from one loading configuration to another can be made analytically or numerically, depending on the complexity of loading configurations concerned. A life prediction under constant stress loading can be made based on equation (4.1) using constant stress-rate testing data as follows [11]:

$$t_f = \left[\frac{D^{n+1}}{n+1}\right] \sigma^{-n} \tag{4.5}$$

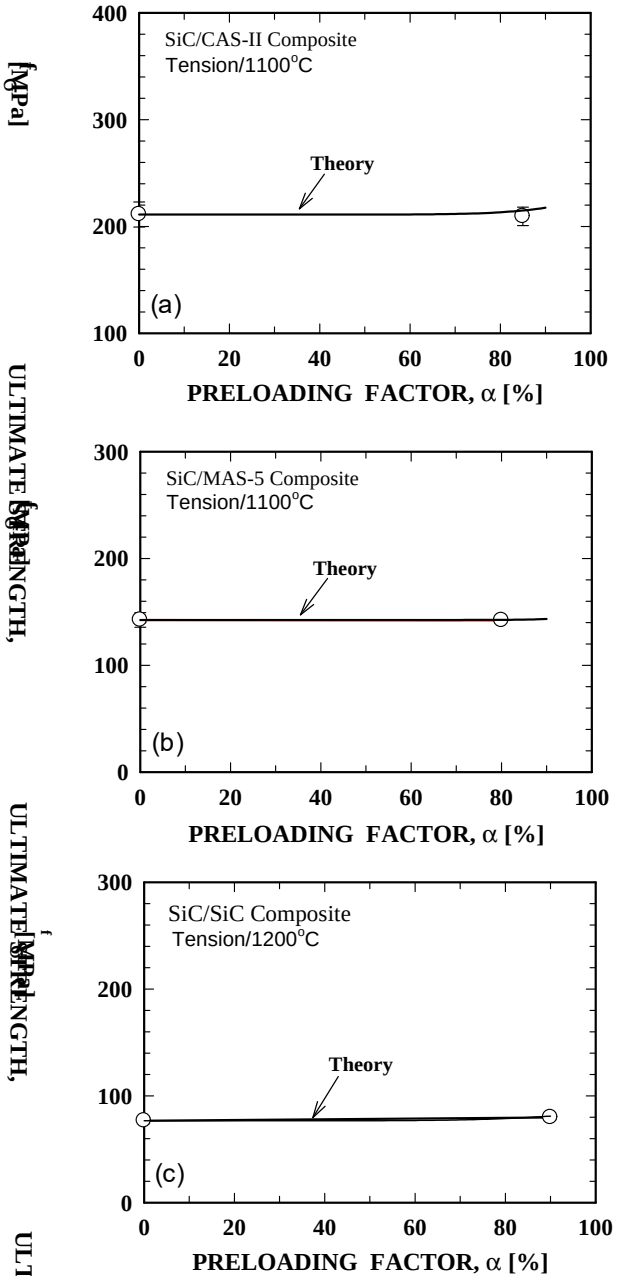

Figure 4. Result of preloading test (ultimate strength as a function of preloading) for (a) SiC/CAS II, (b) SiC/MAS 5, and (c) SiC/SiC composites at elevated temperatures in air. A theoretical line based on equation (4) [8, 9] is included for comparison for each composite material.

where t_f and σ are time to failure and applied stress, respectively. Use of equation (4.5) together with n' and D' determined in constant stress-rate testing allows one to predict life in constant stress loading. The results thus predicted are presented in Figure 3 as solid lines. Except for some discrepancy in the SiC/CAS-II composite, the overall prediction is in reasonable agreement with experimental data, at least for short periods of life. This indicates that the governing failure mechanism of SiC/MAS–5 and SiC/SiC was identical in both constant stress rate testing and constant stress testing. Since the prediction (equation (4.5)) was made based on the power-law relation, it is certain that the distinct failure mechanism of the two composite materials would be governed by the power-law type of damage evolution/accumulation (SCG or delayed failure).

The strength dependency on test rate, the applicability of preloading technique and the reasonable life prediction from one loading configuration (constant stress-rate testing) to another (constant stress or stress rupture testing) all support that the damage evolution/accumulation of the composite materials tested was controlled by a process very similar to the power-law type of SCG of monolithic ceramics, and that the failure mechanism was almost independent of loading configuration either in monotonically increased or in constant loading. This indicates that the constant stress-rate testing, commonly utilized in determining life prediction parameters of monolithic ceramics, could be applicable even to composite materials. The merit of constant stress rate testing is enormous in terms of simplicity and test economy (short test time) over other stress rupture or cyclic fatigue testing, especially for short lifetimes. A continuing effort to establish a database in constant stress rate testing at elevated temperatures is in progress using more ceramic matrix composites. A more detailed study regarding microscopic failure mechanisms [4, 12–15] associated with matrix/fiber interaction, matrix cracking and its effect on slow crack growth, and delayed failure of sustaining fibers near fracture, etc. is needed. Finally, the results of this work also suggest that care must be exercised when characterizing elevated-temperature strength of composite materials. This is due to the fact that elevated-temperature strength has a relative meaning if a material exhibits rate dependency: the strength simply depends on the selected test rate (Fig. 1). Therefore, at least two test rates (high and low) are recommended to better characterize the high-temperature strength behavior of a composite material.

5. **Conclusions**

Elevated-temperature strength of three continuous fiber-reinforced ceramic composites, including SiC/CAS-II, SiC/MAS–5, and SiC/SiC, exhibited a strong dependency on test rate, similar to the behavior observed in many advanced monolithic ceramics at elevated temperatures. The applicability of the preloading technique as well as the predictability of life from one loading configuration (constant stress-rate) to another (constant stress loading) suggested that the distinct, overall failure mechanism of the composite materials would be a process primarily governed by a power-law type of damage evolution/accumulation, analogous to the mechanism observed in

monolithic counterparts. It was further found that constant stress-rate testing could be utilized as a means of life prediction test methodology even for composites when short lifetimes are expected.

Acknowledgement. This work was supported in part by the UEET Program, NASA Glenn Research Center, Cleveland, Ohio. The authors are grateful to R. Pawlik for the experimental work during the course of this work.

References

1. Evans, A.G.: *Slow crack growth in brittle materials under dynamic loading condition*, Int. J. Fracture, **10**, (1974), 251–259.
2. ASTM C 1368, *Standard Test Method for Determination of Slow Crack Growth Parameters of Advanced Ceramics by Constant Stress-Rate Flexural Testing at Ambient Temperature*, Annual Book of ASTM Standards, Vol. 15.01, American Society for Testing and Materials, West Conshohocken, PA, 2001.
3. ASTM C 1465, *Standard Test Method for Determination of Slow Crack Growth Parameters of Advanced Ceramics by Constant Stress-Rate Flexural Testing at Elevated Temperatures*, Annual Book of ASTM Standards, Vol. 15.01, American Society for Testing and Materials, West Conshohocken, PA, 2001.
4. Sorenson, B.F. and Holmes, J.W.: *Effect of loading rate on the monotonic tensile behavior of a continuous-fiber-reinforced glass-ceramic matrix composite*, J. Am. Ceram. Soc., **79**(2), (1996), 313–320.
5. Worthem, D.W.: *Thermomechanical Fatigue Behavior of Three CFCC's*, NASA CR–195441, NASA Glenn Research Center, Cleveland, OH, 1995.
6. Choi, S.R. and Gyekenyesi, J.P.: *Effect of loading rate on strength of Nicalon^{TM}/CAS CFCC at elevated temperature*, in Proc. of the 7th Annual International Conference on Composite Materials, Edited D. Hui, Denver, CO, July 2–9, (2000), 299–300.
7. Worthem, D.W.: *Flat Tensile Specimen Design for Advanced Composites*, NASA CR–185261, NASA Glenn Research Center, Cleveland, OH, 1990.
8. Choi, S.R. and Gyekenyesi, J.P.: *Fatigue strength as a function of preloading in dynamic fatigue testing of glass and ceramics*, ASME Trans., J. Eng. Gas Turbines and Power, **119**(3), (1977), 493–499.
9. Choi, S.R. and Salem, J.A.: *Effect of preloading on fatigue strength in dynamic fatigue testing of ceramic materials at elevated temperatures*, Ceram. Eng. Sci. Proc., **16**(4), (1995), 87–94.
10. ASTM C 1359, *Standard Test Method for Monotonic Tensile Strength Testing of Continuous Fiber-Reinforced Advanced Ceramics with Solid Rectangular Cross-Section Specimens at Elevated Temperatures*, Annual Book of ASTM Standards, Vol. 15.01, American Society for Testing and Materials, West Conshohocken, PA, 2001.
11. Ritter, J.E.: *Engineering Design and Fatigue Failure of Brittle Materials*, pp. 667–686 in Fracture Mechanics of Ceramics, Vol. 4, Edited by R.C. Bradt, D.P.H. Hasselmann, and F.F. Lange, Plenum, NY (1978).
12. Curtin, W.C. and Halverson, H.G.: *High temperature deformation and failure in oxide/oxide composites*, HITEMP Review: Advanced High Temperature Engine Materials Technology Project, NASA/CP—1999-208915/VOL2, Paper 48, NASA Glenn Research Center, Cleveland, OH, 1999.

13. Lewinsohn, C.A., Henager, C.H. and Johns, R.H.: *Environmentally induced time-dependent failure mechanism in CFCCS at elevated temperatures*, Ceram. Eng. Sic. Proc., **19**(4), (1998), 11–18.

14. Henager, C.H. and Jones, R.H.: *Subcritical crack growth in CVI silicon carbide reinforced with Nicalon fibers: experiment and model*, J. Am. Ceram. Soc., **77**(9), (1994), 2381–94.

15. Spearing, S.M., Zok, F.W. and Evans, A.G.: *Stress corrosion cracking in a unidirectional ceramic-matrix composite*, J. Am. Ceram. Soc., **77**(2), (1994), 562–70.

Journal of Computational and Applied Mechanics, Vol. 3., No. 1., (2002), pp. 27–35

INVESTIGATION OF THE EQUATIONS OF MOTION IN TERMS OF DISPLACEMENTS, CONSTRUCTED ON THE BASIS OF THE LENNARD-JOHNS LAW, UNDER THE ACTION OF HARMONIC LOADING

Yura Kabish, Vasil Lavrenyuk
Faculty of Mechanics and Mathematics, Kyiv Taras Shevchenko University
01033 Kyiv, Ukraine
vlavrenyuk@mechmat.univ.kiev.ua

[Received: December 17, 2001]

Abstract. The paper presents the fundamental solutions established for the equations of motion written in terms of displacements in the theory of elasticity of crystalline systems and the hydromechanics of ideal liquids provided that the loading is harmonic and considering 2D and 3D problems as well. On the basis of the results obtained we have found the displacement field in an infinite elastic medium for the corresponding problems. Then the propagation of plane harmonic waves in the three-dimensional infinite elastic medium is investigated in the absence of mass forces.

Mathematical Subject Classification: 74S15, 74H05
Keywords: Lennard-Johns law, fundamental solutions

1. Introduction

The equations of motion in terms of displacements are established in paper [1] within the framework of the theory of elasticity of crystalline systems and the hydromechanics of ideal liquids. These equations are obtained on the basis of the principle of "smoothing" the equations of motion for a single particle interacting with the nearby particles according to the Lennard-Johns law. These equations have the form

$$\mu u_{i,jj} + (\lambda + \mu) u_{j,ij} - \gamma u_{i,jjpp} - k u_{j,ijpp} - q_{,i} + F_i = \rho \ddot{u}_i \tag{1.1}$$

and describe a process of deformation of amorphous bodies and non-viscous liquids which are isotropic media. These equations differ from the classical ones by the presence of fourth-order derivatives affecting the short-wave processes. The Lame constants λ, μ and the additional coefficients γ, k are all determined by the Lennard-Johns potential and by the distances of the particles. Note that $\gamma > 0,\ k > 0$. The term $q_{,i}$ in equation (1.1) specifies the temperature fluctuation. In the paper the fundamental solutions of the equations of motion (1.1) are constructed on the basis of the theory of generalized functions provided that the load is harmonic and the problems considered are 2D and 3D ones. The propagation of plane harmonic waves in the three-dimensional infinite elastic medium is investigated in the absence of mass

forces. Henceforth we assume that all processes except for mechanical displacements are neglected. The coefficients in equation (1.1) are all constants.

2. Fundamental solutions. Displacement fields

2.1. Taking into account the aforementioned assumptions, the equations of motion (1.1) can be written as follows:

$$\mu u_{i,jj} + (\lambda+\mu)u_{j,ij} - \gamma u_{i,jjpp} - k u_{j,ijpp} + F_i = \rho \ddot{u}_i \,. \tag{2.1}$$

Note that $F_i = F_i(\vec{x},t),\ u_i = u_i(\vec{x},t);\ \vec{x} \in R^n\ (n=2,3), i = \overline{1,n};\ \ t>0$. For many practical problems it is important to know the dynamical behavior of the solid body subjected to harmonic loading. Assuming that the transient process is finished and the system is in a steady-state mode, the initial conditions can be neglected. If this is the case the reaction depends on the frequency of the applied loading. Let us consider an infinite elastic medium. Suppose that the mass forces $F_i(\vec{x},t) = \overline{F}_i(\vec{x})e^{-i\omega t}$ are harmonic in time. Then the displacements are also harmonic in time, i.e., can be written as $u_i(\vec{x},t) = \overline{u}_i(\vec{x})e^{-i\omega t}$. Consequently, equation (2.1) assumes the form

$$(\mu\overline{u}_{i,jj} + (\lambda+\mu)\overline{u}_{j,ij} - \gamma\overline{u}_{i,jjpp} - k\overline{u}_{j,ijpp} + \overline{F}_i)e^{-i\omega t} = -\rho\omega^2\overline{u}_i e^{-i\omega t}\,.$$

Since $e^{-i\omega t} \neq 0\ \forall\, t>0$, we obtain from the last equation that

$$\mu\overline{u}_{i,jj} + (\lambda+\mu)\overline{u}_{j,ij} - \gamma\overline{u}_{i,jjpp} - k\overline{u}_{j,ijpp} + \rho\omega^2\overline{u}_i + \overline{F}_i = 0\,. \tag{2.2}$$

In order to find solutions to equations (2.2), one has to construct the fundamental solutions of these equations. Note that the differential operator that determines equation (2.2) is self-adjoint. The tensor with components $U_i^k = U_i^k(\vec{x}),\ i,k = \overline{1,n}$ is called the tensor of fundamental solutions of equations (2.2) if its components satisfy the equations

$$\mu U^k_{i,jj} + (\lambda+\mu)U^k_{j,ij} - \gamma U^k_{i,jjpp} - kU^k_{j,ijpp} + \rho\omega^2 U^k_i + \delta_{ik}\delta(\vec{x}) = 0 \tag{2.3}$$

where $\delta(\vec{x})$ is the generalized Dirac function, $\delta_{ik}\delta(\vec{x})$ is a unit force exerted at the origin and acting in the direction of the axis x_k. To solve equations (2.3) we shall apply the n-dimensional $(n=2,3)$ exponential Fourier transformation [2]

$$\tilde{f}(\vec{x}) = F[f(\vec{x})] = \int\limits_{R^n} f(\vec{x})e^{i(\vec{\alpha},\vec{x})}d\vec{x}, \quad \vec{x}\in R^n \tag{2.4}$$

to these equations. Here $\vec{\alpha}$ is a complex number and $(\vec{\alpha},\vec{x}) = \alpha_1 x_1 + \cdots + \alpha_n x_n$ is the scalar product in the corresponding n-dimensional space. Then we have

$$\mu\alpha_j\alpha_j F[U_i^k] + (\lambda+\mu)\alpha_i\alpha_j F[U_j^k] + \gamma\alpha_j\alpha_j\alpha_p\alpha_p F[U_i^k] + \\ + k\alpha_i\alpha_j\alpha_p\alpha_p F[U_j^k] - \rho\omega^2 F[U_i^k] - \delta_{ik} = 0 \tag{2.5}$$

Let $s = \alpha_p\alpha_p$. Multiply equation (2.5) by α_i and perform a summation with respect to the index i. After some simple manipulations we have

$$\alpha_j F[U_j^k] = \frac{\alpha_k}{(k+\gamma)s^2 + (\lambda+2\mu)s - \rho\omega^2}\,. \tag{2.6}$$

Upon substitution of equation (2.6) into (2.5) we obtain

$$F[U_i^k] = \frac{\delta_{ik}}{\gamma s^2 + \mu s - \rho\omega^2} - \frac{\alpha_i \alpha_k (\lambda + \mu + ks)}{[(k+\gamma)s^2 + (\lambda + 2\mu)s - \rho\omega^2]\,[\gamma s^2 + \mu s - \rho\omega^2]}. \quad (2.7)$$

Resolve the right-hand side of equation (2.7) into simple fractions

$$F[U_i^k] = A\delta_{ik}\left[\frac{1}{s+s_2^2} - \frac{1}{s+s_1^2}\right] - \\ - \alpha_i\alpha_k\left[\frac{A}{s_1^2}\frac{1}{s+s_1^2} - \frac{A}{s_2^2}\frac{1}{s+s_2^2} - \frac{B}{s_3^2}\frac{1}{s+s_3^2} + \frac{B}{s_4^2}\frac{1}{s+s_4^2}\right] \quad (2.8)$$

where

$$s_1 = \left[\frac{\sqrt{\mu^2 + 4\gamma\rho\omega^2} + \mu}{2\gamma}\right]^{\frac{1}{2}}; \quad s_2 = i\left[\frac{\sqrt{\mu^2 + 4\gamma\rho\omega^2} - \mu}{2\gamma}\right]^{\frac{1}{2}};$$

$$A = \frac{1}{\gamma(s_1^2 - s_2^2)}; \qquad s_3 = \left[\frac{\sqrt{(\lambda+2\mu)^2 + 4(k+\gamma)\rho\omega^2} + \lambda + 2\mu}{2(k+\gamma)}\right]^{\frac{1}{2}}; \quad (2.9)$$

$$B = \frac{1}{(k+\gamma)(s_3^2 - s_4^2)}; \qquad s_4 = i\left[\frac{\sqrt{(\lambda+2\mu)^2 + 4(k+\gamma)\rho\omega^2} - (\lambda+2\mu)}{2(k+\gamma)}\right]^{\frac{1}{2}}.$$

Useful inverse Fourier transforms are given below

– both in two-dimensional space:

$$F^{-1}\left[\frac{1}{s+a^2}\right] = \frac{K_0(ar)}{2\pi}, \quad r = \sqrt{x_i x_i}, \quad i = 1,2 \quad (2.10)$$

– and in three-dimensional space:

$$F^{-1}\left[\frac{1}{s+a^2}\right] = \frac{e^{-aR}}{4\pi R}, \quad R = \sqrt{x_i x_i}, \quad i = \overline{1,3} \quad (2.11)$$

where $K_0(z)$ is the modified Bessel function of second kind and zero order. Accordingly, the fundamental solutions of equations (2.2) have the forms

$$U_i^k(\vec{x}) = \frac{A\delta_{ik}}{2\pi}[K_0(s_2 r) - K_0(s_1 r)] - \\ - \frac{1}{2\pi}\frac{\partial^2}{\partial x_i \partial x_k}\left[\frac{AK_0(s_1 r)}{s_1^2} - \frac{AK_0(s_2 r)}{s_2^2} - \frac{BK_0(s_3 r)}{s_3^2} + \frac{BK_0(s_4 r)}{s_4^2}\right] \quad (2.12)$$

and

$$U_i^k(\vec{x}) = \frac{A\delta_{ik}}{4\pi R}\left[e^{-s_2 R} - e^{-s_1 R}\right] - \\ - \frac{1}{4\pi}\frac{\partial^2}{\partial x_i \partial x_k}\left[\frac{1}{R}\left(\frac{Ae^{-s_1 R}}{s_1^2} - \frac{Ae^{-s_2 R}}{s_2^2} - \frac{Be^{-s_3 R}}{s_3^2} + \frac{Be^{-s_4 R}}{s_4^2}\right)\right], \quad (2.13)$$

respectively. If the unit force is applied at point $\vec{\xi}$, then the fundamental solution is denoted by $U_i^k(\vec{x},\vec{\xi})$, and the radii r and R in expressions (2.12) and (2.13) are determined by the formulas

$$r=\sqrt{(x_i-\xi_i)(x_i-\xi_i)}\quad i=1,2;\qquad R=\sqrt{(x_i-\xi_i)(x_i-\xi_i)}\quad i=\overline{1,3}\,.$$

It is well known [2] that the derivative in terms of generalized functions contains functions which do not belong to the class $C^{(m)},\ m=1,2,3\ldots$, therefore it differs from the derivative taken in the ordinary sense. Let us investigate the derivative in equation (2.12). Since [3] $K_0(r)\sim\ln\frac{1}{r}$ as $r\to 0$, the function $K_0(ar)$ is discontinuous at $r=0$. We find [2]

$$\frac{\partial^2}{\partial x_i\partial x_k}\left(\ln\frac{1}{r}\right)=\frac{\widetilde{\partial}^2}{\partial x_i\partial x_k}\left(\ln\frac{1}{r}\right)-\pi\delta_{ik}\delta(\vec{x})\qquad i,k=1,2 \tag{2.14}$$

The tilde over the derivative sign on the right-hand side of equation (2.14) stands for a derivative taken in ordinary sense. The term $\pi\delta_{ik}\delta(\vec{x})$ is called singularity function. It follows from the aforementioned considerations that the singularity functions in

$$\frac{\partial^2}{\partial x_i\partial x_k}\left(\ln\frac{1}{r}\right)\qquad\text{and}\qquad\frac{\partial^2}{\partial x_i\partial x_k}\left(K_0(ar)\right)$$

coincide. Let us find the singular part $U_i^{k(\mathrm{sing})}$ $(i,k=1,2)$ of expression (2.12) :

$$U_i^{k(\mathrm{sing})}=\frac{1}{2\pi}\left(-\pi\delta_{ik}\delta(\vec{x})\right)\left[\frac{A}{s_1^2}-\frac{A}{s_2^2}-\frac{B}{s_3^2}+\frac{B}{s_4^2}\right]=0\,. \tag{2.15}$$

Consequently, the singular part $U_i^{k(\mathrm{sing})}$ of expression (2.12) is equal to zero. This means that derivatives in the fundamental solution for plane problems are derivatives taken in ordinary sense. Analogously we can investigate the singular part of expression (2.13). Since $\frac{e^{-aR}}{R}\sim\frac{1}{R}$ as $R\to 0$, the singular parts of $\frac{\partial^2}{\partial x_i\partial x_k}\left(\frac{e^{-aR}}{R}\right)$ and $\frac{\partial^2}{\partial x_i\partial x_k}\left(\frac{1}{R}\right)$ coincide. We find [2]

$$\frac{\partial^2}{\partial x_i\partial x_k}\left(\frac{1}{R}\right)=\frac{\widetilde{\partial}^2}{\partial x_i\partial x_k}\left(\frac{1}{R}\right)-\frac{4\pi}{3}\delta_{ik}\delta(\vec{x})\,. \tag{2.16}$$

Therefore the singular part of expression (2.13) is also equal to zero:

$$U_i^{k(sing)}=\frac{1}{4\pi}\left(-\frac{4\pi}{3}\delta_{ik}\delta(\overrightarrow{x})\right)\left[\frac{A}{s_1^2}-\frac{A}{s_2^2}-\frac{B}{s_3^2}+\frac{B}{s_4^2}\right]=0\,. \tag{2.17}$$

This means that the derivatives in the fundamental solution for 3D problems are derivatives taken in ordinary sense. The absence of functions of singularities in expressions (2.12) and (2.13) indicates the correctness of the results obtained. Note that analogous results are correct for fundamental solutions, obtained in the case when unit force is applied at a point $\vec{\xi}$.

2.2. Now we can find displacement fields for 2D and 3D problems. As it was mentioned above, $u_i(\vec{x},t)=\overline{u}_i(\vec{x})e^{-i\omega t}$, where $\overline{u}_i(\vec{x})$ is calculated as a convolution:

$$\overline{u}_i(\vec{x})=U_i^k(\vec{x})*\overline{F_k}(\vec{x})=\int\limits_{R^n}U_i^k(\vec{y})\overline{F_k}(\vec{x}-\vec{y})d\vec{y}\,. \tag{2.18}$$

Therefore the displacement field is $u_i(\vec{x},t)=(U_i^k(\vec{x})e^{-i\omega t})*\overline{F_k}(\vec{x})$. Taking formulas (2.9) into account, we have the displacements in two-dimensional space:

$$\begin{aligned}u_i(\vec{x},t)=\Bigg\{&\frac{A\delta_{ik}e^{-i\omega t}}{2\pi}\left[K_0\left(i\left[\frac{\sqrt{\mu^2+4\gamma\rho\omega^2}-\mu}{2\gamma}\right]^{\frac12}r\right)-K_0\left(\left[\frac{\sqrt{\mu^2+4\gamma\rho\omega^2}+\mu}{2\gamma}\right]^{\frac12}r\right)\right]\\
-\frac{e^{-i\omega t}}{2\pi}\frac{\partial^2}{\partial x_i\partial x_k}&\left[\frac{A}{s_1^2}K_0\left(\left[\frac{\sqrt{\mu^2+4\gamma\rho\omega^2}+\mu}{2\gamma}\right]^{\frac12}r\right)-\frac{A}{s_2^2}K_0\left(i\left[\frac{\sqrt{\mu^2+4\gamma\rho\omega^2}-\mu}{2\gamma}\right]^{\frac12}r\right)-\right.\\
&-\frac{B}{s_3^2}K_0\left(\left[\frac{\sqrt{(\lambda+2\mu)^2+4(k+\gamma)\rho\omega^2}+\lambda+2\mu}{2(k+\gamma)}\right]^{\frac12}r\right)+\\
&\left.+\frac{B}{s_4^2}K_0\left(i\left[\frac{\sqrt{(\lambda+2\mu)^2+4(k+\gamma)\rho\omega^2}-(\lambda+2\mu)}{2(k+\gamma)}\right]^{\frac12}r\right)\right]\Bigg\}*\overline{F_k}(\vec{x})\,.\end{aligned} \tag{2.19}$$

The displacement field in three-dimensional space can be written as follows

$$\begin{aligned}u_i(\vec{x},t)=\Bigg\{&\frac{A\delta_{ik}}{4\pi R}\left[e^{-i\left(\left[\frac{\sqrt{\mu^2+4\gamma\rho\omega^2}-\mu}{2\gamma}\right]^{\frac12}R+\omega t\right)}-e^{-\left[\frac{\sqrt{\mu^2+4\gamma\rho\omega^2}+\mu}{2\gamma}\right]^{\frac12}R-i\omega t}\right]-\\
-\frac{1}{4\pi}\frac{\partial^2}{\partial x_i\partial x_k}&\left[\frac{1}{R}\left(\frac{A}{s_1^2}e^{-\left[\frac{\sqrt{\mu^2+4\gamma\rho\omega^2}+\mu}{2\gamma}\right]^{\frac12}R-i\omega t}-\frac{A}{s_2^2}e^{-i\left(\left[\frac{\sqrt{\mu^2+4\gamma\rho\omega^2}-\mu}{2\gamma}\right]^{\frac12}R+\omega t\right)}-\right.\right.\\
&-\frac{B}{s_3^2}e^{-\left[\frac{\sqrt{(\lambda+2\mu)^2+4(k+\gamma)\rho\omega^2}+\lambda+2\mu}{2(k+\gamma)}\right]^{\frac12}R-i\omega t}+\\
&\left.\left.+\frac{B}{s_4^2}e^{-i\left(\left[\frac{\sqrt{(\lambda+2\mu)^2+4(k+\gamma)\rho\omega^2}-(\lambda+2\mu)}{2(k+\gamma)}\right]^{\frac12}R+\omega t\right)}\right)\right]\Bigg\}*\overline{F_k}(\vec{x})\,.\end{aligned} \tag{2.20}$$

Note that genuine displacements for 2D and 3D problems are given by real or imaginary components of expressions (2.19) and (2.20), respectively. Let us consider the solutions obtained for two-dimensional space. They differ from the classical ones by the presence of additional terms. These are modified Bessel functions of second kind and zero order with real arguments. It is known [3] that if the argument of function $K_0(z)$ is a real value and it increases, then the function is damped exponentially. On the other hand, $K_0(r)\sim\ln\frac{1}{r}$ as $r\to 0$. It follows from the previous considerations that the additional terms have a great influence on the behavior of the displacement field near the perturbation source and it gradually vanishes as r increases. Let us consider solutions (2.20). The presence of additional terms influences the behavior

of the displacement field near the perturbation source (i. e., as $R \to 0$). In contrast to the classical case, the solutions obtained do not tend to infinity as $R \to 0$. In other words, the influence of these terms on the displacement field as R increases is insignificant. Note that solutions, obtained for 3D problems, tend to zero as $R \to \infty$. This behaviour confirms again the correctness of the results. It is worthy of mention that we obtain the classical solutions for 2D and 3D problems if $k \to 0$, and $\gamma \to 0$.

3. **Propagation of plane harmonic waves**

3.1. Let us investigate the propagation of plane harmonic waves, described by (2.1), in an infinite elastic medium in the direction of axis x_1. This means that $u_j = u_j(x_1, t),\ j = \overline{1,3}$. Suppose that the mass forces are absent. Then equation (2.1) can be written as follows:

$$\begin{cases} (k+\gamma)\dfrac{\partial^4 u_1}{\partial x_1^4} - (\lambda+2\mu)\dfrac{\partial^2 u_1}{\partial x_1^2} + \rho\ddot{u}_1 = 0 \\ \gamma\dfrac{\partial^4 u_2}{\partial x_1^4} - \mu\dfrac{\partial^2 u_2}{\partial x_1^2} + \rho\ddot{u}_2 = 0 \\ \gamma\dfrac{\partial^4 u_3}{\partial x_1^4} - \mu\dfrac{\partial^2 u_3}{\partial x_1^2} + \rho\ddot{u}_3 = 0 \end{cases} \tag{3.1}$$

where the first equation describes propagation of longitudinal waves. The second and third equations describe the propagation of transverse waves. Taking into account that these three equations differ only in their coefficients we can write

$$\frac{\partial^4 u_j}{\partial x_1^4} - C_{(1)}\frac{\partial^2 u_j}{\partial x_1^2} + C_{(2)}\ddot{u_j} = 0, \quad j = \overline{1,3} \tag{3.2}$$

where

$$C_{(1)} = \begin{cases} \dfrac{\lambda+2\mu}{k+\gamma} & - \text{ for longitudinal waves} \\ \dfrac{\mu}{\gamma} & - \text{ for transverse waves} \end{cases} \tag{3.3}$$

$$C_{(2)} = \begin{cases} \dfrac{\rho}{k+\gamma} & - \text{ for longitudinal waves} \\ \dfrac{\rho}{\gamma} & - \text{ for transverse waves} \end{cases} \tag{3.4}$$

Solutions of equations (3.2) assume the form

$$u_j(\vec{x}_1, t) = e^{i(kx_1 - \omega t)}, \quad j = \overline{1,3} \tag{3.5}$$

where k is the wave number and ω is the frequency. Substituting expression (3.5) into equation (3.2) we obtain the characteristic equation

$$k^4 + C_{(1)}k^2 - C_{(2)}\omega^2 = 0 \tag{3.6}$$

from which

$$k^{(1)} = \left[\frac{\sqrt{C_{(1)}^2 + 4C_{(2)}\omega^2} - C_{(1)}}{2}\right]^{\frac{1}{2}} \qquad k^{(2)} = -\left[\frac{\sqrt{C_{(1)}^2 + 4C_{(2)}\omega^2} - C_{(1)}}{2}\right]^{\frac{1}{2}}$$
$$k^{(3)} = i\left[\frac{\sqrt{C_{(1)}^2 + 4C_{(2)}\omega^2} + C_{(1)}}{2}\right]^{\frac{1}{2}} \qquad k^{(4)} = -i\left[\frac{\sqrt{C_{(1)}^2 + 4C_{(2)}\omega^2} + C_{(1)}}{2}\right]^{\frac{1}{2}}. \tag{3.7}$$

Two of the roots obtained are complex values. However, they are not wave numbers although they both occur in the general solution of equation (3.2). Besides, $|k^{(1)}| = |k^{(2)}|$. This means that one velocity is the velocity of propagation for longitudinal waves and the other is the velocity of propagation for transverse waves. The general solution of equation (3.2) is of the form

$$u_j(x_1 t) = D_1 e^{i\left[\left[\frac{\sqrt{C_{(1)}^2+4C_{(2)}\omega^2}-C_{(1)}}{2}\right]^{\frac{1}{2}} x_1 - \omega t\right]} + D_2 e^{-i\left[\left[\frac{\sqrt{C_{(1)}^2+4C_{(2)}\omega^2}-C_{(1)}}{2}\right]^{\frac{1}{2}} x_1 + \omega t\right]} +$$
$$+ D_3 e^{-i\omega t} e^{-\left[\frac{\sqrt{C_{(1)}^2+4C_{(2)}\omega^2}+C_{(1)}}{2}\right]^{\frac{1}{2}} x_1} + D_4 e^{-i\omega t} e^{\left[\frac{\sqrt{C_{(1)}^2+4C_{(2)}\omega^2}+C_{(1)}}{2}\right]^{\frac{1}{2}} x_1} \tag{3.8}$$

where D_j are constants, $j = \overline{1,4}$. Let us analyze the solutions we have obtained. The first and third terms in (3.8) represent a wave moving to the right (in the positive direction of axis x_1). The second and fourth terms in (3.8) represent a wave moving to the left (in negative direction of x_1). Note that the vibrations determined by the third and fourth terms damp quickly while the first and second terms characterize harmonic vibrations. Solutions (3.8) clearly show that in a negligible neighborhood of the perturbation source the vibrations are non-stationary, and they gradually become harmonic waves. Let us investigate the dependence between wave number k and frequency ω. From equation (3.7) we have

$$k = \sqrt{\frac{\sqrt{C_{(1)}^2 + 4C_{(2)}\omega^2} - C_{(1)}}{2}}. \tag{3.9}$$

From the last equality we obtain

$$\omega = k\sqrt{\frac{C_{(1)}}{C_{(2)}}}\sqrt{1 + \frac{k^2}{C_{(1)}}}. \tag{3.10}$$

Note that

$$\sqrt{\frac{C_{(1)}}{C_{(2)}}} = \begin{cases} c_1 = \sqrt{\dfrac{\lambda + 2\mu}{\rho}} & - \text{ for longitudinal waves} \\ c_2 = \sqrt{\dfrac{\mu}{\rho}} & - \text{ for transverse waves} \end{cases} \tag{3.11}$$

It is known that c_1 and c_2 are the classical velocities of propagation for the longitudinal and transverse waves, respectively. Equality (3.10) determines a quadratic dependence between the wave number and the frequency. Note that as $n \to 0$ we obtain a linear dependence between these values. Indeed, if we expand the right-hand side of equation (3.10) we have

$$\omega = k\sqrt{\frac{C_{(1)}}{C_{(2)}}}\left(1 + \frac{k^2}{2C_{(1)}} - \frac{k^4}{8C_{(1)}^2} + \cdots\right). \tag{3.12}$$

Neglecting the terms of third and higher degrees we obtain the classical dependence between the wave number and the frequency. We deduce from the last equality that the longer the wave the less the difference between the results obtained from the classical and specified equations. This fact lets us conclude that the specified equations are more suitable to describe short-wave processes.

3.2 If the direction of propagation of a plane harmonic wave does not coincide with the axis x_1, the displacement field is described by more complicated formulas, although the physical picture remains the same. Let us consider a common case of propagation of plane harmonic waves in a three-dimensional infinite elastic medium in the direction of vector $\vec{n}$ with velocity c. Consequently, the components of the displacement vector are functions of one parameter, i.e., $u_i = u_i(Z)$, $Z = \vec{n}\,\vec{r} - ct$, where $\vec{n}$ is the normal to the plane $Z = const$. If we introduce a coordinate system $x'_1x'_2x'_3$, where x'_1 is perpendicular to the plane $Z = const$, and the positive direction of this axis coincides with the direction of vector $\vec{n}$, then in the new coordinate system all the results concerning the propagation of plane harmonic waves in the direction of axis x_1 are valid.

4. Conclusions

In the paper the fundamental solutions of the specified equations of motion are constructed assuming 2D and 3D problems and harmonic loading. On the basis of the results obtained we have found the displacement fields in an infinite elastic medium for the corresponding problems. An analysis of the results shows that the solutions of 2D and 3D problems include additional terms, influencing the behavior of the displacement field near the perturbation source. The propagation of plane harmonic waves in the three-dimensional infinite elastic medium in absence of mass forces has also been investigated. The presence of fourth-order derivatives in the equations of motion makes it possible to investigate short-wave processes more accurately. When the wave-length is large, the classical equations and the specified equations lead to the same results.

References

1. Khoroshun, L. P.: *Construction of the governing equations of mechanics for a continuous medium on the base of the Lennard-Johns potential*, Applied Mechanics, **31**(7), (1995), 25–37. (in Russian).

2. Kech, V. and Teodorescu, P.: *Introduction to the Theory of Generalized Functions with Applications in Engineering*, Mir, Moscow, 1978. (in Russian).

3. Janke, E., Emde, F., and Teodorescu, P.: *Special Functions*, Nauka, Moscow, 1977. (in Russian).

Journal of Computational and Applied Mechanics, Vol. 3., No. 1., (2002), pp. 37–49

CALCULATION OF THE WORK DONE BY DEFORMATION DEPENDENT TRACTIONS

Imre Kozák
Department of Mechanics, University of Miskolc
3515 Miskolc–Egyetemváros, Hungary
mechkoz@gold.uni-miskolc.hu

Tamás Szabó
Numerical Mechanics Research Group - Hungarian Academy of Sciences
3515 Miskolc–Egyetemváros, Hungary
mechsza@gold.uni-miskolc.hu

[Received: September 28, 2001]

Dedicated to Professor Gyula Béda on the occasion of his seventieth birthday

Abstract. A generalization of the well-known Nanson's formula for solids has been set up for shells. These formulae relate a surface element vector taken either on the base surface or on the side surface in the reference configuration to any surface element vector in the instantaneous configuration. The characteristic quantities can be given by their truncated Taylor expansions with respect to the control parameter. In this way, the work increment done by a deformation dependent traction can always be calculated through integrals taken in the reference configuration, i.e., for shells on the base surface or on the side surface.

Mathematical Subject Classification: 7499, 74A05
Keywords: deformation dependent tractions, surface element vectors, shells, control parameters, truncated Taylor expansions, displacement increment, work increment

1. Introduction

In order to solve a statical problem, calculation of the work increment done by the loads either during an increment in the kinematically admissible displacement or during an increment in the effective displacement is frequently required. This situation arises, for example, in the application of the incremental form of the principle of virtual work (see, e.g., Molk et al [1], Kozák and Szabó [2]). This is also the case in the course of the solution of stability problems when the work increment done by the loads of an equilibrium configuration during a small perturbation in displacements is calculated.

In this paper the applied normal tractions are deformation dependent and are always perpendicular to the instantaneous surface of the body. The aim of this paper is to calculate the work increment done by the loads of any equilibrium configuration

through an arbitrary displacement increment, both for an arbitrary body and for shells. Large strains are assumed.

In Section 2 three coordinate systems are introduced: namely, the first is defined in the instantaneous configuration, the second is given in the reference configuration of an arbitrary body and the third is associated with the base surface of the shell also in the reference configuration. The geometrical characteristics of the coordinate systems are also presented together with the applied notations.

In Section 3 relationships are established for the surface element vectors concerning both arbitrary solids and shells in an instantaneous configuration and in a reference one. For shells we distinguish a surface element on the base surface from a surface element on the side surface.

Section 4 gives the forces exerted on surface elements at the points of an instantaneous configuration by means of surface elements at the points of the base surface of a shell.

Section 5 details the formulation of the work increment done by the deformation dependent tractions during an arbitrary increment in the displacements. The characteristic quantities are expanded in truncated Taylor series written in an equilibrium configuration with respect to a control parameter. Then the power of the loads is calculated for each intermediate state of a displacement increment, and finally the work increment is given by integrating the power with respect to the control parameter. As a matter of fact the work increment is given by surface integrals, which are calculated by making use of those quantities defined in the reference configuration. In case of shells the integrals are taken on the base surface or on the side surface.

Invariant and indicial notations are used throughout this paper.

In invariant notation vectors and tensors are denoted by bold lower case letters and upper case letters, respectively. A dot denotes the scalar product, e.g. $\boldsymbol{Q}\cdot\mathrm{d}\mathbf{A}$.

In case of indicial notations the coordinate systems we use are assumed to be curvilinear ones. Latin and Greek indices range over the integers 1,2,3 and 1,2. A subscript preceded by a (comma)[semicolon] denotes (partial)[covariant] differentiation with respect to the corresponding coordinate. δ_k^l is the Kronecker delta while e_{klm} and e^{pqr} stand for the permutation symbols.

2. Configurations

2.1. Let us denote the stress and deformation-free reference configuration and the present or instantaneous configuration by (B) and $(\overline{B})$, respectively. Configuration $(\overline{B})$ is an equilibrium one for the actual load level.

In order to extend our investigations for shells, we introduce a base surface (A°) bounded by a closed curve (g°) in the reference configuration (B).

Body forces are neglected, only distributed normal tractions exerted on instantaneous outer surfaces are considered (deformation dependent loads or follower loads).

It is assumed that the kinematical boundary conditions are independent of deformations.

Let us denote the various coordinate systems, a point, the position vector, the local base vectors and the metric tensors in the three different configurations as follows:

– in the current configuration $(\overline{B})$:

$$\{\overline{x}^p\},\ \overline{P},\ \overline{\mathbf{r}},\ \overline{\mathbf{g}}_p,\ \overline{\mathbf{g}}^q,\ \overline{g}_{pq},\ \overline{g}^{rs},$$

– at the arbitrary point P of the reference configuration (B):

$$\{x^k\},\ P,\ \mathbf{r},\ \mathbf{g}_k,\ \mathbf{g}^l,\ g_{kl},\ g^{mn},$$

– on the base surface (A°) of the shell in the reference configuration (B):

$$\{x^{\circ a}\},\ P^\circ,\ \mathbf{r}^\circ,\ \mathbf{g}^\circ_a,\ \mathbf{g}^{\circ b},\ g^\circ_{ab},\ g^{\circ cd}.$$

REMARK 2.1. The curvilinear coordinate systems introduced are arbitrary except the one defined for shells in the reference configuration (B).

2.2. For shells in the reference configuration (B) (see Figure 1) we have at the point P° of the base surface (A°) for which $x^3 = 0$ that:

$$\mathbf{g}^\circ_\alpha = \frac{\partial \mathbf{r}^\circ}{\partial x^{\circ\alpha}}, \quad \mathbf{g}^\circ_3 = \mathbf{g}^{\circ 3} = \frac{\mathbf{g}^\circ_1 \times \mathbf{g}^\circ_2}{|\mathbf{g}^\circ_1 \times \mathbf{g}^\circ_2|}\,. \tag{2.1}$$

If we regard an arbitrary point P $\left(x^3 \neq 0\right)$ then

$$\mathbf{r} = \mathbf{r}^\circ + \mathbf{g}^\circ_3 x^3, \tag{2.2}$$

$$\mathbf{g}_\alpha = \mathbf{g}^\circ_\alpha - b^{\circ\beta}_\alpha \mathbf{g}^\circ_\beta x^3 = \left(\delta^\beta_\alpha - b^{\circ\beta}_\alpha x^3\right)\mathbf{g}^\circ_\beta = \mu^{\beta^\circ}_\alpha\, \mathbf{g}^\circ_\beta, \quad \mathbf{g}_3 = \mathbf{g}^\circ_3 \tag{2.3}$$

where $b^{\circ\beta}_\alpha = -\,\mathbf{g}^\circ_{3,\alpha} \cdot \mathbf{g}^{\circ\beta}$ is the tensor of curvature on the surface (A°) and

$$\mu^{\beta^\circ}_\alpha = \delta^\beta_\alpha - b^{\circ\beta}_\alpha x^3, \quad \mu^{\beta^\circ}_3 = 0, \quad \mu^{3^\circ}_3 = 1 \tag{2.4}$$

where $\mu^{b^\circ}_a$ are the coordinates of a shifter. The inverse shifter is denoted by $\mu^d_{c^\circ}$.

REMARK 2.2. The coordinates x^α and $x^{\circ\alpha}$ of the points P and P° are identical for shells $x^\alpha = x^{\circ\alpha}$, however the corresponding coordinates x^3 are different.

2.3. The permutation tensors taken at the point

$\bar{P}$ are denoted by $\quad \overline{\varepsilon}_{pqr} = \sqrt{\overline{g}}\, e_{pqr}, \quad \overline{\varepsilon}^{rst} = \dfrac{1}{\sqrt{\overline{g}}} e^{rst}, \qquad \left(\overline{g} = \det \overline{g}_{pq}\right), \tag{2.5}$

P are denoted by $\quad \varepsilon_{klm} = \sqrt{g}\, e_{klm}, \quad \varepsilon^{lmn} = \dfrac{1}{\sqrt{g}} e^{lmn}, \qquad \left(g = \det g_{kl}\right), \tag{2.6}$

P° are denoted by $\quad \varepsilon^\circ_{abc} = \sqrt{g^\circ}\, e_{abc}, \quad \varepsilon^{\circ bcd} = \dfrac{1}{\sqrt{g^\circ}} e^{bcd}. \quad \left(g^\circ = \det g^\circ_{ab}\right). \tag{2.7}$

2.4. In accordance with the notations introduced the following conventions are applied. In case of invariant notations a barred letter, a single letter, or a letter with a small circle as a superscript identifies the point from the triplet $\overline{P}$, P or P°, at which the quantity denoted by the letter is defined. In addition to this, when indicial notations are used the same tensor or vector can be written in the local coordinate

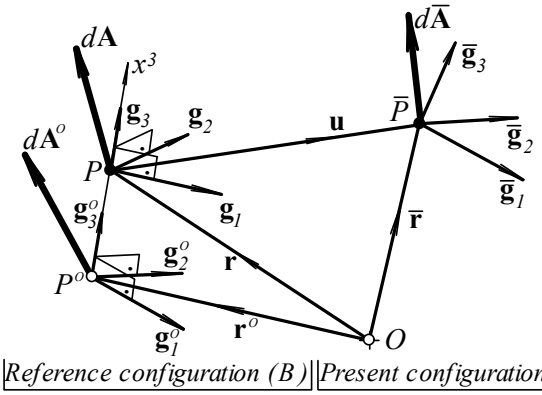

Figurre 1. Base vectors and urface element vectors of shells

system of different points, e.g., the surface element vector defined at point $\overline{P}$ can be written as:

$$\mathrm{d}\overline{\mathbf{A}} = \mathrm{d}\overline{A}_{\overline{p}}\overline{\mathbf{g}}^{p} = \mathrm{d}\overline{A}_{k}\mathbf{g}^{k} = \mathrm{d}\overline{A}_{a^{\circ}}\mathbf{g}^{\circ a}. \tag{2.8}$$

The displacement vector of an arbitrary point can be defined at point $\overline{P}$ and also at point P, and it can be given by the base vectors of point P° as well:

$$\overline{\mathbf{u}} = \overline{u}_{\overline{p}}\overline{\mathbf{g}}^{p} = u_{k}\mathbf{g}^{k} = \mathbf{u} = u_{a^{\circ}}\mathbf{g}^{\circ a}. \tag{2.9}$$

For our later considerations we shall distinguish the arbitrary coordinate system in the reference configuration (B) from the one defined for shells in the same configuration.

3. Surface element vectors

3.1. A geometrical representation. For shells Figure 1 shows the three surface element vectors defined at points $\overline{P}$, P and P°:

$$\overline{P} : \mathrm{d}\overline{\mathbf{A}} = \mathrm{d}\overline{A}_{\overline{p}}\overline{\mathbf{g}}^{p} = \mathrm{d}\overline{\mathbf{r}}_{\mathrm{I}} \times \mathrm{d}\overline{\mathbf{r}}_{\mathrm{II}}, \quad \mathrm{d}\overline{A}_{\overline{p}} = \overline{\varepsilon}_{pqr}\mathrm{d}\overline{x}^{q}_{\mathrm{I}}\mathrm{d}\overline{x}^{r}_{\mathrm{II}}, \tag{3.1}$$

$$P : \mathrm{d}\mathbf{A} = \mathrm{d}A_{k}\mathbf{g}^{k} = \mathrm{d}\mathbf{r}_{\mathrm{I}} \times \mathrm{d}\mathbf{r}_{\mathrm{II}}, \quad \mathrm{d}A_{k} = \varepsilon_{klm}\mathrm{d}x^{l}_{\mathrm{I}}\mathrm{d}x^{m}_{\mathrm{II}}, \tag{3.2}$$

$$P^{\circ} : \mathrm{d}\mathbf{A}^{\circ} = \mathrm{d}A^{\circ}_{a}\mathbf{g}^{\circ a} = \mathrm{d}\mathbf{r}^{\circ}_{\mathrm{I}} \times \mathrm{d}\mathbf{r}^{\circ}_{\mathrm{II}}, \quad \mathrm{d}A^{\circ}_{a^{\circ}} = \varepsilon^{\circ}_{abc}\mathrm{d}x^{\circ b}_{\mathrm{I}}\mathrm{d}x^{\circ c}_{\mathrm{II}} \tag{3.3}$$

where $\mathrm{d}\overline{\mathbf{r}}_{\mathrm{I}}$, $\mathrm{d}\mathbf{r}_{\mathrm{I}}$, $\mathrm{d}\mathbf{r}^{\circ}_{\mathrm{I}}, \ldots$ are line elements at points $\overline{P}$, P and P°, respectively.

REMARK 3.1. The surface element vector $\mathrm{d}\mathbf{A}^{\circ}$ can be oriented arbitrarily in comparison with the base surface (A°).

Let us set ourselves a task to derive three relationships for an arbitrary body and arbitrary shells between the following pairs of surface element vectors

$$\mathrm{d}\overline{\mathbf{A}} \text{ and } \mathrm{d}\mathbf{A}, \quad \mathrm{d}\mathbf{A} \text{ and } \mathrm{d}\mathbf{A}^{\circ}, \quad \mathrm{d}\overline{\mathbf{A}} \text{ and } \mathrm{d}\mathbf{A}^{\circ}.$$

3.2. An arbitrary coordinate system in configuration (B)**.** The mapping between the configurations $(\overline{B})$ and (B) is given either by the function of motion or

by the displacement field

$$\overline{x}^p = \overline{x}^p(x^1, x^2, x^3; t), \quad J = \det \frac{\partial \overline{x}^p}{\partial x^k} \neq 0, \tag{3.4}$$

$$\overline{\mathbf{r}} = \mathbf{r} + \mathbf{u}, \quad \mathbf{u} = \mathbf{u}(x^1, x^2, x^3; t). \tag{3.5}$$

For the line element $\mathrm{d}\overline{\mathbf{r}}$ we can write the following relationships:

$$\mathrm{d}\overline{\mathbf{r}} = \overline{\mathbf{g}}_q \mathrm{d}\overline{x}^q = \frac{\partial \overline{\mathbf{r}}}{\partial \overline{x}^q}\mathrm{d}\overline{x}^q = \frac{\partial(\mathbf{r}+\mathbf{u})}{\partial x^l}\frac{\partial x^l}{\partial \overline{x}^q}\mathrm{d}\overline{x}^q = (\delta^l_s + u^l{}_{;s})\mathrm{d}x^s \mathbf{g}_l, \tag{3.6}$$

where

$$\mathrm{d}x^s = \frac{\partial x^s}{\partial \overline{x}^q}\mathrm{d}\overline{x}^q$$

which follows from the inverse function of motion $x^s = x^s(\overline{x}^1, \overline{x}^2, \overline{x}^3; t)$.

Using equation (3.6) for the line elements $\mathrm{d}\mathbf{r}_{\mathrm{I}}$ and $\mathrm{d}\mathbf{r}_{\mathrm{II}}$, the surface element vector given by equation (3.1) can be written as:

$$\mathrm{d}\overline{\mathbf{A}} = \mathrm{d}\overline{\mathbf{r}}_{\mathrm{I}} \times \mathrm{d}\overline{\mathbf{r}}_{\mathrm{II}} = \mathbf{g}^k \varepsilon_{klm}(\delta^l_s + u^l{}_{;s})(\delta^m_t + u^m{}_{;t})\mathrm{d}x^s_{\mathrm{I}}\mathrm{d}x^t_{\mathrm{II}}. \tag{3.7}$$

Making use of the identity

$$\varepsilon_{klm}(\delta^l_s + u^l{}_{;s})(\delta^m_t + u^m{}_{;t}) = \frac{1}{2}e_{klm}e^{hij}(\delta^l_i + u^l{}_{;i})(\delta^m_j + u^m{}_{;j})\varepsilon_{hst} \tag{3.8}$$

the surface element vector can be expressed as

$$\mathrm{d}\overline{\mathbf{A}} = \mathbf{g}^k Q^h_k \mathrm{d}A_h, \quad Q^h_k = \frac{1}{2}e_{klm}e^{hij}(\delta^l_i + u^l{}_{;i})(\delta^m_j + u^m{}_{;j}) \tag{3.9}$$

where $\mathrm{d}A_h$ is the surface element at point P given by (3.2).

The surface element vector $\mathrm{d}\overline{\mathbf{A}}$ at the point $\overline{P}$ given by (3.9) can be related to the surface element vector $\mathrm{d}\mathbf{A}$:

$$\mathrm{d}\overline{\mathbf{A}} = \mathrm{d}\overline{A}_q \overline{\mathbf{g}}^q = \mathrm{d}\overline{A}_k \mathbf{g}^k = \boldsymbol{Q} \cdot \mathrm{d}\mathbf{A}, \quad \boldsymbol{Q} = Q^h_k \mathbf{g}^k \mathbf{g}_h, \tag{3.10}$$

$$\mathrm{d}\overline{A}_k = Q^h_k \mathrm{d}A_h. \tag{3.11}$$

REMARK 3.2. Relationships (3.9)-(3.11) are always satisfied.

REMARK 3.3. Relationships (3.9) and (3.10) can be manipulated into a different form by the use of the Nanson formula (see, e.g., Béda et al [3], Mason [4]):

$$\mathrm{d}\overline{\mathbf{A}} = J\sqrt{\frac{\overline{g}}{g}}\left(\boldsymbol{F}^{-1}\right)^{\mathrm{T}} \cdot \mathrm{d}\mathbf{A},$$

where $\boldsymbol{F}^{-1}$ is the inverse of the deformation gradient and T denotes the transpose.

3.3. A coordinate system for shells in configuration (B)**.** For shells one can shift the surface element vector $\mathrm{d}\mathbf{A}$ to point P° by the aid of an inverse shifter $\mu^k_{a^\circ}$

$$\mathrm{d}A_{a^\circ} = \mu^k_{a^\circ}\mathrm{d}A_k. \tag{3.12}$$

In accordance with Remark 2.2. we shall assume at points P° and P that

$$\mathrm{d}x^{\circ b} = \mathrm{d}x^b. \tag{3.13}$$

and using (3.12), (3.2), we have

$$\mathrm{d}A_{a^\circ} = \mu^k_{a^\circ}\varepsilon_{klm}\mathrm{d}x^l_{\mathrm{I}}\mathrm{d}x^m_{\mathrm{II}} = \varepsilon^\circ_{abc}\mu^{b^\circ}_l\mu^{c^\circ}_m\mathrm{d}x^l_{\mathrm{I}}\mathrm{d}x^m_{\mathrm{II}}. \tag{3.14}$$

Introducing the notations

$$e_{abc}\mu^{a^\circ}_k\mu^{b^\circ}_l\mu^{c^\circ}_m = De_{klm}, \qquad D = \det\left|\mu^{a^\circ}_l\right| \tag{3.15}$$

and utilizing equation (3.14) we can write:

$$\mathrm{d}A_k = \mu^{a^\circ}_k\,\mathrm{d}A_{a^\circ} = \varepsilon^\circ_{abc}\mu^{a^\circ}_k\mu^{b^\circ}_l\mu^{c^\circ}_m\mathrm{d}x^l_{\mathrm{I}}\mathrm{d}x^m_{\mathrm{II}} = D\mathrm{d}A^\circ_{k^\circ}, \tag{3.16}$$

where with regard to (3.3) and (3.13)

$$\mathrm{d}A^\circ_{k^\circ} = \varepsilon^\circ_{klm}\mathrm{d}x^l_{\mathrm{I}}\mathrm{d}x^m_{\mathrm{II}}. \tag{3.17}$$

As a consequence the surface element vector $\mathrm{d}\mathbf{A}$ at point P can be given with the aid of $\mathrm{d}\mathbf{A}^\circ$ at point P°. With a view to (3.8) and (3.16), it follows from (3.14) that:

$$\mathrm{d}\mathbf{A} = \mathrm{d}A_k\mathbf{g}^k = \mathrm{d}A_{a^\circ}\mathbf{g}^{\circ a} = \boldsymbol{W}^\circ\cdot\mathrm{d}\mathbf{A}^\circ, \quad \boldsymbol{W}^\circ = W^{\circ\,h^\circ}_{a^\circ}\mathbf{g}^{\circ a}\mathbf{g}^\circ_h, \tag{3.18}$$

$$\mathrm{d}A_{a^\circ} = W^{\circ\,h^\circ}_{a^\circ}\mathrm{d}A^\circ_{h^\circ}, \qquad W^{\circ\,h^\circ}_{a^\circ} = \frac{1}{2}e_{abc}e^{hij}\mu^{b^\circ}_i\mu^{c^\circ}_j, \tag{3.19}$$

$$\mathrm{d}A_k = D\mathrm{d}A^\circ_{k^\circ}. \tag{3.20}$$

REMARK 3.4. Relationships (3.18)-(3.20) are valid independently of the orientation of $\mathrm{d}\mathbf{A}^\circ$.

Derivation of the third relationship we planned to set up at the beginning of Section 3 can be carried out as follows. Writing equation (3.7) as

$$\mathrm{d}\overline{\mathbf{A}} = \mathbf{g}^{\circ a}\varepsilon^\circ_{abc}\mu^{b^\circ}_l(\delta^l_s + u^l_{;s})\mu^{c^\circ}_m(\delta^m_t + u^m_{;t})\mathrm{d}x^s_{\mathrm{I}}\mathrm{d}x^t_{\mathrm{II}}$$

and introducing the notations

$$\mathbf{u} = u^l\mathbf{g}_l = u^{b^\circ}\mathbf{g}^\circ_b, \quad \mu^{b^\circ}_l u^l_{;s} = u^{b^\circ}_{;s} \tag{3.21}$$

$$u^{b^\circ}_{;\alpha} = u^{b^\circ}_{,\alpha} + \Gamma^{b^\circ}_{\alpha^\circ n^\circ}u^{n^\circ}, \quad u^{b^\circ}_{;3} = u^{b^\circ}_{,3} \tag{3.22}$$

we obtain, with a view to (3.8), the following relation:

$$\mathrm{d}\overline{\mathbf{A}} = \mathrm{d}\overline{A}_{a^\circ}\mathbf{g}^{\circ a} = \mathbf{g}^{\circ a}Q^{\circ\,h^\circ}_{a^\circ}\mathrm{d}A^\circ_{h^\circ}, \quad Q^{\circ\,h^\circ}_{a^\circ} = \frac{1}{2}e_{abc}e^{hij}(\mu^{b^\circ}_i + u^{b^\circ}_{;i})(\mu^{c^\circ}_j + u^{c^\circ}_{;j}). \tag{3.23}$$

where $\mathrm{d}A^\circ_{h^\circ}$ can be calculated from (3.17).

Finally we have a formula which relates $\mathrm{d}\overline{\mathbf{A}}$ taken at point $\overline{P}$ to $\mathrm{d}\mathbf{A}^\circ$ taken at point P°:

$$\mathrm{d}\overline{\mathbf{A}} = \mathrm{d}\overline{A}_{\overline{q}}\overline{\mathbf{g}}^q = \mathrm{d}\overline{A}_k\mathbf{g}^k = \mathrm{d}\overline{A}_{a^\circ}\mathbf{g}^{\circ a} = \boldsymbol{Q}^\circ\cdot\mathrm{d}\mathbf{A}^\circ, \quad \boldsymbol{Q}^\circ = Q^{\circ\,h^\circ}_{a^\circ}\mathbf{g}^{\circ a}\mathbf{g}^\circ_h, \tag{3.24}$$

$$\mathrm{d}\overline{A}_{a^\circ} = Q^{\circ\,h^\circ}_{a^\circ}\mathrm{d}A^\circ_{h^\circ}. \tag{3.25}$$

Then combining (3.11) and (3.20) we obtain:

$$\mathrm{d}\overline{A}_k = Q^h_k\mathrm{d}A_h = DQ^h_k\mathrm{d}A^\circ_{h^\circ}. \tag{3.26}$$

For shells we distinguish two special cases for the location of the surface element $\mathrm{d}\mathbf{A}^{\circ}$. In the first case the surface element $\mathrm{d}\mathbf{A}^{\circ}$ is on the base surface (A°) and in accordance with equation (3.3) we get

$$\mathrm{d}\mathbf{A}^{\circ} = \mathrm{d}A^{\circ}_{3^{\circ}}\mathbf{g}^{\circ 3} = \varepsilon^{\circ}_{3\sigma\tau}\mathrm{d}x^{\sigma}_{\mathrm{I}}\mathrm{d}x^{\tau}_{\mathrm{II}}\mathbf{g}^{\circ 3} \tag{3.27}$$

and

$$\mathrm{d}\overline{\mathbf{A}} = \mathrm{d}\overline{A}_{a^{\circ}}\mathbf{g}^{\circ a}, \qquad \mathrm{d}\overline{A}_{a^{\circ}} = Q^{\circ}_{a^{\circ}}{}^{3^{\circ}}\mathrm{d}A^{\circ}_{3^{\circ}} = \frac{1}{2}e_{abc}e^{3\eta\vartheta}(\mu^{b^{\circ}}_{\eta} + u^{b^{\circ}}_{;\eta})(\mu^{c^{\circ}}_{\vartheta} + u^{c^{\circ}}_{;\vartheta})\mathrm{d}A^{\circ}_{3^{\circ}}. \tag{3.28}$$

In the second case the surface elements $\mathrm{d}\overline{\mathbf{A}}$, $\mathrm{d}\mathbf{A}$ and $\mathrm{d}\mathbf{A}^{\circ}$ are situated on the side surface $\left(\overline{A}^{*}\right)$, or (A^{*}). Let us denote the surface elements by $\mathrm{d}\overline{\mathbf{A}}^{*}$, $\mathrm{d}\mathbf{A}^{*}$ and $\mathrm{d}\mathbf{A}^{\circ *}$ and the corresponding points by $\overline{P}^{*}$, P^{*} and $P^{\circ *}$, respectively. (A^{*}) is determined by the normal vector of the base surface (A°) on the boundary curve (g°). Assume that $x^{\vartheta} = x^{\vartheta}(s^{\circ})$ is the equation of the boundary curve (g°) on the base surface (A°). Then we can write the unit tangent and the unit normal to the surface (A^{*}) as

$$\mathbf{t}^{\circ} = \frac{\mathrm{d}\mathbf{r}^{\circ}}{\mathrm{d}s^{\circ}} = \frac{\partial\mathbf{r}^{\circ}}{\partial x^{\vartheta}}\frac{\mathrm{d}x^{\vartheta}}{\mathrm{d}s^{\circ}} = t^{\circ\vartheta}\mathbf{g}^{\circ}_{\vartheta}, \quad \mathbf{n}^{\circ} = \mathbf{t}^{\circ}\times\mathbf{g}^{\circ}_{3} = \varepsilon^{\circ}_{\eta\vartheta 3}t^{\circ\vartheta}\mathbf{g}^{\circ\eta} = n^{\circ}_{\eta}\mathbf{g}^{\circ\eta}. \tag{3.29}$$

The surface element at point P° of the curve (g°) on the side surface (A^{*}) is given by

$$\mathrm{d}\mathbf{A}^{\circ *} = (\mathbf{t}^{\circ}\mathrm{d}s^{\circ})\times\left(\mathbf{g}^{\circ}_{3}\mathrm{d}x^{3}\right) = \mathbf{n}^{\circ}\mathrm{d}s^{\circ}\mathrm{d}x^{3} = \mathrm{d}A^{\circ *}_{\eta^{\circ}}\mathbf{g}^{\circ\eta} \tag{3.30}$$

$$\mathrm{d}A^{\circ *}_{\eta^{\circ}} = n^{\circ}_{\eta^{\circ}}\mathrm{d}s^{\circ}\mathrm{d}x^{3} = \varepsilon^{\circ}_{\eta\vartheta 3}t^{\circ\vartheta}\mathrm{d}s^{\circ}\mathrm{d}x^{3}. \tag{3.31}$$

Similarly, at an arbitrary point $\overline{P}^{*}$ of the side surface $\left(\overline{A}^{*}\right)$ the surface element can be obtained from (3.25) and (3.26) and can be written as

$$\mathrm{d}\overline{A}^{*}_{a^{\circ}} = Q^{\circ *\eta^{\circ}}_{a^{\circ}}\mathrm{d}A^{\circ *}_{\eta^{\circ}}, \qquad \mathrm{d}\overline{A}^{*}_{k} = D^{*}Q^{*\eta}_{k}\mathrm{d}A^{\circ *}_{\eta^{\circ}}. \tag{3.32}$$

4. **Deformation dependent tractions**

4.1. An arbitrary coordinate system in configuration (B)**.** We define the traction on the surface part $\left(\overline{A}_{t}\right)$ of an arbitrary present configuration $\left(\overline{B}\right)$ as

$$\widetilde{p} = p\widetilde{p}_{\circ}, \quad x\in\left(\overline{A}_{t}\right), \tag{4.1}$$

where p is the load parameter and $\widetilde{p}_{\circ}$ is a reference traction regarded as positive if the traction points out of the surface.

The surface part $\left(\overline{A}_{t}\right)$ corresponds to (A_{t}) in configuration (B).

In accordance with (3.10) the force acting on the corresponding surface element is given by the formulae:

$$\mathrm{d}\overline{\mathbf{F}} = \widetilde{p}\mathrm{d}\overline{\mathbf{A}} = \widetilde{p}\boldsymbol{Q}\cdot\mathrm{d}\mathbf{A}\,, \tag{4.2}$$

$$\mathrm{d}\overline{F}_{\overline{q}} = \widetilde{p}\mathrm{d}\overline{A}_{\overline{q}}, \quad \mathrm{d}\overline{F}_{k} = \widetilde{p}\mathrm{d}\overline{A}_{k} = \widetilde{p}Q^{\,p}_{k}\mathrm{d}A_{p}\,. \tag{4.3}$$

REMARK 4.1. Tractions can be exerted on two or more surface parts simultaneously.

4.2. A coordinate system for shells in configuration (B)**.** The shell in configuration (B) is bounded by a top surface (A^+) and a bottom surface (A^-), which are given by the equations $b^+ = b^+\left(x^1, x^2\right)$, $b^- = b^-\left(x^1, x^2\right)$, and a side surface (A^*). The values of b^+ and b^- are measured along the normal vector $\mathbf{g}_3^\circ$ of the base surface (A°): $b^+ \geq x^3 \geq b^-$. The thickness of the shell is $b = b^+ - b^-$.

In the present configuration $\left(\overline{B}\right)$ the surfaces $\left(\overline{A}^+\right)$, $\left(\overline{A}^-\right)$ and $\left(\overline{A}^*\right)$ correspond to the top surface (A^+), bottom surface (A^-) and side surface (A^*).

We define the tractions on the surface parts $\left(\overline{A}_t^+\right)$ and $\left(\overline{A}_t^*\right)$ of an arbitrary present configuration $\left(\overline{B}\right)$ of the shell by

$$\widetilde{p}^+ = p^+ \widetilde{p}_\circ^+, \quad x \in \left(\overline{A}_t^+\right), \tag{4.4}$$

$$\widetilde{p}^* = p^* \widetilde{p}_\circ^*, \quad x \in \left(\overline{A}_t^*\right), \tag{4.5}$$

where p^+ and p^* are load parameters, and $\widetilde{p}_\circ^+$ and $\widetilde{p}_\circ^*$ are reference tractions regarded as positive, if the traction is directed out of the surface.

REMARK 4.2. Loads can be exerted on the bottom surface (A^-) as well.

In accordance with equations (3.10), (3.11) and (3.22), (3.23), the forces acting on the corresponding surface elements are given by the formulae:

$$\mathrm{d}\overline{\mathbf{F}}^+ = \widetilde{p}^+ \mathrm{d}\overline{\mathbf{A}}^+ = \widetilde{p}^+ \boldsymbol{Q}^+ \cdot \mathrm{d}\mathbf{A}^+ = \widetilde{p}^+ \boldsymbol{Q}^{\circ +} \cdot \mathrm{d}\mathbf{A}^{\circ +}, \tag{4.6}$$

$$\mathrm{d}\overline{F}_{\overline{q}}^+ = \widetilde{p}^+ \mathrm{d}\overline{A}_{\overline{q}}^+, \quad \mathrm{d}\overline{F}_k^+ = \widetilde{p}^+ \mathrm{d}\overline{A}_k^+ = \widetilde{p}^+ Q_k^{+\,p} \mathrm{d}A_k^+, \quad \mathrm{d}\overline{F}_{a^\circ}^+ = \widetilde{p}^+ \mathrm{d}\overline{A}_{a^\circ}^+ = \widetilde{p}^+ Q_{a^\circ}^{\circ +\;h^\circ} \mathrm{d}A_{h^\circ}^\circ \tag{4.7}$$

$$\mathrm{d}\overline{\mathbf{F}}^* = \widetilde{p}^* \mathrm{d}\overline{\mathbf{A}}^* = \widetilde{p}^* \boldsymbol{Q}^* \cdot \mathrm{d}\mathbf{A}^*, \tag{4.8}$$

$$\mathrm{d}\overline{F}_{\overline{q}}^* = \widetilde{p}^* \mathrm{d}\overline{A}_{\overline{q}}^*, \quad \mathrm{d}\overline{F}_k^* = \widetilde{p}^* \mathrm{d}\overline{A}_k^* = \widetilde{p}^* Q_k^{*\,h} \mathrm{d}A_h^*. \tag{4.9}$$

5. Calculation of the work increment

5.1. We apply the Lagrangian formulation in the reference configuration (B).

Let us introduce a *control parameter* τ and its increment $\Delta\tau$ to describe a small change of an equilibrium configuration $\left(\overline{B}\right)$ in the interval $0 \leq \tau \leq \Delta\tau$. The control parameter can be either a load parameter (e.g. p, p^+, p^*) or a displacement parameter.

We assume on the initiation made by Marcinowsky [5] that the variables in a small neighborhood of the equilibrium configuration $\left(\overline{B}\right)$ can be given by truncated Taylor expansions with respect to the control parameter (asymptotic numerical method).

The control parameter is regarded as quasi-time. In our problem

$$u^k(\tau) = u^k_{\mathrm{B}} + \Delta u^k_{\mathrm{B}} = u^k_{\mathrm{B}} + \dot{u}^k_{\mathrm{B}}\tau + \frac{1}{2}\ddot{u}^k_{\mathrm{B}}\tau^2 + \frac{1}{6}\dddot{u}^k_{\mathrm{B}}\tau^3 + \cdots, \tag{5.1}$$

$$p(\tau) = p_{\mathrm{B}} + \Delta p_{\mathrm{B}} = p_{\mathrm{B}} + \dot{p}_{\mathrm{B}}\tau + \frac{1}{2}\ddot{p}_{\mathrm{B}}\tau^2 + \frac{1}{6}\dddot{p}_{\mathrm{B}}\tau^3 + \cdots, \tag{5.2}$$

$$Q^{\,p}_{k}(\tau) = Q_{\mathrm{B}k}{}^{h} + \Delta Q_{\mathrm{B}k}{}^{h} = Q_{\mathrm{B}k}{}^{h} + \dot{Q}_{\mathrm{B}k}{}^{h}\tau + \frac{1}{2}\ddot{Q}_{\mathrm{B}k}{}^{h}\tau^2 + \frac{1}{6}\dddot{Q}_{\mathrm{B}k}{}^{h}\tau^3 + \cdots, \tag{5.3}$$

where a dot (or dots) above a variable denotes differentiation with respect to a control parameter, $\Delta\tau$ belongs to the displacement increment Δu^k_{B}, which determines the configuration $\left(\overline{B} + \Delta\overline{B}\right)$. The subscript B means that the quantity in question is defined in the equilibrium configuration $\left(\overline{B}\right)$.

In accordance with equation (3.9) we can write

$$Q_{\mathrm{B}k}{}^{p} = \frac{1}{2}e_{klm}e^{pqr}(\delta^l_q + u_{\mathrm{B}}{}^{l}{}_{;q})(\delta^m_r + u_{\mathrm{B}}{}^{m}{}_{;r}), \tag{5.4}$$

$$\dot{Q}_{\mathrm{B}k}{}^{p} = e_{klm}e^{pqr}(\delta^l_q + u_{\mathrm{B}}{}^{l}{}_{;q})\dot{u}_{\mathrm{B}}{}^{m}{}_{;r}, \tag{5.5}$$

$$\ddot{Q}_{\mathrm{B}k}{}^{p} = e_{klm}e^{pqr}\left[(\delta^l_q + u_{\mathrm{B}}{}^{l}{}_{;q})\ddot{u}_{\mathrm{B}}{}^{m}{}_{;r} + \dot{u}_{\mathrm{B}}{}^{l}{}_{;q}\dot{u}_{\mathrm{B}}{}^{m}{}_{;r}\right], \tag{5.6}$$

$$\dddot{Q}_{\mathrm{B}k}{}^{p} = e_{klm}e^{pqr}\left[(\delta^l_q + u_{\mathrm{B}}{}^{l}{}_{;q})\dddot{u}_{\mathrm{B}}{}^{m}{}_{;r} + 3\ddot{u}_{\mathrm{B}}{}^{l}{}_{;q}\dot{u}_{\mathrm{B}}{}^{m}{}_{;r}\right]. \tag{5.7}$$

5.2. An arbitrary coordinate system in configuration (B)**.** Using formulae (4.2), (4.3) and (5.1), (5.3) for the power of the traction (4.1) in the equilibrium configuration $\left(\overline{B}\right)$ and in the interval $0 \le \tau \le \Delta\tau$ we can writte

$$\begin{aligned} P(\tau) &= p_{\mathrm{B}}\int_{(A_t)}\widetilde{p}_{\circ}\dot{\mathbf{u}}(\tau)\cdot\mathrm{d}\overline{\mathbf{A}} = P(\tau) = p_{\mathrm{B}}\int_{(A_t)}\widetilde{p}_{\circ}\dot{\mathbf{u}}(\tau)\cdot\mathrm{d}\overline{\mathbf{A}} = \\ &= p_{\mathrm{B}}\int_{(A_t)}\widetilde{p}_{\circ}\dot{\mathbf{u}}(\tau)\cdot\boldsymbol{Q}(\tau)\cdot\mathrm{d}\mathbf{A} = p_{\mathrm{B}}\int_{(A_t)}\widetilde{p}_{\circ}\dot{u}^k(\tau)\,Q^{\,p}_{k}(\tau)\,\mathrm{d}A_p = \\ &= p_{\mathrm{B}}\int_{(A_t)}\widetilde{p}_{\circ}\left(\dot{u}^k_{\mathrm{B}} + \ddot{u}^k_{\mathrm{B}}\tau + \frac{1}{2}\dddot{u}^k_{\mathrm{B}}\tau^2 + \cdots\right)\left(Q_{\mathrm{B}k}{}^{p} + \dot{Q}_{\mathrm{B}k}{}^{p}\tau + \frac{1}{2}\ddot{Q}_{\mathrm{B}k}{}^{p}\tau^2 + \cdots\right)\mathrm{d}A_p\,. \end{aligned} \tag{5.8}$$

The work increment of the traction in interval $0 \le \tau \le \Delta\tau$ can be determined by integrating the power $P(\tau)$ with respect to τ:

$$\begin{aligned} \Delta W &= \int_{\tau=0}^{\Delta\tau} P(\tau)\,\mathrm{d}\tau = \\ &= p_{\mathrm{B}}\left[\int_{(A_t)}\widetilde{p}_{\circ}\dot{u}^k_{\mathrm{B}}Q_{\mathrm{B}k}{}^{p}\mathrm{d}A_p\right]\Delta\tau + \\ &+ p_{\mathrm{B}}\left[\int_{(A_t)}\widetilde{p}_{\circ}\left(\dot{u}^k_{\mathrm{B}}\dot{Q}_{\mathrm{B}k}{}^{p} + \ddot{u}^k_{\mathrm{B}}Q_{\mathrm{B}k}{}^{p}\right)\mathrm{d}A_p\right]\frac{1}{2}(\Delta\tau)^2 + \\ &+ p_{\mathrm{B}}\left[\int_{(A_t)}\widetilde{p}_{\circ}\left(\dot{u}^k_{\mathrm{B}}\ddot{Q}_{\mathrm{B}k}{}^{p} + 2\ddot{u}^k_{\mathrm{B}}\dot{Q}_{\mathrm{B}k}{}^{p} + \dddot{u}^k_{\mathrm{B}}Q_{\mathrm{B}k}{}^{p}\right)\mathrm{d}A_p\right]\frac{1}{6}(\Delta\tau)^3 + \cdots. \end{aligned} \tag{5.9}$$

If one applies a finite element discretization ΔW can be given – in a view of (5.4)-(5.7) and (5.9) – in terms of $\underline{\mathbf{t}}_{\mathrm{B}}$ and its derivatives $\dot{\underline{\mathbf{t}}}_{\mathrm{B}}$, $\ddot{\underline{\mathbf{t}}}_{\mathrm{B}}$, $\dddot{\underline{\mathbf{t}}}_{\mathrm{B}}$, $\cdots$ taken with respect to the displacement parameter $\underline{\mathbf{t}}$.

5.3. A coordinate system for shells in configuration (B)**.** Geometrically nonlinear shell theories differ from each other mainly in the applied kinematic assumptions (see, e.g., Basar and Ding [6], Parisch [7], Sansour and Kollmann [8]). In this paper the analysis of the geometrically nonlinear shells is out of scope, therefore we adopt a displacement field without reasoning. Let the displacement be given at an arbitrary point P of the configuration (B) as

$$\begin{gathered}\mathbf{u} = u^k \mathbf{g}_k = u^{a^\circ} \mathbf{g}^\circ_a,\\ \mathbf{u} = \mathbf{v}^\circ + \mathbf{w}^\circ x^3 + \mathbf{q}^\circ \left(x^3\right)^2 + \mathbf{s}^\circ \left(x^3\right)^3,\\ u^{a^\circ} = v^{\circ a^\circ} + w^{\circ a^\circ} x^3 + q^{\circ a^\circ} \left(x^3\right)^2 + s^{\circ a^\circ} \left(x^3\right)^3 \end{gathered} \tag{5.10}$$

where the functions $\mathbf{v}^\circ$, $\mathbf{w}^\circ$, $\mathbf{q}^\circ$ and $\mathbf{s}^\circ$ are defined on the base surface (A°). With a view to (5.1) and (5.3) we can write

$$u^{a^\circ}(\tau) = u_{\mathrm{B}}^{a^\circ} + \Delta u_{\mathrm{B}}^{a^\circ} = u_{\mathrm{B}}^{a^\circ} + \dot{u}_{\mathrm{B}}^{a^\circ}\tau + \frac{1}{2}\ddot{u}_{\mathrm{B}}^{a^\circ}\tau^2 + \frac{1}{6}\dddot{u}_{\mathrm{B}}^{a^\circ}\tau^3 + \cdots, \tag{5.11}$$

$$Q^{\circ\, h^\circ}_{a^\circ}(\tau) = Q^{\circ}_{\mathrm{B}a^\circ}{}^{h^\circ} + \Delta Q^{\circ}_{\mathrm{B}a^\circ}{}^{h^\circ} = Q^{\circ}_{\mathrm{B}a^\circ}{}^{h^\circ} + \dot{Q}^{\circ}_{\mathrm{B}a^\circ}{}^{h^\circ}\tau + \frac{1}{2}\ddot{Q}^{\circ}_{\mathrm{B}a^\circ}{}^{h^\circ}\tau^2 + \frac{1}{6}\dddot{Q}^{\circ}_{\mathrm{B}a^\circ}{}^{h^\circ}\tau^3 + \cdots \tag{5.12}$$

and in accordance with (3.23) it follows

$$Q^{\circ}_{\mathrm{B}a^\circ}{}^{h^\circ} = \frac{1}{2} e_{abc} e^{hij} (\mu_{\mathrm{B}i}{}^{b^\circ} + u_{\mathrm{B}}{}^{b^\circ}{}_{;i})(\mu_{\mathrm{B}j}{}^{c^\circ} + u_{\mathrm{B}}{}^{c^\circ}{}_{;j}), \tag{5.13}$$

$$\dot{Q}^{\circ}_{\mathrm{B}a^\circ}{}^{h^\circ} = e_{abc} e^{hij} (\mu_{\mathrm{B}i}{}^{b^\circ} + u_{\mathrm{B}}{}^{b^\circ}{}_{;i}) \dot{u}_{\mathrm{B}}{}^{c^\circ}{}_{;j}, \tag{5.14}$$

$$\ddot{Q}^{\circ}_{\mathrm{B}a^\circ}{}^{h^\circ} = e_{abc} e^{hij} \left[(\mu_{\mathrm{B}i}{}^{b^\circ} + u_{\mathrm{B}}{}^{b^\circ}{}_{;i}) \ddot{u}_{\mathrm{B}}{}^{c^\circ}{}_{;j} + \dot{u}_{\mathrm{B}}{}^{b^\circ}{}_{;i} \dot{u}_{\mathrm{B}}{}^{c^\circ}{}_{;j} \right], \tag{5.15}$$

$$\dddot{Q}^{\circ}_{\mathrm{B}a^\circ}{}^{h^\circ} = e_{abc} e^{hij} \left[(\mu_{\mathrm{B}i}{}^{b^\circ} + u_{\mathrm{B}}{}^{b^\circ}{}_{;i}) \dddot{u}_{\mathrm{B}}{}^{c^\circ}{}_{;j} + 3\ddot{u}_{\mathrm{B}}{}^{b^\circ}{}_{;i} \dot{u}_{\mathrm{B}}{}^{c^\circ}{}_{;j} \right], \tag{5.16}$$

where, e.g.,

$$\dot{u}_{\mathrm{B}}^{a^\circ} = \dot{v}_{\mathrm{B}}^{\circ a^\circ} + \dot{w}_{\mathrm{B}}^{\circ a^\circ} x^3 + \dot{q}_{\mathrm{B}}^{\circ a^\circ} \left(x^3\right)^2 + \dot{s}_{\mathrm{B}}^{\circ a^\circ} \left(x^3\right)^3. \tag{5.17}$$

5.3.1. The loaded surfaces $\left(\overline{A_t^+}\right)$, $\left(A_t^+\right)$ and $\left(A_t^{\circ +}\right)$ belong together. Making use of equations (4.7) and (5.11), (5.12) for the power of the traction (4.4) acting on the surface part $\left(\overline{A_t^+}\right)$ in the equilibrium configuration $\left(\overline{B}\right)$ and in the interval

$0 \leq \tau \leq \Delta\tau$ we can write

$$P(\tau) = p_{\mathrm{B}}^{+} \int_{\left(\bar{A}_t^{+}\right)} \widetilde{p}_{\circ}^{+} \dot{\mathbf{u}}^{+}(\tau) \cdot \mathrm{d}\overline{\mathbf{A}} = p_{\mathrm{B}}^{+} \int_{\left(A_t^{\circ +}\right)} \widetilde{p}_{\circ}^{+} \dot{u}^{+a^{\circ}}(\tau)\, Q_{a^{\circ}}^{\circ + h^{\circ}}(\tau)\, \mathrm{d}A_{h^{\circ}}^{\circ} =$$
$$= p_{\mathrm{B}}^{+} \int_{\left(A_t^{\circ +}\right)} \widetilde{p}_{\circ}^{+} \left(\dot{u}_{\mathrm{B}}^{+a^{\circ}} + \ddot{u}_{\mathrm{B}}^{+a^{\circ}} \tau + \frac{1}{2} \dddot{u}_{\mathrm{B}}^{+a^{\circ}} \tau^2 + \cdots \right) \cdot$$
$$\cdot \left(Q_{\mathrm{B}a^{\circ}}^{\circ + h^{\circ}} + \dot{Q}_{\mathrm{B}a^{\circ}}^{\circ + h^{\circ}} \tau + \frac{1}{2} \ddot{Q}_{\mathrm{B}a^{\circ}}^{\circ + h^{\circ}} \tau^2 + \cdots \right) \mathrm{d}A_{h^{\circ}}^{\circ}, \tag{5.18}$$

where in accordance with (5.17), e.g.,

$$\dot{u}_{\mathrm{B}}^{+a^{\circ}} = \dot{v}_{\mathrm{B}}^{\circ a^{\circ}} + \dot{w}_{\mathrm{B}}^{\circ a^{\circ}} b^{+} + \dot{q}_{\mathrm{B}}^{\circ a^{\circ}} \left(b^{+}\right)^2 + \dot{s}_{\mathrm{B}}^{\circ a^{\circ}} \left(b^{+}\right)^3, \tag{5.19}$$

and with a view to (5.14), (2.4) and (5.10), (5.17) we have e.g.,

$$\dot{Q}_{\mathrm{B}a^{\circ}}^{\circ + h^{\circ}} = e_{abc} e^{hij} \left\{ \left[\delta_i^b - b_i^{\circ b} b^{+} + v_{\mathrm{B};i}^{\circ b^{\circ}} + w_{\mathrm{B};i}^{\circ b^{\circ}} b^{+} + q_{\mathrm{B};i}^{\circ b^{\circ}} \left(b^{+}\right)^2 + s_{\mathrm{B};i}^{\circ b^{\circ}} \left(b^{+}\right)^3 \right] \cdot \right.$$
$$\left. \cdot \left[\dot{v}_{\mathrm{B};j}^{\circ c^{\circ}} + \dot{w}_{\mathrm{B};j}^{\circ c^{\circ}} b^{+} + \dot{q}_{\mathrm{B};j}^{\circ c^{\circ}} \left(b^{+}\right)^2 + \dot{s}_{\mathrm{B};j}^{\circ c^{\circ}} \left(b^{+}\right)^3 \right] \right\}. \tag{5.20}$$

The work increment of the traction in the interval $0 \leq \tau \leq \Delta\tau$ can be obtained by integrating the power $P(\tau)$ with respect to τ:

$$\Delta W = \int_{\tau=0}^{\Delta\tau} P(\tau)\, \mathrm{d}\tau. \tag{5.21}$$

This formula can also be detailed if we take equations (5.10) and (5.13)-(5.16) into account.

5.3.2. In the special case when the side surface $\left(\overline{A}^{*}\right)$ is subjected to tractions we can also set up the required relationships. Using formula (3.25) for the power of the traction (4.5) exerted on the surface part $\left(\overline{A}_t^{*}\right)$ in the equilibrium configuration $\left(\overline{B}\right)$ and in the interval $0 \leq \tau \leq \Delta\tau$ we obtain

$$P(\tau) = p_{\mathrm{B}}^{*} \int_{\left(\bar{A}_t^{*}\right)} \widetilde{p}_{\circ}^{*} \dot{\mathbf{u}}^{*}(\tau) \cdot \mathrm{d}\overline{\mathbf{A}}^{*} = p_{\mathrm{B}}^{*} \int_{\left(A_t^{*}\right)} \widetilde{p}_{\circ}^{*} \dot{u}^{*a^{\circ}}(\tau)\, Q_{a^{\circ}}^{\circ * \eta^{\circ}}(\tau)\, \mathrm{d}A_{\eta^{\circ}}^{\circ *}.$$

In view of (3.31), the surface integral can be decomposed into two line integrals. Integration is performed in two steps, first along the thickness and then on the part (g_t°) of the boundary curve (g°) – this part belongs to (A_t^{*}):

$$P(\tau) = p_{\mathrm{B}}^{*} \int_{(g_t^{\circ})} \left[\int_{(b)} \widetilde{p}_{\circ}^{*} \dot{u}^{*a^{\circ}}(\tau)\, Q_{a^{\circ}}^{\circ * h^{\circ}}(\tau)\, \mathrm{d}x^3 \right] \varepsilon_{\eta\vartheta 3}^{\circ} t^{\circ\vartheta} \mathrm{d}s^{\circ}. \tag{5.22}$$

The work increment ΔW is obtained by integrating the power $P(\tau)$ with respect to τ in the interval $0 \leq \tau \leq \Delta\tau$:

$$\Delta W = \int_{\tau=0}^{\Delta\tau} P(\tau)\,\mathrm{d}\tau =$$

$$= p_{\mathrm{B}}^{*} \int_{(g_t^{\circ})} \left\{ \int_{(b)} \widetilde{p}_{\circ}^{*} \left[\int_{\tau=0}^{\Delta\tau} \dot{u}^{*a^{\circ}}(\tau)\, Q_{a^{\circ}}^{\circ *h^{\circ}}(\tau)\,\mathrm{d}\tau \right] \mathrm{d}x^{3} \right\} \varepsilon_{\eta\vartheta 3}^{\circ} t^{\circ\vartheta}\,\mathrm{d}s^{\circ}. \tag{5.23}$$

In order to detail the integration across the thickness in (5.22) we should use equations (5.11), (5.12), (5.13)-(5.16) and (5.10).

REMARK 5.1. It is worth emphasizing that calculation of the work increment done by the tractions in an equilibrium configuration $\left(\overline{B}\right)$ during a kinematically admissible displacement $\Delta u_{\mathrm{B}}^{k}$ is determined by the derivatives $\dot{u}_{\mathrm{B}}^{k}$, $\ddot{u}_{\mathrm{B}}^{k}$, $\dddot{u}_{\mathrm{B}}^{k}$,... in (5.1). Numerical computations can be performed e.g., by the finite element method.

REMARK 5.2. When the computation of ΔW is to be performed on an equilibrium path by means of the incremental form of the principle of virtual work, we have to determine $\dot{u}_{\mathrm{B}}^{k}$, $\ddot{u}_{\mathrm{B}}^{k}$, $\dddot{u}_{\mathrm{B}}^{k}$,... in advance as functions of $\dot{p}_{\mathrm{B}}$, $\ddot{p}_{\mathrm{B}}$, $\dddot{p}_{\mathrm{B}}$,... which define Δp_{B}. The computations can also be carried out by the finite element method.

6. **Conclusions**

The well-known Nanson formula gives a relationship between the surface elements $\mathrm{d}\mathbf{A}$ and $\mathrm{d}\overline{\mathbf{A}}$ taken at the points P and $\overline{P}$ of the reference configuration (B) and present configuration $\left(\overline{B}\right)$, respectively.

Making use of the Nanson formula a relationship has been found for shells between the surface elements $\mathrm{d}\mathbf{A}^{\circ}$ and $\mathrm{d}\overline{\mathbf{A}}$. The surface element $\mathrm{d}\mathbf{A}^{\circ}$ with an arbitrary orientation is associated with the point P° of the base surface (A°) of a shell in configuration (B) while the surface element $\mathrm{d}\overline{\mathbf{A}}$ is associated with the point $\overline{P}$ of configuration $\left(\overline{B}\right)$. As a special case we have investigated what happens when $\mathrm{d}\mathbf{A}^{\circ}$ is loacated either on the base surface (A°) or on the side surface (A^{*}).

The geometric variables in a small neighborhood of the equilibrium configuration $\left(\overline{B}\right)$ can be given by truncated Taylor expansions with respect to a control parameter. The control parameter is regarded as quasi-time. In this way the displacement field and the surface element vectors can be regarded as functions of a control parameter (control parameters) in a small neighborhood of the configuration $\left(\overline{B}\right)$. We have preferred the total Lagrangian formulation in which the variables are defined at the points of the reference configuration (B).

Using the relationship set up for the surface element vectors calculation of the work increment ΔW done by the deformation dependent normal traction $\widetilde{p}$ during a displacement increment $\Delta\overline{\mathbf{u}}$ requires calculation of integrals taken on the surface of configuration (B). The traction $\widetilde{p}$ is exerted on the surface part $\left(\overline{A}_t\right)$ of configuration $\left(\overline{B}\right)$, and the displacement increment $\Delta\overline{\mathbf{u}}$ is measured in a small neighborhood of configuration $\left(\overline{B}\right)$.

In special cases, i.e., for shells the surface integrals are calculated either on the base surface (A°) or on the side surface (A^*) depending on which surface part is loaded.

Acknowledgement. The support provided by the Hungarian National Research Foundation (project No.: OTKA T031998) is gratefully acknowledged.

References

1. Molk, D.P., Wall, W.A., Bischoff, M. and Ramm, E.: *Algorithmic aspects of deformation dependent loads in non-linear static finite element analysis*, Engineering Computation, **16**, (1999), 601-618.
2. Kozák, I., Nándori, F. and Szabó, T.: *FE analysis of geometrically nonlinear static problems with follower loads*, Computer Assisted Mechanics and Engineering Sciences, **6**, (1999), 369-383.
3. Béda, Gy., Kozák, I. and Verhás, J.: *Continuum Mechanics*, Akadémiai Kiadó, Budapest, 1995, p. 314.
4. Mason, J.: *Variational, Incremental and Energy Methods in Solid Mechanics and Shell Theory*, Elsevier, Amsterdam - Oxford - New York, 1980, p. 368.
5. Marcinowsky, M.: *Large deflections of shells subjected to external load and temperature changes*, International Journal of Solids and Structures, **34**, (1997), 755-768.
6. Basar, Y. and Ding, Y.: *Shear deformation models for large strain shell analysis*, International Journal of Solids and Structures, **34**, (1997), 1687-1708.
7. Parisch, H.: *A continuum based shell theory for nonlinear application*, Int. J. Solids and Structures, **38**, (1995), 1855-1883.
8. Sansour, C. and Kollmann, F. G.: *Families of 4-node and 9-node finite elements for a finite deformation shell theory. An assessment of hybrid stress, hybrid strain elements*, Computational Mechanics, **24**, (2000), 435-447.

Journal of Computational and Applied Mechanics, Vol. 3., No. 1., (2002), pp. 51–60

CONTACT PROBLEM FOR THE AUTOFRETTAGE OF THICK CYLINDERS

Gennadiy Lvov and Sergey Lysenko
Kharkov Polytechnic University
310002 Kharkov, 21 Frunze Str., Ukraine
lvovgi@kpi.kharkov.ua

[Received: October 4, 2001]

Abstract. The autofrettage of thick-walled cylinders with variable thickness is considered on the basis of a variational formulation of the corresponding elastic-plastic contact problem. The numerical solution is determined by the use of the finite element method. We have chosen a material model which takes kinematic hardening and the ideal Baushinger effect into account. The optimum geometric parameters for the bandage and the initial gap are both determined in a way that a favorable distribution of residual stresses will develop and the bandage is removed after unloading.

Mathematical Subject Classification: 74M15, 74S0
Keywords: autofrettage, finite element method, contact problem, residual stresses

1. Introduction

Thick-walled cylinders subjected to high impulsive pressure are wide-spread as elements of many important constructions. When the magnitude of pressure is commensurable with the yield point of the material, a raise of strength can be reached by the special methods of the autofrettage. In an outcome of the intended plastic deformations caused by the interior pressure acting in the cylinders a favourable field of residual stresses is developed.

In works [1-3] the process of forming residual stresses is investigated for a broad class of materials with various types of deformation diagrams.

The magnitude of residual stresses depends on what sizes the areas of plastic deformations have and on the differences in character between the stress distributions in plastic and elastic conditions.

The possibilities for the autofrettage are frequently limited by the strength of the cylinders during plastic loading. Such a restriction is especially essential for cylinders with various wall thicknesses because the creation of irregular technological pressure for the autofrettage entails significant engineering difficulties.

It is expedient to apply technological bandages for restriction of strains of cylinders in areas with a smaller thickness of walls for raising the effectiveness of autofrettage

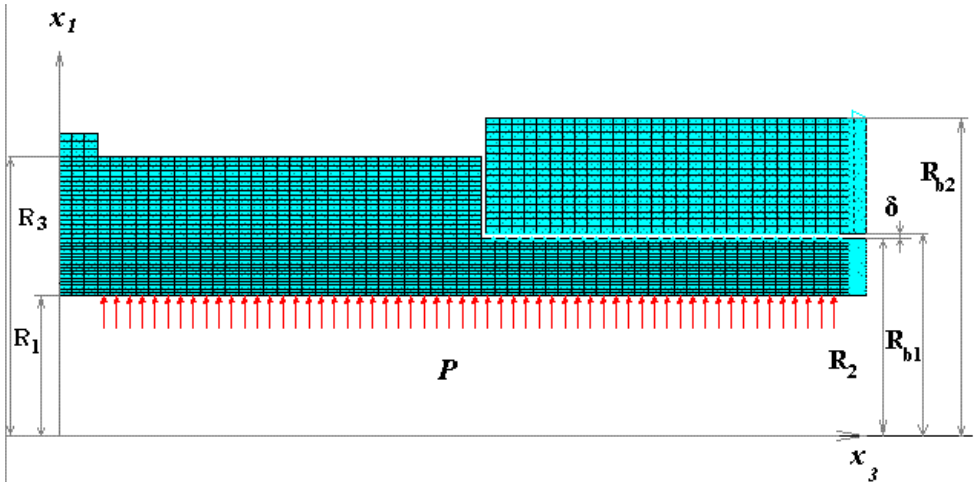

Figure 1. Finite element model of a composite construction

in cylinders of a variable thickness. The scheme of such an autofrettage with uniform pressure and one restraining bandage is shown in Figure 1.

2. Description of investigation of autofrettage

The theoretical analysis of a process of autofrettage is reduced to the solution of an elastic-plastic problem which includes loading and unloading by taking the contact interaction of the cylinder and technological bandage into consideration.

Let's consider such a problem for two bodies of revolution assuming axisymmetric deformations. During loading and unloading the stress increments $d\sigma_{11}, \ldots, d\sigma_{13}$ of the deformed solid bodies should satisfy the equilibrium equations

$$\frac{\partial}{\partial x_1}(d\sigma_{11}) + \frac{\partial}{\partial x_3}(d\sigma_{31}) + \frac{d\sigma_{11} - d\sigma_{22}}{x_1} = 0\,, \tag{2.1a}$$

$$\frac{\partial}{\partial x_3}(d\sigma_{33}) + \frac{\partial}{\partial x_1}(d\sigma_{31}) + \frac{1}{x_1} d\sigma_{13} = 0\,. \tag{2.1b}$$

The surface S of each body can be presented as a union of two surfaces: $S = S_F \cup S_K$, where S_F is the surface on which the increments of the exterior forces are given, and S_K is the contact region between the cylinder and the bandage.

The exterior surface of the cylinder is given by the parametrical equations $x_1 = x_1(\alpha)$, $x_3 = x_3(\alpha)$, where α is the length of the meridian curve in initial condition.

The interior surface of the bandage, where contact is possible, is given by the equation $f(x_1, x_3) = 0$. The kinematic condition on the displacement increments dU_C and dU_B in the cylinder and bandage due to the interaction assumes the form of an inequality:

$$f(x_1, x_3) + \operatorname{grad} f \cdot (U_C + dU_C) - \operatorname{grad} f \cdot (U_B + dU_B) \leqslant 0\,. \tag{2.2}$$

Condition (2.2) is equality in the contact zone.

The strain increments $d\varepsilon_{11}, \ldots, d\varepsilon_{13}$ are related to the displacements u_1, u_3 via linear equations:

$$d\varepsilon_{11} = \frac{\partial}{\partial x_1}(du_1)\,, \quad d\varepsilon_{22} = \frac{1}{x_1}(du_1)\,, \tag{2.3a}$$

$$d\varepsilon_{33} = \frac{\partial}{\partial x_3}(du_3)\,, \quad d\varepsilon_{13} = \frac{1}{2}\left[\frac{\partial}{\partial x_1}(du_3) + \frac{\partial}{\partial x_3}(du_1)\right]\,. \tag{2.3b}$$

The deformation trajectories in the autofrettage processes have a complicated character. During unloading secondary plastic deformations may emerge with an opposite sign. Under the conditions of contact interaction the loading process will not be simple even for a monotone increase of the exterior load.

For an adequate description of the plastic deformations it is necessary to use physical relations reflecting the Baushinger effect and the directed character of hardening. As the physical relations satisfying the conditions mentioned for one cycle of loading and unloading we have selected the theory of plasticity with anisotropic hardening [4,5]. The increment of plastic deformations $d\varepsilon_{ij}^p$ is determined by the law

$$d\varepsilon_{ij}^p = d\lambda \cdot \frac{\partial \varphi}{\partial \sigma_{ij}}\,, \tag{2.4}$$

in which $d\lambda$ is a parameter to be determined,

$$\varphi = \frac{3}{2}\,(S_{ij} - \rho_{ij}) \cdot (S_{ij} - \rho_{ij}) - \sigma_y^2 = 0 \tag{2.5}$$

is the surface of plasticity, $S_{ij} = \sigma_{ij} - \delta_{ij}\sigma_0$ denotes the stress deviator (σ_0 is the first scalar invariant of the stress tensor), σ_y is the yield stress in the initial state. The character of directed hardening is determined by the deviator ρ_{ij} obtained from the accumulated plastic deformations:

$$\rho_{ij} = \int C\,(\varepsilon_i^p)\, d\varepsilon_{ij}^p\,. \tag{2.6}$$

The integral is calculated on the loading path. If C is constant the hardening is linear. The multilinear law of hardening corresponds to a discrete combination of the values $C_k\,(\varepsilon^p)$, where C_k has a constant value for every separate section of approximation for the deformation diagram.

The position of a surface of plasticity is determined by the history of plastic deformations, but the hardening is transmitted which corresponds to the ideal Baushinger effect.

The increment of plastic deformations can be given in terms of the stress increments

$$d\varepsilon_{ij}^p = \frac{(S_{mn} - \rho_{mn}) \cdot d\sigma_{mn}}{3 \cdot C \cdot (S_{kl} - \rho_{kl}) \cdot (S_{kl} - \rho_{kl})}\,(S_{ij} - \rho_{ij})\,. \tag{2.7}$$

If the conditions for active loading are not satisfied, the increment of plastic deformations is equal to zero.

For each stage of the autofrettage process determination of the displacement, stress and strain increments requires the integration of a boundary value problem defined by

the field equations (2.1), (2.3) and (2.7), which should be associated with appropriate boundary conditions and the kinematic restriction for the contact interaction (2.2).

The problem is a nonlinear one since during the solution it is necessary to determine the boundaries of the contact area and the character of loading for both cylinders.

For a numerical solution by the finite element method the problem is reduced to an extremum problem for a functional defined on the kinematically admissible displacement increments which should also satisfy inequality (2.2):

$$\min J\left(dU_C,\, dU_B\right) = \frac{1}{2}\iiint\limits_{V_C+V_B} d\sigma_{ij}\, d\varepsilon_{ij}\, dV - \iint\limits_{S_F} dU_C\, dp\, dS. \tag{2.8}$$

In this functional $d\varepsilon_{ij}$ is determined by the kinematic relations (2.3) and $d\sigma_{ij}$ is obtained from the inverse of relation (2.7). Equivalence of the extremum problem (2.8) to the contact problem follows from the theory of variational inequalities [6, 7].

3. **Results**

The numerical solution is determined by the finite element method for an axisymmetric autofrettage of the cylinder. The bandage has a cylindrical form. The initial geometric parameters of the construction have the following values (see Figure 1):

- the interior radius of cylinder R_1= 0.06 m;
- the exterior small radius of cylinder R_2 = 0.092 m;
- the exterior large radius of cylinder R_3 = 0.138 m;
- the interior radius of bandage R_{b1} = 0.093 m;
- the exterior radius of bandage R_{b2} = 0.16 m;
- the length of cylinder L = 0.525 m; the length of bandage L_b = 0.247m;
- the initial gap between the surfaces of the cylinder and bandage δ= 0.001 m.
- the residual gap between the surfaces of the cylinder and bandage β=0.052 mm.

The finite element model of the composite construction is made of axisymmetric solid elements with four nodal points which have two degrees of freedom (U_{x1}, U_{x3}). The coordinate x_3 corresponds to the rotational axis, and the coordinate x_1 is measured in the radial direction. The second order shape functions are used. For modelling the contact interaction between the surfaces of the cylinder and bandage, which in the initial non-loaded condition are separated by a gap δ, the axisymmetric three-nodal contact elements of the type "a knot to a surface" were used. The contact surface is modelled with the help of the pseudo-element technology. This surface can interact during the elasto-plastic loading and unloading. In Figure 1 the finite element model is shown. This includes 2058 axisymmetric elements (1538 for the cylinder and 480 for bandage), and also 38 contact elements between surfaces of the cylinder and the bandage.

The technological autofrettage process is produced by the interior hydraulic pressure exerted on the inner surface of the cylinder.

For carrying out the computations we have chosen the following data for the materials of the cylinder and bandage: modulus of elasticity $\mathrm{E} = 0.21 \cdot 10^6$ MPa; Poisson's constant $\nu = 0,29$; yield stress $\sigma_{\mathrm{y}} = 1200$ MPa; the strength $\sigma_B = 1500$ MPa. The deformation diagram $\sigma\,(\varepsilon)$ is assumed to be multilinear. The four sections of the diagram are given by point: $\sigma_k = 1200, 1400, 1500, 1900$ MPa; $\varepsilon_k = 0,0057, 0,02, 0,05, 0,43$.

The step by step loading of the cylindrical pipe by pressure autofrettage was applied in an interactive procedure with adjusting the loading steps automatically to solve the physically and structurally non-linear problem. In addition, we have assumed that the load follows a linear law in each step. Such a solution procedure for non-linear problems ensures fast convergence of the Newton-Raphson method (from 3 up to 10 iterations) and makes it possible to reflect the history of loading.

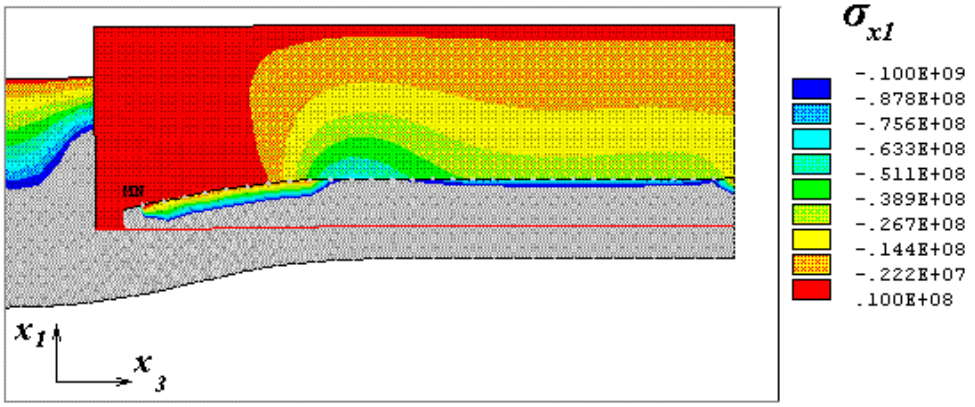

Figure 2. Distribution of radial stresses.

When one considers the contact autofrettage of the cylinders with the use of auxiliary bandages, one of the principal problems is to find the most appropriate values for the initial gap and the geometric parameters of the bandage. If the value of the initial gap meets the condition $\delta > 0.002$ m and the cylinder has a smaller thickness ($h = 0.032$ m) dangerous residual plastic deformations – up to 10% – can develop. In this case the bandage does not keep the strains under a reasonable limit. If the initial gap is too small ($\delta < 0.0007$ m), the residual plastic deformations in the cylinder prevent the full unloading in the bandage, therefore a residual pressure develops between the bandage and cylinder. Then the bandage cannot be removed from the cylinder. Moreover, the magnitude of the initial gap should ensure the release of the surfaces of the cylinder and bandage after unloading taking the residual gap β into consideration. Increasing the exterior radius of the bandage up to $R_{b2} = 0.192$ m, it is possible to significantly redistribute the stresses acting on the contact surfaces and to achieve a more uniform distribution of the residual radial displacements on the same surfaces after unloading. However, numerical experiments have shown that a big increase in the bandage thickness $h > 0.1$ m is ineffective. A repeated variation

of the geometric parameters resulted in the values: $\delta = 0.001$ m, $R_{b1} = 0.093$ m, $R_{b2} = 0.16$ m, which seem to be the best for an appropriate autofrettage.

The computational results we are going to present have all been obtained by the use of the above mentioned best parameters.

In the interactive regime of the computations of an autofrettage, seven loading conditions of the construction from the initial pressure $D = 500$ MPa up to a maximum value $D = 950$ Mpa are fixed.

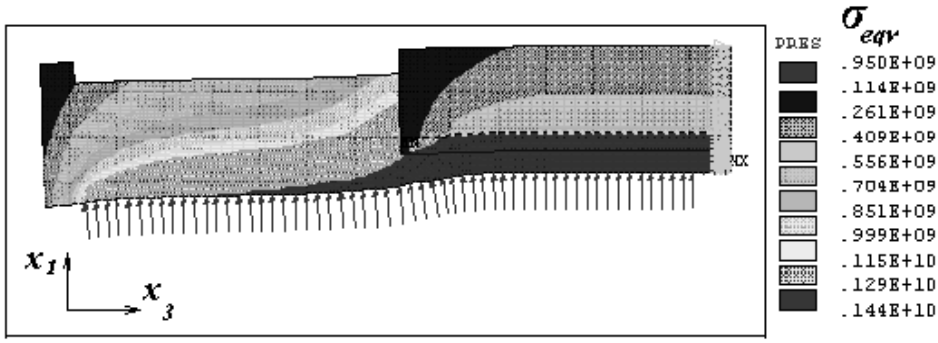

Figure 3. Distribution of equivalent stresses under of $P=950$ MPa

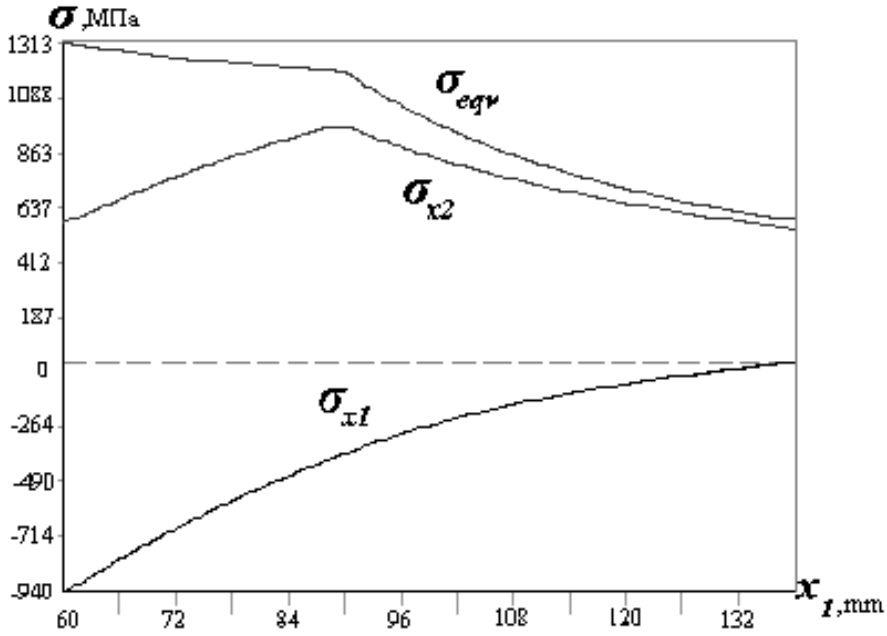

Figure 4. Distribution of stresses in the 1-st radial cut

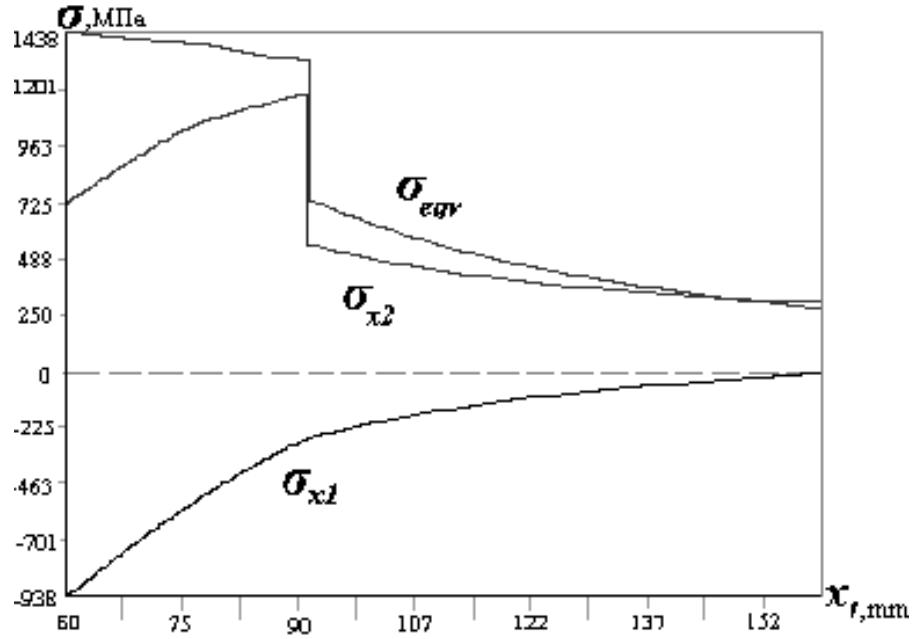

Figure 5. Distribution of stresses in the 2-nd radial cut

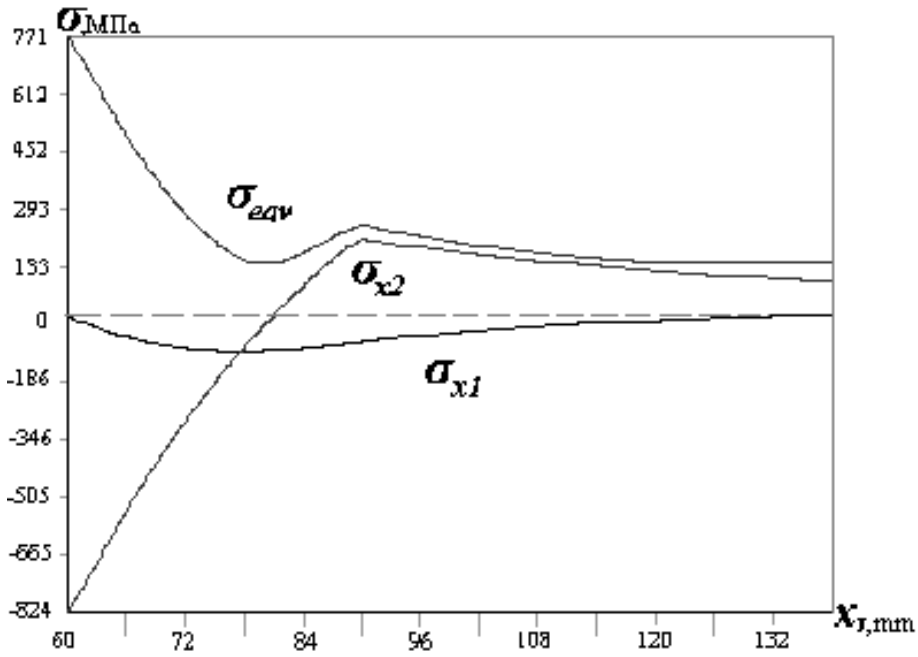

Figure 6. Distribution of residual stresses in the 1-st cut under P = 0.

Under the initial load the zones of plastic deformation in the second part of the cylinder are small and the surfaces of the cylinder and bandage do not contact yet. Contact zones appear if the load reaches the value $P = 650$ MPa.

For P= 700 MPa, Figure 2 shows the zone of contact interaction. The final distribution of the Mises equivalent stresses when the construction is subjected to the maximum load P= 950 MPa is represented in Figure 3. It is seen from those level lines of stresses which reached the yield stress of the material $\sigma_y = 1200$ MPa that the second part of the cylinder is in a plastic condition, while in the first one it is less than 600 MPa. As the character of the stress distributions in the two parts they are significantly different and for this reason it is expedient to investigate the regularities of the stress distributions along the thickness in the cross-sections: 1) $x_3 = 0.15$ m; 2) $x_3 = 0.4$ m.

Figure 4 shows the distributions of the equivalent σ_{eqv}, circular σ_{X2} and radial σ_{X1} stresses due to the maximum load $P = 950$ MPa for the first cross-section. The same stresses are given in the second cross-section, which passes through the cylinder and the bandage (Figure 5). If the circular stresses are discontinuous on the common boundary of the bodies, the radial stresses are continuous.

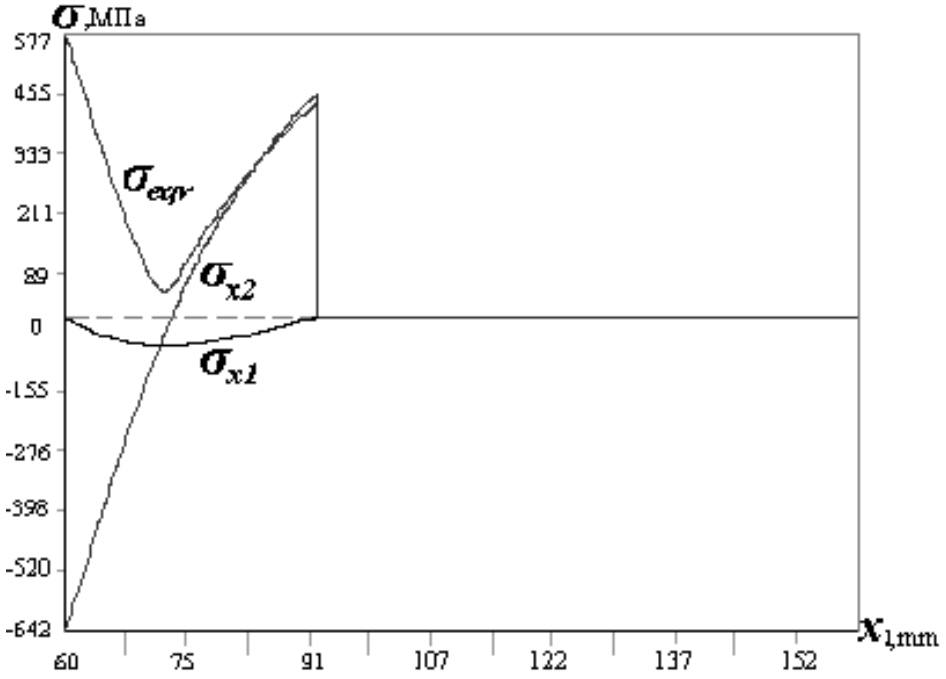

Figure 7. Distribution of the residual stresses in the 2-nd cut under P= 0.

In the last step the load was completely removed. Figure 6 shows the distribution of the residual stresses in the first cross-section. The circular stress reaches its maximum

$|\sigma_{X2}| = 824.5$ MPa on the interior surface of the cylinder. As regards the second cross-section (Figure 7), the stress distributions essentially differ and the circular stress on the interior surface has a sizeable magnitude $\sigma_{X2} =$ - 642 MPa. The distribution of the equivalent residual stresses is shown for the whole structure in Figure 8. The bandage is completely unloaded and the residual radial displacements on the exterior contact surface of the pipe in the second cross-section are less than the initial gap: $U_{X1} =$ 0.938 mm. Then the actual gap after unloading is $\delta = 0.062$ mm, which exceeds the supposed value β, therefore the bandage can be removed from the cylinder.

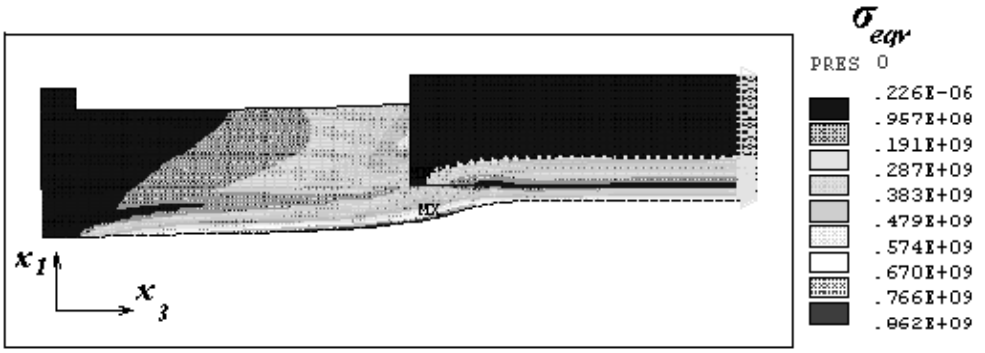

Figure 8. Distribution of equivalent residual stresses.

4. **Conclusions**

The results of the study allow us to project of autofrettage processes for real elements of constructions which have a complex shape. On the basis of these results the parameters can be calculated for loading and technology tools which do not admit of failure of construction. The procedure we have presented allows us to determine rational parameters for the contact autofrettage under which highly uniform fields of residual stresses on the interior surface of the cylinder are achieved.

References

1. Birger, I. A.: *Residual Stresses*, M., 1963, p. 230.
2. Perl, M. and Aroné, R.: *Stress intensity factors for a radially multicracked partially-auto-frettaged pressurized thick-walled cylinder*, Trans. of the ASME, J. of Pressure Vessel Technology, **110**, (1988), 147 - 154.
3. Schindler, H. J.: *Determination and evaluation of residual stresses in thick-walled cylinders due to auto-frettage*, Proc. of the 6th Int. Conf. on Residual Stresses, Oxford, U.K., July 10-12, 2000, Vol. 2, 837-844.
4. Baltov, A. and Sawczuk A.: *A rule of anisotropic hardening*, Acta Mechanica, **1**, (1965), 81-92.

5. Kadashevich, U. I. and Novozhilov, V. V.: *A theory of plasticity which takes residual microstresses into account*, Applied Mathematics and Mechanics, **22**(1), (1958), 78-89. (in Russian).

6. Duvaut, G. and Lions, J. L.: *Inequalities in mechanics and physics*, Dunod, Paris, 1972. (in French).

7. Lvov G. I.: *Variational formulation of a contact problem for linearly elastic and physically non-linear slanting shells*, Applied Mathematics and Mechanics, **46**(5), (1982), 841-846. (in Russian).

Journal of Computational and Applied Mechanics, Vol. 3., No. 1., (2002), pp. 61–84

EXAMINATION OF CONTACT OPTIMIZATION AND WEARING PROBLEMS

István Páczelt and Attila Baksa
Department of Mechanics, University of Miskolc
3515 Miskolc-Egyetemváros, Hungary
mechpacz@uni-miskolc.hu and mechab@uni-miskolc.hu

[Received: April 22, 2002]

Dedicated to Professor Gyula Béda on the occasion of his seventieth birthday

Abstract. A system of elastic bodies is examined. It is assumed that the displacements and deformations are small. Firstly, the minimum of maximum pressure and other mechanical values (torque, frictional power loss) are sought by controlling the distribution of contact pressure. Secondly, the optimization problem for roller bearings in rolling state will be discussed and the optimization problem for the wearing process will be formulated as well. For the solution of the optimization problems special iterational algorithms have been developed. In order to solve the contact problem we use both the total potential energy with augmented Lagrangian technique and the modified complementary energy. The p-version of the finite element method is applied for the first problem type, while in the second case an iterational algorithm is developed which includes Kalker's *KOMBI* program. Numerical examples demonstrate the efficiency of the proposed iterational procedure.

Mathematical Subject Classification: 74M15, 74P99, 74S05
Keywords: contact problems, optimization, p-version FEM, wearing process

1. Introduction

The stress state of machine parts is strongly influenced by their geometrical shapes and forms. The optimum design of elements of different bearings, machine tool guides, bars, etc., needs special considerations to avoid singularities and to improve the strength endurance. In optimization problems the design parameters are usually concerned with material parameters, shape, characteristic dimensions, supports, loads, inner links, reinforcement and topology (see Mróz [1]). In engineering practice, connections between machine elements are frequently modelled as unilateral contact problems. Comparatively few studies can be found in the literature for contact optimization [2], [3]. The thorough mathematical investigation of the subject can be found in [4]. The controlling technique of contact pressure distribution is employed for the shape optimization problem of cylindrical bodies using h- and p-version of the finite element method without friction in [5], [6] and with friction in [7]. Work [8] gives a contribution to the solution for practical problems by controlling the contact

pressure distribution when one of the bodies has rigid body translation and rotation. The question of round off is examined in [9] for roller bearings without friction.

Contact pressure optimization is studied for the problem of an elastic punch and a rigid target within the framework of linear elasticity in [10]-[13]. In many earlier works [14]-[16] the maximum contact pressure was chosen to be the objective function, but it was not differentiable. Articles [10], [11], [13] and [17] use the total potential energy as a cost function and the integral of the gap function as the ISO-parametric constraint.

Approximately constant contact pressure distribution has been achieved in [15], [16] by appropriate shape optimization for axially symmetric bodies, assuming that the change in radius has no effect on the stiffness and compliance matrices.

Discretization of the domain with p-version finite elements is advantageous [18], since it results in fast convergence, and high order mapping assures accurate geometry for shape optimization.

Five types of mechanical contact problems will be examined:

1. Minimization of the maximum of contact pressure.
2. Maximization of rigid body displacement.
3. Maximization of torque or the contact resultant force between the bodies.
4. Minimization of frictional power loss (wearing values) between machine elements.
5. Optimization of roller shape by controlling the contact pressure distribution.

In case 5 the effect of frictional stress, which arises during the rolling motion, is taken into account. In cases 2, 3 and 5 the Mises equivalent stress is kept under a prescribed limit in addition to the control of contact pressure.

In the optimization of roller shape, the influence matrix is derived from the solution of the elastic half-space problem [19], and the mirror technique is also applied in this program [9].

The p-version of the finite element method is used in the first four types of the optimization problems.

2. Contact conditions

The contact of two elastic bodies ($\alpha = 1, 2$) is examined here. It is assumed that the displacements and deformation are small. The body volumes V^α are bounded by surfaces S^α, which can be separated into S_p^α, S_u^α – on which the surface traction is $\widetilde{\mathbf{p}}$ and the displacement $\mathbf{u}_0$ is given – and into S_c^α on which there could be unilateral contact (see Figure 1). The Signorini type contact conditions are assumed in normal direction $\mathbf{n}_c$, where $\mathbf{n}_c = -\mathbf{n}^2 \widetilde{=} \mathbf{n}^1$.

The normal stress on the surface S_c^α is $\sigma_N^\alpha = \mathbf{n}^\alpha \cdot \boldsymbol{\sigma}^\alpha \cdot \mathbf{n}^\alpha$, where $\boldsymbol{\sigma}^\alpha$ is the stress tensor. After deformation the gap in the direction $\mathbf{n}_c$ is

$$d = u_N^2 - u_N^1 + h \tag{2.1}$$

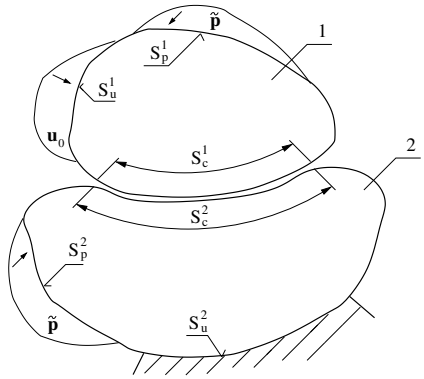

Figure 1. The contact between two bodies

where $u_N^\alpha = \mathbf{u}^\alpha \cdot \mathbf{n}_c$ and h is the initial gap – see Figure 2 for further details.

Let

$$p = -\sigma_N^1 = -\sigma_N^2 \tag{2.2}$$

be the contact pressure. It is clear that there is contact if the following conditions are fulfilled

$$d = 0\,, \qquad p \geq 0 \qquad \mathbf{x} \in \Omega_p\,, \tag{2.3a}$$

and there is separation if

$$d \geq 0\,, \qquad p = 0 \qquad \mathbf{x} \in \Omega_0\,, \tag{2.3b}$$

that is

$$p \cdot d = 0\,, \qquad \mathbf{x} \in S_c = \Omega = \Omega_p \cup \Omega_0\,. \tag{2.3c}$$

To calculate the effects of friction, the slip between the contacting bodies is also to

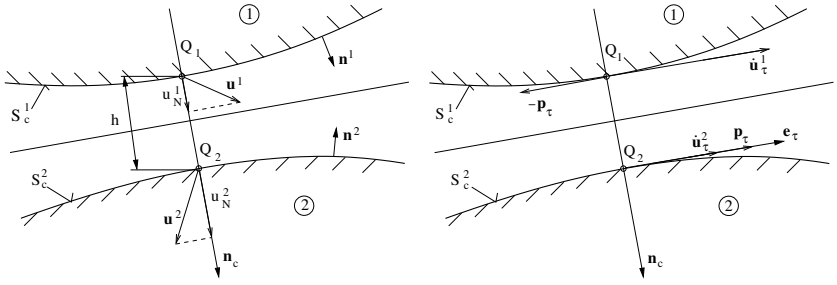

Figure 2. Contact and separation

be defined. The Coulomb dry friction model is employed henceforth. The relative slip in tangential direction is formulated as

$$\dot{\mathbf{u}}_\tau = \dot{\mathbf{u}}_\tau^1 - \dot{\mathbf{u}}_\tau^2\,, \tag{2.4}$$

where $\dot{\mathbf{u}}_\tau^\alpha$ is the tangential velocity in the body α. The adhesion zone of the contact region is characterized by the following conditions

$$\|\mathbf{p}_\tau\| \le \mu\, p\,, \qquad \dot{\mathbf{u}}_\tau = \mathbf{0}\,, \tag{2.5a}$$

where

$$\mathbf{p}_\tau = -\sigma^1 \cdot \mathbf{n}^1 - p\,\mathbf{n}_c = \sigma^2 \cdot \mathbf{n}_c - p\,\mathbf{n}_c \equiv \mathbf{p} - p\,\mathbf{n}_c\,. \tag{2.5b}$$

In the slip domain the traction in tangential direction is given as

$$\mathbf{p}_\tau = \mu\, p \frac{\dot{\mathbf{u}}_\tau}{\|\dot{\mathbf{u}}_\tau\|}\,, \tag{2.5c}$$

where $\mathbf{p}_\tau$ is calculated for the lower body, namely the second body in our case.

The boundary value problem is solved by making use of variational principles [20] by which we mean the modified complementary energy and potential energy with augmented Lagrangian technique [8], [24].

3. **Optimization problems**

3.1. **Control of the contact pressure.** The expected aim is achieved by changing the shape of the proposed zone of contact domain in the types of contact optimization tasks considered. Some works can be found in the references where the shape of the contacting bodies is changed on the surfaces which are out of the contact zone, such as [21], [22] and [23].

In our optimization problems it is assumed that the bodies are in contact in the whole sub-domain Ω_c of the contact zone $S_c = \Omega$, where Ω_c is called the control sub-domain. The contact surface is modified so that the following function holds true for the contact pressure

$$p(\mathbf{x}) = v(\mathbf{x})\, p_{\max}\,, \qquad \mathbf{x} \in \Omega_c\,, \tag{3.1}$$

where the control function we have chosen must satisfy the condition $0 \le v(\mathbf{x}) \le 1$, and

$$p_{\max} = \max\, p(\mathbf{x})\,, \qquad \mathbf{x} = [s,t]\,, \tag{3.2}$$

where s and t are surface co-ordinates in the region Ω. In the sub-domain Ω_{nc} ($\Omega =$

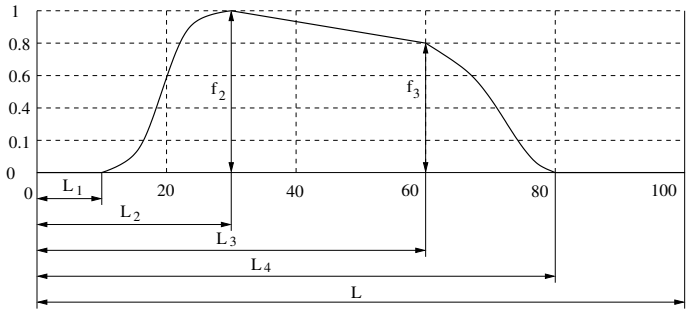

Figure 3. $V(s)$ function

$\Omega_c \cup \Omega_{nc}$), where the pressure is not controlled, the fulfillment of the following inequality is required

$$\chi(\mathbf{x}) = v(\mathbf{x})p_{\max} - p(\mathbf{x}) \geq 0, \qquad \mathbf{x} \in \Omega_{nc}. \tag{3.3}$$

Let us define a function $V(s)$ of class C^1 in the sub-region Ω_c (see Figure 3)

$$V^* = V^*(s) = f_2 + (f_3 - f_2)\frac{s - L_2}{L_3 - L_2} \tag{3.4}$$

$$V(s) = 0\,, \qquad 0 \leq s \leq L_1$$

$$V(s) = V^* \left\{ 3 \left[\frac{s - L_1}{L_2 - L_1} \right]^2 - 2 \left[\frac{s - L_1}{L_2 - L_1} \right]^3 \right\}, \qquad L_1 \leq s \leq L_2$$

$$V(s) = V^*, \qquad L_2 \leq s \leq L_3$$

$$V(s) = V^* \left\{ 1 - 3 \left[\frac{s - L_3}{L_4 - L_3} \right]^2 + 2 \left[\frac{s - L_3}{L_4 - L_3} \right]^3 \right\}, \qquad L_3 \leq s \leq L_4$$

$$V(s) = 0\,, \qquad L_4 \leq s \leq L,$$

where parameters $f_2, f_3, L_j, j = 1, \ldots, 4$ are fixed or some of these are calculated in the optimization process. In this case $\frac{dV}{ds} = 0$ at $s = L_1, s = L_4$, and also if $f_2 = f_3 = 1$ at points $s = L_2, s = L_3$.

For two dimensional contact problems $v(s) = V(s)$ in Ω. For three- dimensional problems it is assumed that the upper body has a translation and a rigid body rotation, Ω_c is a line s, and the rotation vector is perpendicular to this line. The control function along the curve s has the following form

$$v(s) = V(s) \left[1 + B \left(\frac{s}{L} \right)^n \right], \tag{3.5}$$

and along direction t $\widetilde{v}(t) = 1$, that is

$$v(\mathbf{x}) = v(s)\widetilde{v}(t). \tag{3.6}$$

Value B is calculated from equilibrium equations for the first body, where $10 \leq n \leq 15$ [8].

3.2. **Contact optimization for axisymmetric bodies.**

3.2.1. *Solving the contact problems with iteration.* Firstly, the arising equivalent stress is not taken into account in most of the tasks investigated. The optimal shape is determined besides the prescribed parameters (L_i, $i = 1, \ldots, 4$).

The solution of the problem is found with the iterational method, introduced in [8]. This method is labelled as 1^{st} *type iteration.*

Secondly, the Mises equivalent stress σ_{eq} must be under a prescribed ultimate stress σ_U

$$\sigma_{eq} \leq \sigma_U. \tag{3.7}$$

When the optimization problem includes (3.7) as an additional condition, the solution requires another iteration, labelled as 2^{nd} *type iteration.* These problems are classified

into two main groups. The first one is when a kinetic or dynamic quantity is maximized (for example the displacement of the upper punch or the contact force between the bodies). The second one is when one of the control parameters (see Figure 3) is minimized or maximized.

The 2^{nd} *type iteration* is built up in the following way. The quantity searched for is f. During the iteration the value of f is changed. The iteration variable is istep, and the value of f is calculated by

$$f = f_0 \cdot \mathsf{istep}\,, \tag{3.8}$$

where f_0 is chosen in advance. The optimization problem is solved by the 1^{st} *type iteration* with the fixed f. In each istep a new shape is determined for the upper body.

The Mises equivalent stress σ_{eq} is calculated in the Gaussian integral points of the finite elements and in the border points as well: $(\xi = -1, \xi_1, \ldots, \xi_{NG}, 1)$, $(\eta = -1, \eta_1, \ldots, \eta_{NG}, 1)$, where ξ, η are the local normal co-ordinates, and NG is the number of integration points along the direction ξ or η. When $\sigma_{eq} > \sigma_U$ in any control points, then $f = f^{**}$ and in the previous step $f = f^*$. The optimal f^{opt} is searched for in the interval $f^* < f^{opt} < f^{**}$ by the following linearization process:

$$f^{opt^{(i)}} = f^* + (f^{**^{(i)}} - f^*) \cdot \frac{\sigma_U - \sigma^*_{eq}}{\sigma^{**^{(i)}}_{eq} - \sigma^*_{eq}} \qquad i = 1, 2, \ldots \tag{3.9}$$

where $f^{**^{(1)}} = f^{**}$, $\sigma^{**^{(1)}}_{eq} = \sigma^{**}_{eq}$, σ^*_{eq} is the maximum value of the Mises equivalent stress calculated by f^* similarly to the value of σ^{**}_{eq}. The iterational process will run until

$$\frac{\left|\sigma_U - \sigma^{**^{(i)}}_{eq}\right|}{\sigma_U} \leq 0.015. \tag{3.10}$$

3.2.2. *Optimization problems examined.* In the present examination axisymmetric bodies (see Figure 4) are discretized by p-extension elements [18].

The following problems have been analyzed:

P1: The vertical displacement w_0 is prescribed on the top surface of the punch. Using the control function with given parameters L_j, $(j = 1, \ldots, 4)$, the shape optimization is performed on the punch keeping its unloaded original length that is fixed in axial direction. Introducing a new variable $s = R - R_b$, and Δh for the gap function, the optimization problem [8] is formulated as

$$\min\Big\{p_{\max}\,\Big|\, p \geq 0,\ d = d(p, \Delta h) = 0\,, \quad \chi = v(s)\, p_{\max} - p(s) = 0,\ \min \Delta h = 0\Big\}. \tag{3.11}$$

The problem is solved by the 1^{st} *type iteration.*

P2: This is the problem where the additional constraint (3.7) is to be satisfied during the optimization process. So the value of displacement w_0 on the top surface

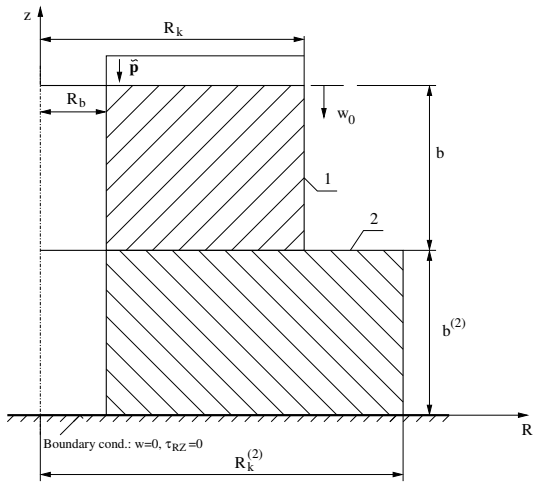

Figure 4. Punch problem of axially symmetric bodies

of the upper body must be maximized, thus the problem to be solved can be described as follows

$$\max\Big\{w_0\ \Big|\ \min\big\{p_{\max}\,\big|\,p\geq 0,\ d=d(p,\Delta h)=0\,,\ \chi=0,\ \min\Delta h=0\big\},\sigma_{eq}\leq\sigma_U\Big\}. \tag{3.12}$$

in which the inner optimization problem is calculated by the 1^{st} *type iteration*, while the 2^{nd} *type iteration* is used for solving the outer task. In equation (3.9) the quantity searched for is $f = w_0$.

P3: Applying the given displacement w_0 and the control function of problem P1, shape optimization is performed on the punch resulting in a given value of compressing force F_p [8].

$$\min\Big\{p_{\max}\,\Big|\,p\geq 0,\ d=d(p,\Delta h)=0,\ \chi=0,\ F_p=2\pi\int_{R_b}^{R_k}R\,p\,dR\Big\}. \tag{3.13}$$

P4: When the constraint of the Mises equivalent stress is kept, the value of F_p cannot be chosen at will, its maximum value will be presented as an additional unknown variable. The problem to be solved is therefore the following

$$\max\Big\{F_p\ \Big|\ \min\big\{p_{\max}\,\big|\,p\geq 0,\ d=d(p,\Delta h)=0,\ \chi=0\big\},\ \sigma_{eq}\leq\sigma_U\Big\}. \tag{3.14}$$

Figure 5 shows an example for this problem, with the following material properties: Young modulus: $E = 2{\cdot}10^5\,MPa$, Poisson ratio: $\nu = 0.3$ and geometrical data $R_b = 20\,mm$, $R_k = 120\,mm$, $R_k^{(2)} = 140\,mm$, $b = b^{(2)} = 50\,mm$. The parameters of the control function in (3.4) are $L_1 = 0\,mm$, $L_2 = 4\,mm$, $L_3 =$

$96\,mm$, $L_4 = 100\,mm$. The prescribed displacement on the top surface of the upper body is $w_0 = 0.1\,mm$. Let the value of f_0 in equation (3.8) be

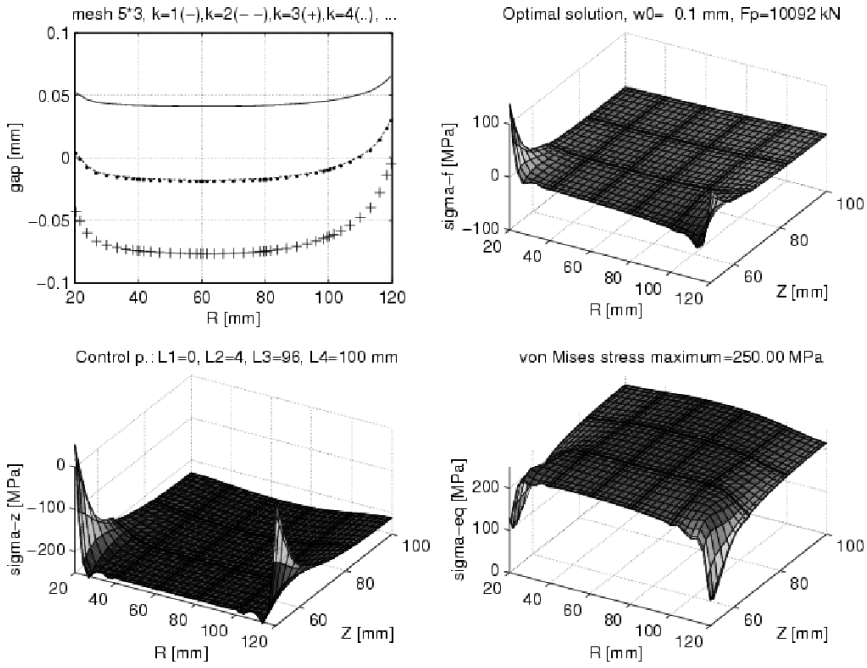

Figure 5. Gap and stress distribution for Problem P4

$f_0 = F_0 = 5000\,kN$ fir which the contact force is $F_p = F_0 \cdot \mathsf{istep}$ in the 2^{nd} *type iteration*. In Figure 5 the upper left picture illustrates the gap during the iterations ($k = \mathsf{istep}$). $\sigma_{eq} < \sigma_U$ in the first two iterations ($k = 1, 2$), but for $k > 2$ then σ_{eq} is significantly more than σ_U. In this example the number of iterations in (3.9) is two. The result shows that the height of the upper part must be extended, i.e., the initial gap between the bodies is a negative value in the interval $20 \le R \le 110$. The maximum of the compressing force F_p is also calculated and is equal to $= 10092\,kN$.

P5: The punch is loaded by a constant pressure $\widetilde{p}$ on its top surface. The resultant is $F_0 = \pi(R_k^2 - R_b^2)\widetilde{p}$. The torque M_T should be maximized

$$\frac{M_T}{\mu} = \int_{R_b}^{R_k} 2\pi R^2\, dR\,, \tag{3.15}$$

where μ is the coefficient of friction. It is evident that the maximum torque is achieved when only the outer corner of the punch ($R = R_k$) is in contact, and the minimum value is observed if any of the inner corners of the punch ($R = R_b$) is in contact. In order to have a smooth stress distribution the shape of

the punch is determined using a control function given in terms of the parameters $(L_2 - L_1), L_3$ where the latter has a fixed value and L_4 is also fixed. The control of the discretization of contact pressure is calculated from the following equation:

$$\begin{aligned}\chi = \chi(s, p, L_1) =& v(s, L_1, L_2(L_1), L_3 \text{ and } L_4 \text{ are fixed})\, p_{\max} \\ & - p(s, L_1) = v(s, L_1)\, p_{\max} - p(s, L_1) = 0\,,\end{aligned} \tag{3.16}$$

that is

$$p(s, L_1) = v(s, L_1)\, p_{\max}\,. \tag{3.17}$$

The equilibrium equation for the upper body is

$$F = F(L_1, p_{\max} \text{ is fixed}) = F_0 - 2\pi \int_{R_b}^{R_k} R\, v(R - R_b, L_1)\, p_{\max}\, dR = 0\,. \tag{3.18}$$

The value of L_1 can be determined from equation (3.18) because the maximum value of the contact pressure $p_{\max}$ is prescribed.

The optimization problem is formulated as follows

$$\begin{aligned}\max \Big\{ \frac{M_T}{\mu} \,\Big|\, & p = p(s, L_1) \geq 0,\ d = d(p, \Delta h) = 0\,, \\ & \chi = \chi(s, p, L_1) = 0,\ F = F(L_1, p_{\max} \text{ is fixed}),\ \min \Delta h = 0 \Big\},\end{aligned} \tag{3.19}$$

where parameters L_1, Δh, p are unknown [8].

P6: When the additional stress condition (3.7) is kept, the value of $p_{\max}$ cannot be fixed in advance. The solution should be searched for by maximizing length L_1, and the problem to be solved is formulated as follows

$$\begin{aligned}\max_{L_1} \Big\{ \frac{M_T}{\mu} \,\Big|\, & p = p(s, p_{\max}(L_1)) \geq 0,\ d = d(p, \Delta h) = 0, \chi = \chi(s, p, L_1) = 0\,, \\ & F = F(p_{\max}(L_1)) = 0,\ \min \Delta h = 0,\ , \sigma_{eq} \leq \sigma_U \Big\}.\end{aligned} \tag{3.20}$$

During the optimization process the distance L_1 is changed by $\Delta L_1 = \frac{L_3 - L_1}{10} = \frac{96-4}{10}$, where L_3, L_4 are the control parameters in the initial state, i.e. (istep $= 1$). The optimal length is L_1^{opt}, which is computed in the $L_1^* < L_1^{opt} < L_1^{**}$ interval using the iteration with linear approximation according to (3.9).

Figure 6 shows the results of a numerical example and Figure 7 shows the shape of the punch during the iteration. The load of the upper body is $\widetilde{p} = 100\, MPa$. After the solution of the optimization problem the results are the following, $L_1^{\text{opt}} = 19.42\, mm$, $L_2 = L_1^{\text{opt}} + 4$, $\frac{M_T}{\mu} = 377.68 \cdot 10^6\, Nmm$. Figure 6 shows the solution for the original construction, i.e., when there is no initial gap between the contacting bodies. The number of iterations istep varies from 0 to 6. If (istep $= 1$), the control parameters are $L_1 = 0\, mm$, $L_2 = 4\, mm$, $L_3 = 96\, mm$, $L_4 = 100\, mm$.

Since the elements around the point with co-ordinates $R = R_k$, $z = b^{(2)}$ in the lower body are not small, the solution cannot give as a high value for σ_{eq} in istep $= 0$ as is expected. Theoretically this point shows singularity with respect

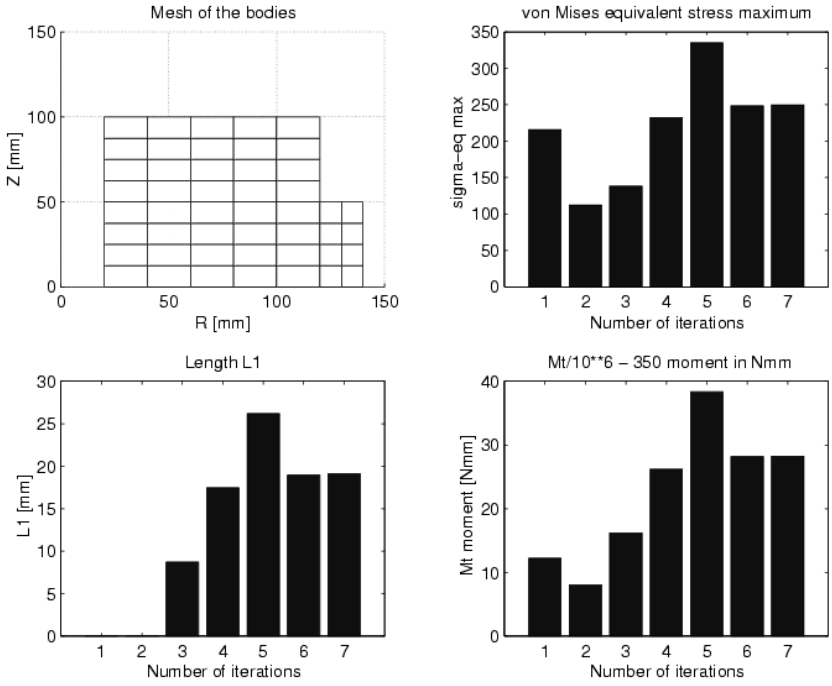

Figure 6. Results of optimization problem P6 (Number of iterations $=$ istep $+ 1$)

to the stress state. In our investigation the control of the contact pressure gives the stress state without any singularity, so large elements are applicable.

Choosing different loads $\widetilde{p}$ the results are shown in Table 1. It is observed that the pressure $\widetilde{p}$ is changing linearly however the torque is not increased in that way. The 2^{nd} *type iteration* is controlled by keeping the inequality (3.10).

$\widetilde{\mathbf{p}}\ [MPa]$	$\mathbf{L_1}\ [mm]$	$\frac{\mathbf{M_T}}{\mu} \cdot 10^{-6}\ [Nmm]$	$\mathbf{p}_{\max}\ [MPa]$	$\max \sigma_{\mathbf{eq}}\ [MPa]$
40	48.932	169.646	62.968	249.98
60	33.454	238.869	77.468	252.69
80	24.569	307.771	95.210	248.12
100	19.418	377.677	114.480	249.35

Table 1. Results for problem P6 with different loads

P7: The relative angular velocity ω of the punch is given. The shape of the contact surface is optimized in order to minimize the frictional power loss by applying the control function with parameters $L_1 = 0\,mm$, L_2 is a fixed value and $L_4 - L_3$ are

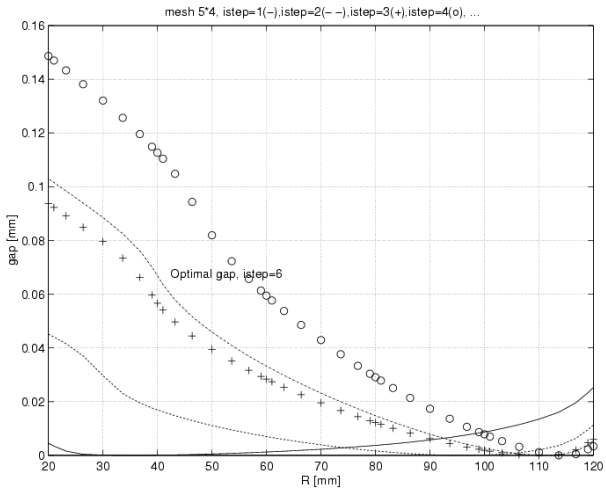

Figure 7. Gaps during the optimization problem P6

given values. The power loss is written as

$$D = \int_{R_b}^{R_k} 2\pi R\,\omega\,\mu\,R\,dR = M_T\,\omega\,. \tag{3.21}$$

The closer the location of the resultant of the contact pressure to radius R_b the smaller the frictional power loss, so the optimization problem [8] is expressed as

$$\min\Big\{\frac{D}{\mu\,\omega}\,\Big|\,p = p(s,L_4) \geq 0,\; d = d(p,\Delta h) = 0,\; F = F(L_4, p_{\max}\,\mathsf{is\ fixed}) = 0\,,$$
$$\chi = v(s,L_1,L_2\,\mathsf{is\ fixed}, L_3(L_4), L_4)\,p_{\max} - p(s,L_4) = 0,\; \min\Delta h = 0\Big\}\,, \tag{3.22}$$

where parameters L_4, Δh and p are unknown if $p_{\max}$ is given.

P8: In this case the additional condition (3.7) is valid, and the length L_4 is minimized during the process of optimization.

$$\min_{L_4}\Big\{\frac{D}{\mu\,\omega}\,\Big|\,p = p(s,p_{\max}(L_4)) \geq 0,\; d = d(p,\Delta h) = 0,\; \chi = \chi(s,p,L_4) = 0\,,$$
$$F = F(p_{\max}(L_4)) = 0,\; \min\Delta h = 0,\; ,\sigma_{eq} \geq \sigma_U\Big\}. \tag{3.23}$$

The train of thought in this iteration is the same as for problem P6. The results are shown in Figure 8. Stress distribution is illustrated in Figure 9. The applied load is $\widetilde{p} = 100\,MPa$ and the results are the following: optimized length is $L_4 = 93,90\,mm$, $L_1 = L_2 = 0\,mm$, $L_3 = L_4 - 4$ and $\frac{D}{\mu\omega} = 337.09 \cdot 10^6\,Nmm$.

During the calculations the initially uniform finite element mesh is modified automatically by the program. To ensure the oscillation-proof results for stress

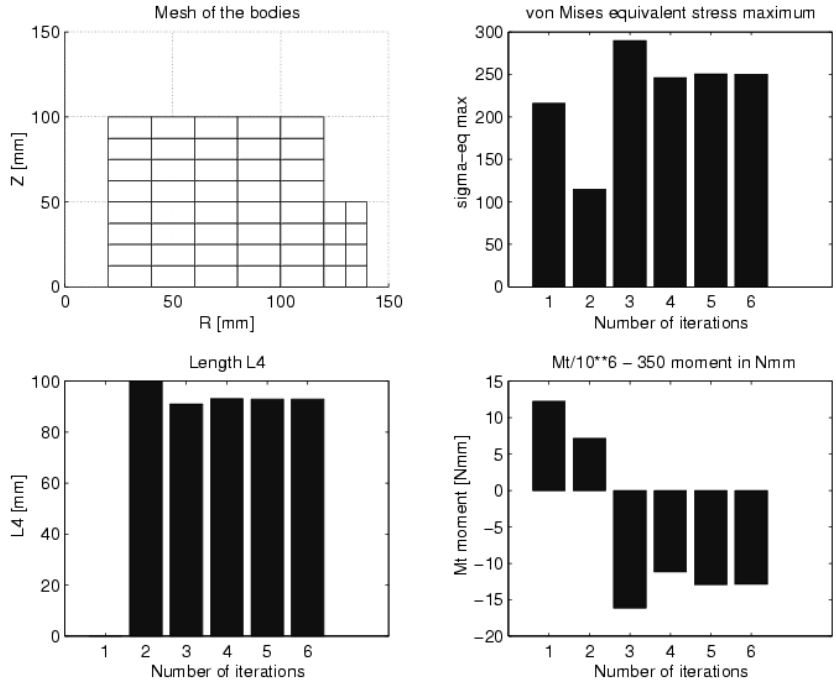

Figure 8. Results of optimization problem P8

distribution intervals $L_3 \leq s \leq L_4$ and $L_4 \leq s \leq L$ are divided into small elements. The contact zone is monitored from the right border point of the second finite element starting at the outer radius of the upper body.

$\widetilde{\mathbf{p}}\ [MPa]$	$\mathbf{L_4}\ [mm]$	$\frac{\mathbf{D}}{\mu\omega} \cdot 10^{-6}\ [Nmm]$	$\mathbf{p}_{\max}\ [MPa]$	$\max \sigma_{\mathbf{eq}}\ [MPa]$
40	78.15	116.839	63.29	249.18
60	86.81	190.064	79.34	247.47
80	91.27	263.595	97.06	247.64
100	93.90	337.091	115.45	250.46

Table 2. Results for problem P8 with different loads

For different loads $\widetilde{p}$ the results are shown in Table 2. The initial control parameters for optimization are $L_1 = L_2 = 0\,mm$, $L_3 = 96\,mm$, $L_4 = 100\,mm$.

P9: In the wearing process the wearing velocity has the following form

$$\dot{w} = c(\mu\, p)^a ||\dot{\mathbf{u}}_\tau||^b, \qquad \mathbf{x} \in S_c\,, \tag{3.24}$$

where a, b, c are parameters resulting from experiment [25] and $\dot{\mathbf{u}}_\tau$ stores the relative velocity in the tangential direction. The rate of wear is calculated by

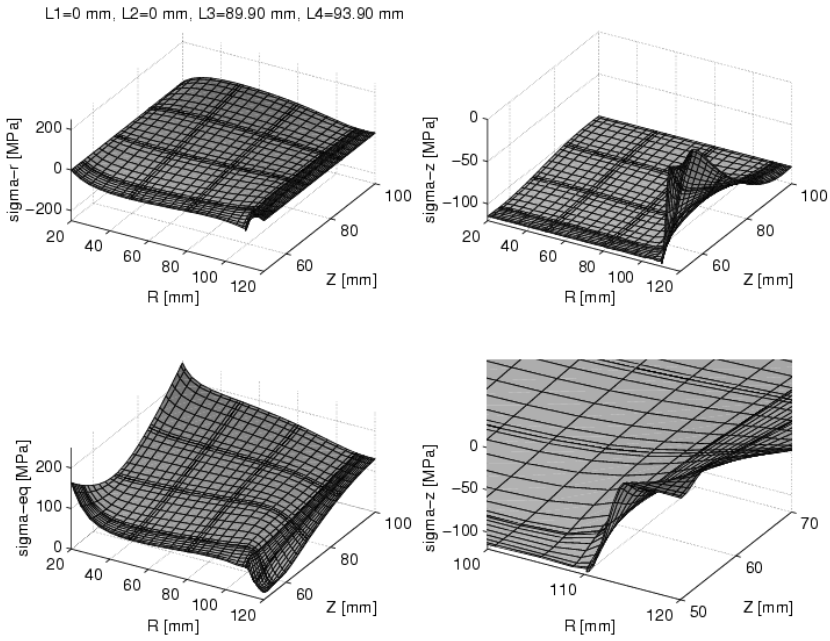

Figure 9. Stress distribution of optimization problem P8

the following formula

$$\dot{W} = \int_{S_c} \dot{w}\, dS\,. \tag{3.25}$$

If $||\dot{\mathbf{u}}_\tau|| = R\,\omega$ and $a = b = 1$, then

$$\dot{W} = \frac{D}{c} \tag{3.26}$$

that is, the minimization problem for $\dot{W}$ is equivalent to formula (3.23). In another case a strongly nonlinear optimization problem is obtained because the objective function is nonlinear as well.

3.3. **Optimal shape design of rollers.** Rolling elements can be found in a number of engineering equipment. Their long overall lifetime requires keeping stresses at a low and smooth value.

A number of papers [9], [25]-[28] are devoted to the issue of roller rounding-off. In these papers, except for the last one, the radius of rounding-off is given, which results in a generally non-smooth contact pressure distribution.

In paper [8] the optimum shape of a roller bearing is determined by the control function according to formulae (3.3)-(3.5), in which $f_2 = f_3 = 1$. The roller has a

translation and rigid body rotation. In the optimization process the rolling state of the roller has not been taken into account, that is, there is no friction.

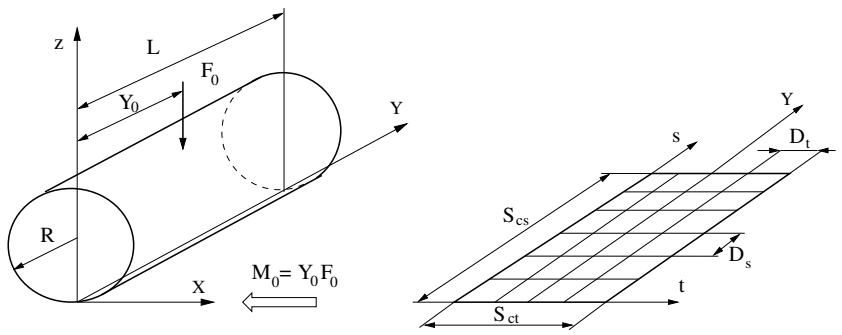

Figure 10. Roller load and geometrical properties

A roller is loaded by the force F_0, which can be replaced by an equivalent force couple system F_0 and M_0 on the axis x. The geometry and the load of a roller can be found in Figure 10. The elastic half-space model is applied to produce the influence function for the roller, taking the mirror technique [9] into account. $Z = 0$ on the surface of the half-space and the rectangular contact region $(S_{ct} \times S_{cs})$ is divided into small rectangles $(D_t \times D_s)$.

Elements of the influence matrix are computed by applying a unit normal load or a unit tangential load in the direction X in the sub-region $D_t \times D_s$. The formulae can be found in Kalker's book [19]. In order to eliminate shearing stresses at the ends of the roller, the mirror technique is taken into account.

The present work enhances the previous results in two ways.

1. Firstly, if the load is not applied along the center of the roller, that is $Y_0 < \frac{S_{cs}}{2}$, an algorithm should be applied, which is based on the following formula
$$M_* = Y_0 \int_\Omega p\, dS - \int_\Omega Y p\, dS\,, \tag{3.27}$$
which should be minimized to zero.
   In this case there are two possibilities.
   - The first is to search for the end of the control function, that is $s = L_4$, when $f_2 = f_3 = 1$ and the value of B is practically zero. The result is that the contact pressure is carried by the $0 \le s \le L_4$ interval of the roller.
   - The second is to ensure contact along the roller's full length. In this case the problem is to search for the value $f_3 < 1$, while $f_2 = 1$.
2. Secondly, the tangential components of stress are taken into account while optimizing the shape of the roller, when the roller is loaded in its center. The pressure distribution is controlled by parameters L_j, $j = 1, \ldots, 4$ during optimization, using the control functions defined under (3.4).

To solve the rolling problem Kalker's program [30] is used, which is written in FORTRAN. The calculations use the KOMBI subroutine of Kalker's program, which gives a prescribed F_0 load, and a prescribed displacement in direction X. The theoretical background of the program can be found in work [19].

3.3.1. *Examples for non-centrally loaded rollers.* The radius of the roller is $R_0 = 60\,mm$. The roller is subjected to loads of $F_0 = 5000\,N$ and $M_0 = 33000\,Nmm$; $Y_0 = 13.2\,mm$. The material properties are as follows: Young modulus: $E = 1.97{\cdot}10^5\,MPa$, Poisson ratio: $\mu = 0.28$.

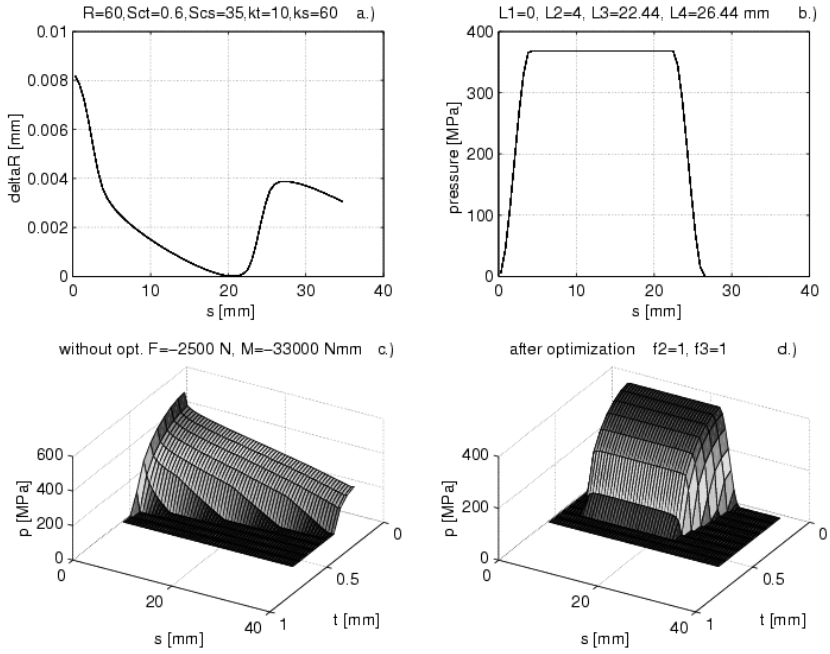

Figure 11. Optimized shape and pressure distribution in the 2^{nd} solution

The proposed contact region is divided into $10 \cdot 60$ rectangular elements, $L_1 = 0\,mm$, $L_2 = 4\,mm$, $L_4 - L_3 = 4\,mm$. In this case $n = 12$ (see formula (3.5))

- *First solution:* The problem can be solved by making use of an algorithm published in [8]. At the end of the calculations $M_* = -77.7\,Nm$, $B = -0.999$, $L_4 = 26.86\,mm$ and $p_{\max} = 369.1\,MPa$.
- *Second solution:* For the first case the value of $L_4$is determined by positive pressure. However, for the the second case L_4 is determined by the minimization of the moment M_*. The algorithm developed gave the following results: $M_* = -6.65\,Nm$, $B = -0.68 \cdot 10^{-3}$, $L_4 = 26.44\,mm$ and $p_{\max} = 368.9\,MPa$.

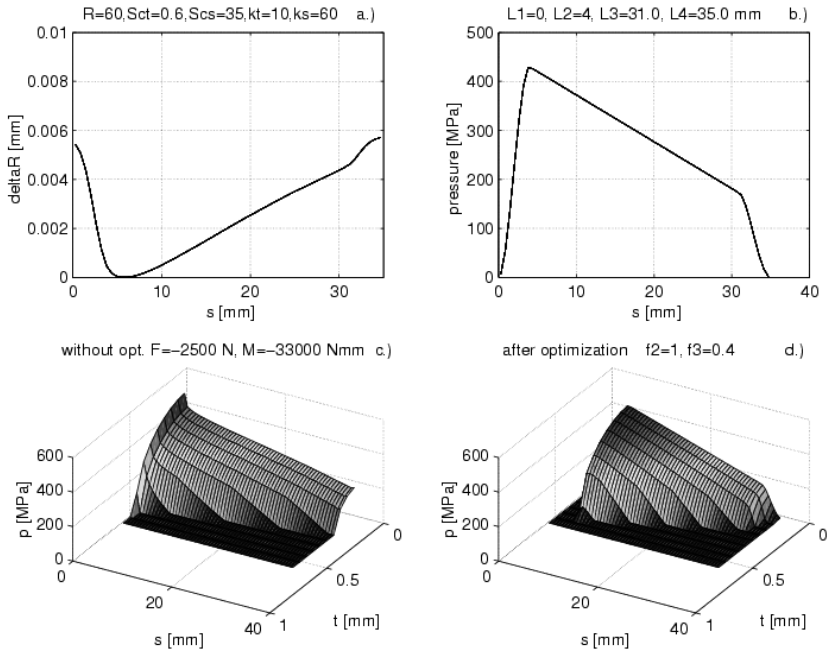

Figure 12. Optimized shape and pressure distribution in the 3^{rd} solution

Figure 11 shows the initial gap, the pressure distribution in the central longitudinal section of the roller, and the pressure over the whole domain before and after optimization.

- *Third solution:* The value of moment M_* is minimized by changing the parameter f_3, while equation $L_4 = S_{cs}$ is kept. Results of the calculation are $M_* = 47.58\,Nm$, $B = 0.39 \cdot 10^{-3}$ and $p_{\max} = 425\,MPa$. Figure 12 shows the initial gap and the stress-state for this optimization prioblem.

  Comparing these results, it can be realized that the second solution is the best according to the objective function ($\min p_{\max}$).

3.3.2. *Optimization of centrally loaded rollers when rolling.* The equilibrium equations for the roller are of the form

$$\mathbf{F} = \mathbf{F}_0 - \int_\Omega \mathbf{p}\, dS = \mathbf{0}\,, \qquad \mathbf{M} = \mathbf{M}_0 - \int_\Omega \mathbf{R} \times \mathbf{p}\, dS = \mathbf{0}\,, \tag{3.28}$$

where $\mathbf{p}$ is the contact stress acting on the second body, $\mathbf{R}$ is the position vector, $\mathbf{F}_0$, $\mathbf{M}_0$ are the resultant and moment resultant of the load exerted on the roller. The

optimization problem can be written as follows

$$\min\Big\{p_{\max}\,\Big|\,p\geq 0,\ d\geq 0,\ p\cdot d=0,\ \text{Coulomb frict. cond.},\ \mathbf{x}\in\Omega\,,\\ \chi=0,\ \mathbf{x}\in\Omega_c,\ \chi\geq 0,\ \mathbf{x}\in\Omega_{nc},\ \mathbf{F}=\mathbf{0},\ \mathbf{M}=\mathbf{0}\Big\},\tag{3.29}$$

where friction conditions are taken into consideration in the rolling motion.

Minimization is solved by using an iteration process. The effect of tangential stress, which is calculated in the rolling problem, is taken into account when determining the displacement in the normal direction during the minimization of the maximum pressure. Therefore the normal displacement from tangential stress p_τ along the direction X is

$$\widetilde{u}_N^\alpha(\mathbf{x})=(-1)^\alpha\int\limits_\Omega H^{(\alpha)\,NT}(\mathbf{x},\mathbf{s})\,p_\tau(\mathbf{s})\,dS\,,\qquad \alpha=1,2,\tag{3.30}$$

where $H^{(\alpha)\,NT}(\mathbf{x},\mathbf{s})$ is the Green-influence function in the α^{th} body.

The normal displacement due to the pressure is as follows

$$u_N^\alpha(\mathbf{x})=(-1)^\alpha\int\limits_\Omega H^{(\alpha)\,NN}(\mathbf{x},\mathbf{s})\,p(\mathbf{s})\,dS\,.\tag{3.31}$$

The displacement difference along normal direction can be written as

$$u_N^2-u_N^1=\int\limits_{S_c}\Big(H^{(1)\,NN}(\mathbf{x},\mathbf{s})+H^{(2)\,NN}(\mathbf{x},\mathbf{s})\Big)p(\mathbf{s})\,dS+\widetilde{u}_N^{(2)}-\widetilde{u}_N^{(1)}-u^1_{\text{rigid}}=\\ =\sum_{\alpha=1}^{2}\int\limits_{S_c}H^{(\alpha)\,NN}(\mathbf{x},\mathbf{s})\,p(\mathbf{s})\,dS+\sum_{\alpha=1}^{2}\int\limits_{S_c}H^{(\alpha)\,NT}(\mathbf{x},\mathbf{s})\,p_\tau(\mathbf{s})\,dS-u^1_{\text{rigid}}\,.\tag{3.32}$$

where u^1_{rigid} is the normal displacement from the rigid body motion of the roller (translation along z and rotation around X).

The radius of the roller is

$$R=R(t),\tag{3.33}$$

which is used to determine the initial gap $h(\mathbf{x})=h(x,t)=h(x,R(t))$ between the bodies. The optimization problem is solved by the iterational method. The following sub-optimization problem is defined, in which the optimized shape is calculated with the control of the contact pressure, where the effect of the tangential stress p_τ on the normal displacement is taken into account. The rolling problem is calculated with the use of the optimized shape, then p_τ is determined and is used to solve the sub-optimization problem again. The optimization problem for calculating the change in radius can be written in the following way

$$\min\Big\{p_{\max}\,\Big|\,p\geq 0,\ d=d(p,p_\tau\ \text{is fixed},R)\geq 0,\ p\cdot d=0\,,\\ \chi(p)\geq 0,\ \mathbf{F}=\mathbf{0},\ \mathbf{M}=\mathbf{0}\Big\}.\tag{3.34}$$

In this task p, $p_{\max}$ and R are unknown variables. The discretized problem is solved by using the iteration recommended in [9].

In the pressure control the change in radius will only be significant in the subdomain Ω_E, which is associated with the end of the roller. In this domain the resultant tangential stress is

$$T = \int\limits_{\Omega_E} p_\tau \, dS \,. \tag{3.35}$$

The iteration continues until the following error limit holds true

$$\frac{|T^{(\mathsf{irol})} - T^{(\mathsf{irol}\,-1)}|}{|T^{(\mathsf{irol})}|} 100 \leq 0.05 \,. \tag{3.36}$$

The iterational algorithm has the following structure

```
LOOP over rolling:  irol=1,...,k convergence
    if (irol .eq.  1) call pressure optimization loop
    Solving the Rolling contact problem with Kalker's program.
    LOOP over pressure optimization:  igap=1,..., convergence
                Solving the optimization problem (3.34)
    END LOOP
    Convergence:  when tolerance (3.36) holds true
 END LOOP
```

3.3.3. *Numerical example.* The roller and an elastic half-space are observed. The radius of the roller is $R = 60\,mm$. The roller is subjected to loads of $F_0 = 5\,kN$ and $M_0 = 87.5\,kNmm$. The proposed zone of the contact region is given by $S_{ct} = 1mm \times S_{cs} = 35mm$, and it is divided into 18×30 rectangular elements, $f_2 = f_3 = 1$, $L_1 = 0\,mm$, $L_2 = 4\,mm$, $L_4 - L_3 = 4\,mm$. The static and kinetic coefficient of friction is $\mu_0 = 0.2$in this example. The displacement of the roller's centerline along the direction X is prescribed as $u_x = 0.005mm$.

Figure 13 the pressure distribution can be seen with and without optimization. The optimized gap is illustrated in section *a.)* of the Figure.

Figure 14 shows the contact stress, pressure (p), tangential stress (Tau $\equiv p_\tau$) in the direction X and the slip function in the contact region. The slip function ($\hat{s}$), illustrated in Figure 14, is calculated by Kalker's routines, which provide the function with reference to the velocity of the roller's center point, and $\hat{s}$ has a value with no dimension. The radius of the roller is R_0, and the velocity of the roller's center point is V_0, i.e. $\omega = \frac{V_0}{R_0}$.

4. **Optimization of roller shape and wear**

The rolling element and the base are in contact and there is a slip area between them, since the surface of the contacting elements undergoes wear. The speed of wear

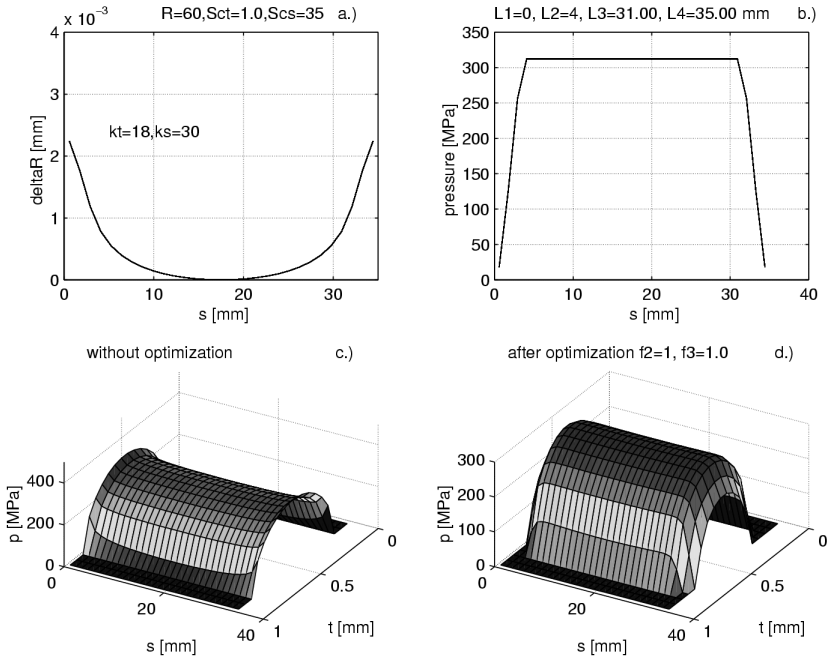

Figure 13. Optimized gap, control function and pressure with and without optimization

is defined by

$$\dot{w} = C\mu\, p||\dot{\mathbf{u}}_\tau|| = C\mu\, p\, \hat{s}\, V_0 = C\mu\, p\, \hat{s}\, R_0\, \omega\,, \tag{4.1}$$

where C is a material property and $\hat{s}$ is the slip, when the rolling velocity is equal to one.

Since the roller rotates while moving forward, the total wear is calculated by the time integration of equation (4.1) by taking the rotational time ($t_\omega = \frac{2\pi}{\omega}$) into account. During time t_* the total wear which exerts an influence on changing the radius is

$$W = \int_0^{\frac{t_*}{t_\omega}} \int_\Omega C\mu\, p\hat{s} R_0 \omega\, d\Omega\, d\tau = \int_0^{\frac{t_*}{t_\omega}} \int_\Omega \widetilde{C}\mu\, p\hat{s}\, d\Omega\, d\tau\,, \tag{4.2}$$

where $\widetilde{C} = CR_0\,\omega$. During the rolling motion the roller is moving along direction X. It is supposed that the wear is evaluated for a Y co-ordinate of the roller by the integral of the $\mu\, p$ and $\hat{s}$ quantities which can change along the direction X, that is

$$W = \int_0^{\frac{t_*}{t_\omega}} \int_0^{S_{cs}} \int_0^{S_{ct}} C\mu\, p(s,t)\hat{s}(s,t)\, dt\, ds\, d\tau\,. \tag{4.3}$$

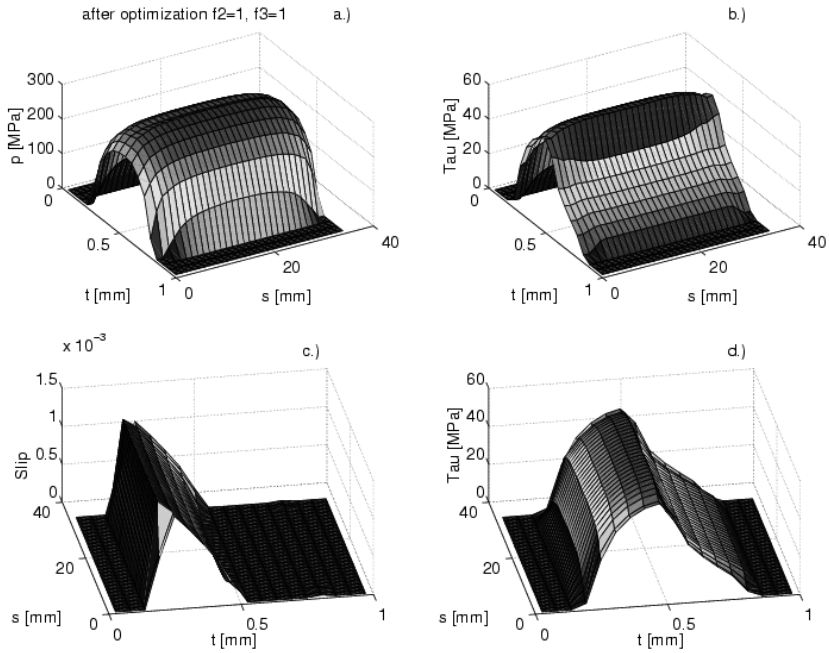

Figure 14. Optimized pressure $\mathbf{p}$, $\mathbf{p}_\tau$ and slip distribution in rolling state

The contact region is divided into small rectangles with size $D_s \times D_t$. There are KX, along the direction X, and KY, along the direction Y, pieces of rectangles. All of the rectangles may have various contact stresses and relative speeds, which are calculated in the middle of these small areas. These quantities are supposed to be constant within the rectangles. In this way the formula (4.3) can be rewritten as

$$W = \int_0^{\frac{t_*}{t_\omega}} \Big(\sum_{j=1}^{\mathsf{KY}} \sum_{i=1}^{\mathsf{KX}} C\mu\, p_{ij} \hat{s}_{ij} D_s D_t \Big)\, d\tau, \tag{4.4}$$

where $p_{ij} = p(s_i, t_j)$, and $\hat{s}_{ij} = \hat{s}(s_i, t_j)$.

During the time integration it is supposed that the pressure and slip vary linearly between τ_n and τ_{n+1} time, which define an interval ${}^{n+1}_{n}\Delta = \tau_{n+1} - \tau_n$. Introducing the parameter $0 \le \Theta \le 1$ the pressure is formulated as

$$p_{ij} = (1 - \Theta) p_{ij}^n + \Theta\, p_{ij}^{n+1}, \tag{4.5}$$

where p_{ij}^n, p_{ij}^{n+1} are pressure at time τ_n, τ_{n+1}. Similar equation can be written for slip too. With the use of (4.5) the following formula can be written

$$\int_{\tau_n}^{\tau_{n+1}} p_{ij}\hat{s}_{ij}\,d\tau = {}^{n+1}_{n}\Delta\Big[\frac{1}{3}\big(p_{ij}^n\,\hat{s}_{ij}^n + p_{ij}^{n+1}\,\hat{s}_{ij}^{n+1}\big) + \frac{1}{6}\big(p_{ij}^n\,\hat{s}_{ij}^{n+1} + p_{ij}^{n+1}\,\hat{s}_{ij}^n\big)\Big] \equiv {}^{n+1}_{n}\Delta\;{}^{n+1}_{n}B_{ij} \tag{4.6}$$

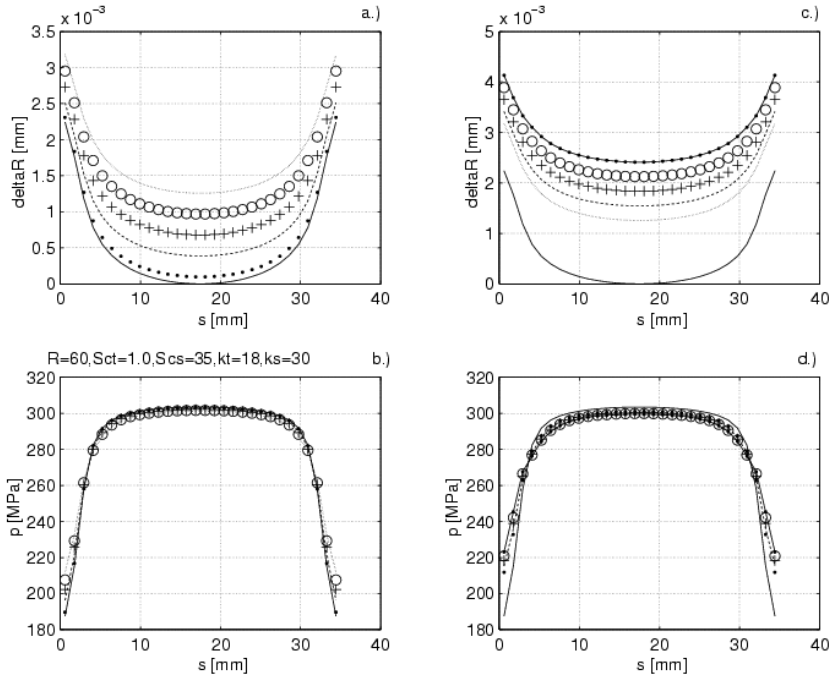

Figure 15. Change in the radius roller

The change in the radius of the roller is

$${}^{n+1}_{n}(\Delta R_j) = \sum_{i=1}^{\mathsf{KX}} {}^{n+1}_{n}B_{ij}\hat{C}D_sD_t\,, \qquad j = 1,\ldots,\mathsf{KY}, \tag{4.7}$$

where $\hat{C} = {}^{n+1}_{n}\Delta\;\widetilde{C}$, and it is calculated in section s_j and ${}^{n+1}_{n}\Delta$ time-interval.

After wear the new radius of the roller can be written as follows

$${}^{n+1}R_j = {}^{n}R_j - {}^{n+1}_{n}(\Delta R_j), \qquad j = 1,\ldots,\mathsf{KY}. \tag{4.8}$$

Figure 15 illustrates the results of a numerical calculation for the wearing process. In sub-figures the symbols stand for the times steps. In *a.*) and *b.*) chars have the following meanings; $-$: optimal shape, $..$: 1^{st} time step, $--$: 2^{nd} time step, $++$:

3^{rd} time step, $\circ\circ$: 4^{th} time step, ...: 5^{th} time step. In of diagrams *c.*) and *d.*) symbols have the meaning: $-$: optimal shape, ...: 5^{th} time step, $--$: 6^{th} time step, $++$: 7^{th} time step, $\circ\circ$: 8^{th} time step, $\bullet-$: 9^{th} time step, the value of parameter $\hat{C}$ is 0.025.

5. Conclusion

Contact optimizations using the control of contact pressure have been performed for many problems. Three groups of contact optimization tasks have been examined.

- In the first group axially symmetric contact problems have been solved by p-extension finite elements. Discretization of the domain with these elements is advantageous, since it results in fast convergence, and high order mapping assures accurate geometry for shape optimization.

  The following contact optimization problems have been solved for axisymmetric bodies:

  1. Minimizing the maximum of contact pressure (Problems P1, P3)
  2. Maximizing the rigid body displacement (Problem P2)
  3. Maximizing the contact resultant force (Problem P4)
  4. Maximizing the torque due to friction (Problems P5, P6)
  5. Minimizing the frictional power loss (Problems P7, P8)
  6. Minimizing the wearing velocities (Problem P9)

- In the second group of optimization problems an optimal shape design of the roller has been carried out. A new control function and three algorithms are proposed.

- In the third group of optimization problems the roller is loaded centrally and the rolling state has been taken into account. A special iterational algorithm has been developed for solving the rolling contact optimization problem. The rolling problem has been solved with Kalker's subroutines in order to calculate the shearing stresses. The influence of friction is not significant and the examples demonstrate the effectiveness of the proposed algorithms.

  Finally, a numerical method is developed for solving the problem of wear. The wearing process is analyzed for a moving roller with optimized shape.

Acknowledgement. We thank professor J. Kalker for the opportunity to utilize the source code calculating the rolling problem. Financial support for this paper was provided by Grants FKFP 0040/1999 and OTKA T025172.

References

1. Mróz, Z.: *Sensitivity analysis of distributed and discretized systems*, Advanced TEMPUS Course on Numerical Methods in Computer Aided Optimal Design, Zakopane, May 11-15, 1992, T. Burczynki [Ed.] Silesian Technical University of Gliwice, Lecture Notes, **Vol. 1.** 1-60, (1992)

2. Klarbring, A.: *Contact, Friction, Discrete Mechanical Structures and Mathematical Programming.* In CISM course: Contact problems: Theory, Methods, Applications, pp. 1-51, Udine, 1997.
3. Hilding, D., Klarbring, A. and Petersson J.: *Optimization of structures in unilateral contact*, Appl. Mech. Rev. **52**(4), (1999), 139-160.
4. Haslinger, J. and Neattaanmaki, P.: *Finite Element Approximation for Optimal Shape Design*, John Wiley & Sons Ltd., London, 1996.
5. Páczelt, I. and Szabó, T.: *Application of the augmented lagrangian technique for solution of contact optimization problems.* In M. Aliabadi and C. Alessandri, editors, Second International Conference Contact Mechanics: Contact Mechanics II, pp. 249-256, Computational Mechanics Publications, London, 1995.
6. Páczelt, I.: *Some new developments in contact pressure optimization*, Engng. Trans., **43**(1-2), (1995), 297-312.
7. Páczelt, I. and Szabó, T.: *Solution of contact optimization problems of cylindrical bodies using the hp-FEM*, Int. J. Numer. Meth. Engng., **53**, (2002), 123-146.
8. Páczelt, I.: *Iterative methods for solution of contact optimization problems*, Arch. Mech., **52**(4-5), (2000), 685-711.
9. Páczelt, I. and Szabó, T.: *Optimal shape design for contact problems*, Structural Optimization, **7**(1/2), (1994), 66-75.
10. Benedict, R. L. and Taylor, J. E.: *Optimal design for elastic bodies in contact*, In Optimization of distributed parameters structures, Part II., E. J. Haug, J. Cea, 1553-1599, Sijthoff and Alphen an den Rijn, 1981.
11. Kikuchi, N. and Taylor, J.E.: *Shape optimization for unilateral elastic contact problems*, In Num. Meth. Coupl. Probl. (Proc. Int. Conf., held at University College, Swansea, Wales), 430-441, 1981.
12. Klarbring, A.: *On the problem of optimizing contact force distributions*, J. Optimization Theory Appl., **74**, (1992), 131-150.
13. Klarbring A. and Haslinger J.: *On almost constant stress distributions by shape optimization*, Structural Optimization, **5**, (1993), 213-216.
14. Conry, I. F. and Seireg, A.: *A mathematical programming method for design of elastic bodies in contact*, J. Appl. Mech. **38**, (1991), 387-392.
15. Oda J., Sakamoto J. and San, K.: *A method for producing a uniform stress distribution in composite with interface*, Structural Optimization, **3**, (1991), 23-28.
16. Páczelt, I. and Herpai, B.: *Some remarks on the solution of contact problems of elastic shells*, Archivum Budowy Maszyn XXIV, (1977), 197-202.
17. Peterson, J.: *Behaviorally constrained contact force optimization*, Structural Optimization, **9**, (1995), 189-193.
18. Szabó, B. and Babuska I.: *Finite Element Analysis*, Wiley-Interscience, New-York, 1991.
19. Kalker J.J.: *Three Dimensional Elastic Bodies in Rolling Contact*, Academic Publisher, Doordrecht, 1990.
20. Béda Gy., Kozák I. and Verhás J.: *Continuum Mechanics*, Academic Publisher, Budapest, 1995.

21. Fancello, E.A. and Feijóo, R.A.: *Shape optimization in frictionless contact problems*, Int. J. Numer. Meth. Engng., **37**, (1994), 2311-2335.

22. Fancello E., Haslinger, J. and Feijóo, R. A.: *Numerical comparison between two cost functionals in contact shape optimization*, Structural Optimization, **9**, (1995), 57-68.

23. Herskovits J., Leontiev A., Dias G. and Santos G.: *Contact Shape Optimization: A bilevel programming approach*, Struc. Multidisc. Optim., **20**, (2000), 214-221.

24. Páczelt, I., Szabó, B. and Szabó, T.: *Solution of contact problem using the hp-version of the finite element method*, Computers and Mathematics with Application, **38**, (1999), 49-69.

25. Strömberg, N., Johanson, L. and Klarbring, A.: *Derivation and analysis of a generalized standard model for contact, friction and wear*, Int. J. Solids Structures, **33**, (1996), 1817-1836.

26. Oh, K. P. and Trachmann, E. G.: *A numerical procedure for designing profiled rolling*, ASME J. Lubrication Technology Series F, **98**, (1996), 68-75.

27. Harnett, M. J.: *The analysis of contact stresses in rolling element bearings*, Trans. ASME, J. Lubrication Technology Series F, **101**, (1979), 105-109.

28. Chiu, Y. P. and Harnett, M. J.: *A numerical solution for the contact problem involving bodies with cylindrical surface considering cylinder effect*, ASME J. Tribology, **109**, (1987), 479-486.

29. de Mul, J. M., Kalker, J.J. and Frederiksson B.: *The contact between arbitrarily curved bodies of finite dimension*, ASME J. Tribology, **108**, (1986), 140-148.

30. Kalker, J.J.: CONPC90*, User's Manual, Listing CONPC*, TU Delft, Faculty of Technical Mathematics and Informatics, 1982, 1986, 1990.

Journal of Computational and Applied Mechanics, Vol. 3., No. 1., (2002), pp. 85–92

APPELL-GIBBS EQUATIONS FOR CLASSICAL WHEEL SHIMMY — AN ENERGY VIEW

Gábor Stépán
Department of Applied Mechanics, Budapest University of Technology and Economics
Műegyetem rkp. 3, 1111 BUDAPEST, Hungary
stepan@mm.bme.hu

[Received: April 2, 2002]

Dedicated to Professor Gyula Béda on the occasion of his seventieth birthday

Abstract. The spatial motion of elastically supported wheels rolling on rough plane surfaces is an old and well-studied problem of classical mechanics. The recent development of nonlinear vibrations theory, the appearance of bifurcation theory, and the description of chaotic motions drew the attention again to this classical problem, reconsidering several partial results we know. This study investigates the lowest degree-of-freedom mechanical model of a shimmying wheel that still exhibits unstable stationary rolling and even chaos. An explanation of the instability is given considering the energy flow in the system with or without the presence of viscous damping.

Mathematical Subject Classification: 37J60, 70F25
Keywords: dynamical systems, local bifurcations, non-holonomic systems

1. Introduction

Since the appearance of Newtonian mechanics, rolling wheels have always been one of the most studied non-trivial problems of classical mechanics. This is due to the practical importance of the problem in engineering, mainly in transportation. The road accidents related to the sometimes unpredictable motion of trucks, articulated buses, trailers, motorcycles still call the attention to the unresolved problems related to the nonlinear dynamics of rolling.

The simplest mechanical models consider a rigid wheel rolling along a straight line in a fixed vertical plane. The rigid wheel has a single contact point with the rigid surface it rolls on, and their connection is described by the so-called Coulomb friction. The distinction between the dynamics induced by the different cases of sticking and sliding friction is now a well-understood task in basic dynamics courses. Vibrations can occur neither in these systems nor in the corresponding mechanical models.

The lateral vibrations of rolling wheels can, however, be experienced during the motion of simple structures like the towed wheels of shopping carts, wheelchairs, trailers, or on the front wheels of bicycles and motorcycles. These vibrations are

often called 'shimmy'. The common meaning of the word shimmy is a dance back in the early thirties of the last century. This shows that the phenomenon named by the same word, shimmy, has been studied for several decades already. The earliest scientific study the author could find is that of Schlippe *et al.* (1941). The mechanical models of shimmy contain wheels that are towed via a shaft about which they can rotate. This way, the wheels can choose the direction of their rolling and this direction can change during the course of the motion. In these mechanical models the wheel is not constrained to remain in a single prescribed vertical plane.

The subsequent chapters present the simplest mechanical model that describes shimmy, then the construction of the Appell-Gibbs equations of motion, the results of their linear and nonlinear analysis, and conclusions regarding the energy flow in the system.

2. Mechanical model

The model presented in Figure 1 has the lowest number of degrees of freedom that still describes the shimmy phenomenon. The model has four essential elements: the vehicle of mass m_v, the king pin supported by springs of overall stiffness s, the caster of mass m_c and of length l, and the wheel of mass m_w and of radius R. The vehicle is modelled as a rigid body running straight with a constant velocity $\mathbf{v}$ on the horizontal plane (x, y). Clearly, the towed wheel can exhibit only the straight stationary running if the king pin is rigidly supported.

In vehicle dynamics, this model is considered to be realistic for rigid wheels without pneumatic tyres at low running speed v (see Plaut, 1996, O'Railley, 1999, Coleman *et al.*, 1999). In other cases, the elasticity of the wheel is usually more relevant than that of the king pin. The tyre/ground contact can be modelled by means of the so-called creep force (see Pacejka, 1988, Kalker, 1990, Böhm *et al.* (1989)). Although the creep force is a stationary idea, it can still be used successfully in linear calculations: Scheidl *et al.* (1985) can be mentioned here for tractor-semi-trailer systems, the analysis of Sharp and Jones (1980) and Limebeer *et al.* (2001) for motorcycles, and that of Fratile *et al.* (1995) for caravans.

Although, the model in Figure 1 has limited value in studying engineering problems in practice, we still go ahead with its detailed analysis since it draws attention to some important physical conclusions regarding the nonlinear vibrations of these systems.

There are several constraints in this system. The vehicle can move in the x direction only, the king pin can move in the lateral direction y relative to the vehicle body, the caster can rotate about the vertical axis by the angle ψ relative to the vehicle, and the wheel can rotate about the horizontal axis η by the angle φ. These stationary geometrical constraints leave four degrees of freedom for this chain of four rigid bodies described by the four scalar state variables x, y, ψ and φ.

There are further constraints. The constant speed of towing can be modelled as a non-stationary (simple, but still time dependent) geometrical constraint:

$$x - vt = 0\,. \tag{2.1}$$

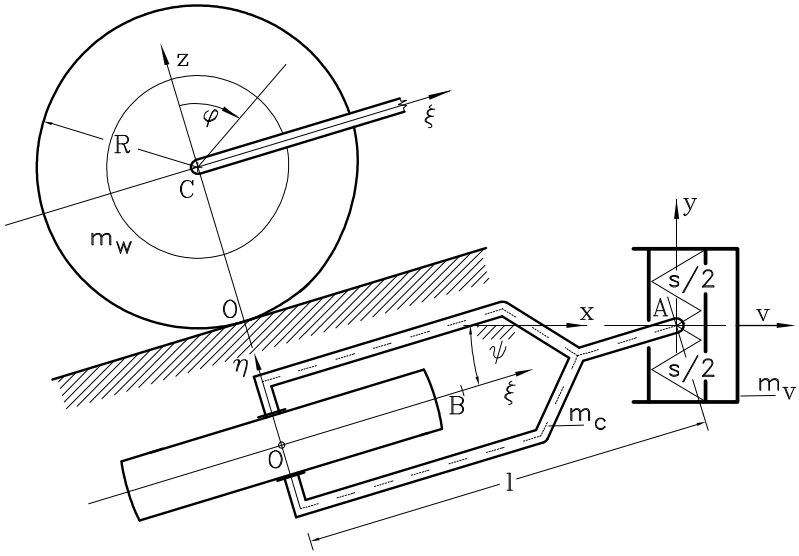

As a consequence, the system is rheonomic. There is also a stationary but kinematical constraint, namely the rolling condition

$$\mathbf{v}_P = \begin{pmatrix} v_{Px} \\ v_{Py} \end{pmatrix} = \begin{pmatrix} v + l\dot{\psi}\sin\psi - R\dot{\varphi}\cos\psi \\ \dot{y} - l\dot{\psi}\cos\psi - R\dot{\varphi}\sin\psi \end{pmatrix} = \begin{pmatrix} 0 \\ 0 \end{pmatrix} . \tag{2.2}$$

As a consequence, the system is non-holonomic. The constraining equation (2.1) decreases the number of degrees of freedom by one. The two scalar kinematical constraints in (2.2) provide two scalar first order differential equations. These result in an overall decrease in the degrees of freedom by another one. Thus, the system has only two degrees of freedom left, the corresponding state space is four dimensional, and the equations of motion can be arranged into a system of four first order ordinary differential equations. Due to the simple form of the non-stationary constraint (2.1), these equations are still autonomous.

In spite of the fact that the only active force has the usual time-independent potential function of a linear spring, this system is not conservative due to its non-holonomic rheonomic nature.

3. **Equations of motion**

Because of the geometrical constraint (2.1), only three general coordinates are chosen: y, ψ and φ. In order to construct the simplest form of the equations of motion, we present the construction of the Appell-Gibbs equations (see Gantmacher, 1975). To do so, so-called pseudo velocities have to be chosen. The number of these velocities is equal to the difference between the number of the general coordinates and the number of the kinematical constraints, that is, $3 - 2 = 1$. The simplest choice for this pseudo

velocity is the angular velocity ω of the caster:

$$\dot{\psi} = \omega\,. \tag{3.1}$$

The kinematical constraints (2.2) and the pseudo velocity definition (3.1) can be arranged into a system of linear algebraic equations:

$$\begin{pmatrix} 0 & l\sin\psi & -R\cos\psi \\ 1 & -l\cos\psi & -R\sin\psi \\ 0 & 1 & 0 \end{pmatrix} \begin{pmatrix} \dot{y} \\ \dot{\psi} \\ \dot{\varphi} \end{pmatrix} = \begin{pmatrix} -v \\ 0 \\ \omega \end{pmatrix}. \tag{3.2}$$

The solution of these equations gives a unique description of the general velocities by the pseudo velocity and the general coordinates themselves:

$$\begin{pmatrix} \dot{y} \\ \dot{\psi} \\ \dot{\varphi} \end{pmatrix} = \begin{pmatrix} v\tan\psi + \dfrac{l}{\cos\psi}\omega \\ \omega \\ \dfrac{v}{R\cos\psi} + \dfrac{l}{R}\omega\tan\psi \end{pmatrix}. \tag{3.3}$$

The general accelerations can also be expressed by the same general coordinates, the pseudo velocity ω and the pseudo acceleration $\dot{\omega}$:

$$\begin{pmatrix} \ddot{y} \\ \ddot{\psi} \\ \ddot{\varphi} \end{pmatrix} = \begin{pmatrix} \dfrac{v}{\cos^2\psi}\omega + \dfrac{l\tan\psi}{\cos\psi}\omega^2 + \dfrac{l}{\cos\psi}\dot{\omega} \\ \dot{\omega} \\ \dfrac{v\tan\psi}{R\cos\psi}\omega + \dfrac{l}{R\cos^2\psi}\omega^2 + \dfrac{l}{R}\dot{\omega}\tan\psi \end{pmatrix}. \tag{3.4}$$

With the help of the above general accelerations, the so-called acceleration energy S can be calculated. The formula of the total acceleration energy of the system consists of the partial acceleration energies of the caster and the wheel, where the corresponding accelerations of the centres of gravity are $\mathbf{a}_B$ and $\mathbf{a}_C$, the angular velocities are $\mathbf{\Omega}_c$ and $\mathbf{\Omega}_w$, while the angular accelerations are $\dot{\mathbf{\Omega}}_c$ and $\dot{\mathbf{\Omega}}_w$:

$$\begin{aligned} S = {} & \frac{1}{2}m_c\mathbf{a}_B^2 + \frac{1}{2}\dot{\mathbf{\Omega}}_c^T\mathbf{J}_B\dot{\mathbf{\Omega}}_c + (\dot{\mathbf{\Omega}}_c\times\mathbf{\Omega}_c)^T(\mathbf{J}_B\mathbf{\Omega}_c) + \\ & + \frac{1}{2}m_w\mathbf{a}_C^2 + \frac{1}{2}\dot{\mathbf{\Omega}}_w^T\mathbf{J}_C\dot{\mathbf{\Omega}}_w + (\dot{\mathbf{\Omega}}_w\times\mathbf{\Omega}_w)^T(\mathbf{J}_C\mathbf{\Omega}_w) + \dots\,. \end{aligned} \tag{3.5}$$

In this formula, the dots refer to terms that do not contain the pseudo acceleration $\dot{\omega}$, the superscript T refers to transposed vectors, and $\mathbf{J}_{B,C}$ are the corresponding matrices of mass moments of inertia. In the calculations, only the simplified elements

$$J_{Bz} = \frac{1}{12}m_c l^2\,, \quad J_{C\eta} = \frac{1}{2}m_w R^2\,, \quad J_{Cz} = \frac{1}{4}m_w R^2$$

are used.

Using the formulae (3.3) and (3.4), the kinematical analysis of the structure gives the accelerations, angular velocities and angular accelerations as functions of the general coordinates, the pseudo velocity and the pseudo acceleration. Actually, only the angle ψ of the caster will appear among the general coordinates, and the final

formula of the acceleration energy assumes the form:

$$S(\dot\omega,\omega,\psi) =$$
$$\frac{1}{2}m_c l^2\left(\dot\omega^2\left(\frac{1}{\cos^2\psi}-\frac{2}{3}\right)+\dot\omega\omega\frac{v}{l}\left(\frac{2}{\cos^3\psi}-\frac{1}{\cos\psi}\right)+2\dot\omega\omega^2\frac{\sin\psi}{\cos^3\psi}\right)+$$
$$+\frac{1}{2}m_w l^2\left(\dot\omega^2\left(\frac{3}{2}\tan^2\psi+\frac{R^2}{4l^2}\right)+3\dot\omega\omega\frac{v}{l}\frac{\sin^2\psi}{\cos^3\psi}+3\dot\omega\omega^2\frac{\sin\psi}{\cos^3\psi}\right)+\dots . \tag{3.6}$$

This formula provides the left hand side of the Appell-Gibbs equation. In the right hand side, the so-called pseudo force Π has to be calculated via the virtual power of the single active force caused by the springs at the king pin A. If δ denotes virtual quantities, this calculation gives

$$\delta P = \mathbf{F}_A^T\delta\mathbf{v}_A = \begin{pmatrix}0 & -sy & 0\end{pmatrix}\delta\begin{pmatrix}0\\-\dot y\\ vt\end{pmatrix} = -sy\delta\dot y =$$
$$-sy\delta\left(\frac{l}{\cos\psi}\omega+v\tan\psi\right) = -sy\frac{l}{\cos\psi}\delta\omega = \Pi\delta\omega\,, \tag{3.7}$$

that is, the pseudo force depends only on the general coordinates y and ψ as follows:

$$\Pi(y,\psi) = -sl\frac{y}{\cos\psi}\,. \tag{3.8}$$

The four dimensional system of first order ordinary differential equations of the two degree of freedom system consists of the single scalar Appell-Gibbs equation

$$\frac{\partial S}{\partial\dot\omega} = \Pi\,, \tag{3.9}$$

and the 3 scalar equations (3.3) of the general velocities:

$$\begin{aligned}
\dot\omega &= -\frac{\frac{v}{l}\Big(\frac{1}{\cos^2\psi}-\frac{1}{2}+\frac{3m_w}{2m_c}\tan^2\psi\Big)\omega+\frac{s}{m_c l}y+\Big(1+\frac{3m_w}{2m_c}\Big)\frac{\sin\psi}{\cos^2\psi}\omega^2}{\Big(\frac{1}{3}+\tan^2\psi\Big)\cos\psi+\frac{m_w}{4m_c}\Big(\frac{R^2}{l^2}+6\tan^2\psi\Big)\cos\psi}\\
\dot y &= v\tan\psi+l\frac{\omega}{\cos\psi}\\
\dot\psi &= \omega\\
\dot\varphi &= \frac{v+l\omega\sin\psi}{R\cos\psi}\,.
\end{aligned} \tag{3.10}$$

Since the general coordinate φ appears neither in the acceleration energy S nor in the pseudo force Π, this coordinate takes the role of a so-called cyclic coordinate, and the corresponding last scalar equation of (3.10) can be separated from the first three equations. Thus, the system can uniquely be described in the three dimensional phase space of the pseudo velocity ω (i.e. the angular velocity of the caster), the lateral displacement y of the king pin, and the angle ψ of the caster.

4. **Stability and nonlinear vibrations**

The stationary running of the towed wheel is characterised by the following solution of the equations of motion (3.10):

$$\omega \equiv 0\,, \quad y \equiv 0\,, \quad \psi \equiv 0\,, \quad \varphi = \frac{v}{R}t + \varphi_0$$

If the first three equations of (3.10) are linearised about their trivial zero solution with respect to the small perturbations x_1, x_2 and x_3, a three dimensional linear ODE is obtained in the form:

$$\dot{\mathbf{x}} = \mathbf{A}\mathbf{x}$$

with the coefficient matrix

$$\mathbf{A} = \begin{pmatrix} -\dfrac{6\frac{v}{l}}{4+3\frac{m_w}{m_c}\frac{R^2}{l^2}} & -\dfrac{12\frac{s}{m_c l}}{4+3\frac{m_w}{m_c}\frac{R^2}{l^2}} & 0 \\ l & 0 & v \\ 1 & 0 & 0 \end{pmatrix}. \tag{4.1}$$

The characteristic equation $\det(\lambda\mathbf{I} - \mathbf{A}) = 0$ can be transformed into the 3rd degree polynomial equation

$$\left(4 + 3\frac{m_w}{m_c}\frac{R^2}{l^2}\right)\lambda^3 + 6\frac{v}{l}\lambda^2 + 12\frac{s}{m_c}\lambda + 12\frac{s}{m_c}\frac{v}{l} = 0\,. \tag{4.2}$$

The real parts of all the three characteristic roots $\lambda_{1,2,3}$ are negative, and the stationary running of the towed wheel is asymptotically stable, if and only if the conditions of the Routh-Hurwitz criterion are fulfilled. Since all the coefficients of (4.2) are positive, the only condition to be satisfied is the positivity of the Hurwitz determinant:

$$\det\begin{pmatrix} 6\frac{v}{l} & 12\frac{s}{m_c}\frac{v}{l} \\ 4+3\frac{m_w}{m_c}\frac{R^2}{l^2} & 12\frac{s}{m_c} \end{pmatrix} > 0\,,$$

that is,

$$\frac{l}{R} > \sqrt{\frac{3}{2}\frac{m_w}{m_c}}\,. \tag{4.3}$$

The physical meaning of the result is clear: the longer the caster is, the more stable the structure is.

However it is not obvious at this point, how the nonlinear vibrations develop when the stationary running is unstable. Where does the system take the energy from to increase its kinetic energy during its oscillations?

The nonlinear analysis of the system does not give an answer to this. As it was shown in the paper of Stépán (1991), Hopf bifurcation occurs at the limit of stability defined by the equality in (4.3). Physically, self-excited nonlinear vibrations are expected there. However, a tedious algebraic calculation proves that the sense of the Hopf bifurcation is subcritical. This means that an unstable periodic motion exists around the stable stationary motion of the towed wheel, that is, even the domain of attraction of stable running is finite. As a numerical simulation also confirms, there is an attractor neither outside the unstable periodic oscillation, nor outside the unstable

stationary motion of the rolling system — the rolling system looks globally unstable. Although the change of the dynamics of the rolling wheel to the dynamics of a sliding wheel at large vibration amplitudes explains the presence of an either periodic, quasi-periodic or chaotic attractor outside the unstable rolling (see Stépán, 1999), the question on the energy flow of the unstable rolling system is not answered this way.

5. **Conclusions**

The rheonomic non-holonomic system of the simplest shimmying wheel structure for pure rolling shows instability. The increasing vibrations have to be excited by an external force having an overall positive work. The only active force in the system is the linear spring force. The pseudo force Π in the Appell-Gibbs equation is also related to the presence of this spring force. It has a potential function, so it cannot be the source of the energy input.

All the constraining forces that provide the kinematical constraint of rolling are ideal in the sense that their virtual power, and their actual power is also zero, since the velocity of their point of application P is prescribed to be zero. All the other stationary geometrical constraining forces are ideal, and their power is also zero.

The non-stationary geometrical constraining force $\mathbf{F}_v$ that provides the constant running speed $\mathbf{v}$ of the vehicle is also ideal since its virtual power is zero again:

$$\delta P_v = \mathbf{F}_v^T \delta \mathbf{v} = F_{v,x} 0 = 0\,.$$

Thus, all the constraining forces are ideal, and neither of them appear in the most dense Appell-Gibbs equations of motion. But the constraining force $\mathbf{F}_v$ that pulls the vehicle has non-zero real power:

$$P_v = \mathbf{F}_v^T \mathbf{v} = F_{v,x} v \neq 0\,.$$

This power may change in time, naturally. This non-stationary constraint is the source of the external energy that can excite the system.

This explanation of the energy flow in case of unstable stationary running, that is, in case of a shimmy, can be confirmed also experimentally. When a shopping cart is towed, the force we apply alternates as the wheel oscillates. The increasing vibration amplitudes make the cart increasingly difficult to pull. This shows clearly, that the violent vibrations related to shimmy are supported by the constraining force that tries to provide the constant running speed of the cart.

As it was already pointed out in the introduction, the above rheonomic non-holonomic system is not conservative, in spite of the fact that its equations of motion are autonomous, all the active forces have time-independent potential functions, and all the constraints are ideal.

Acknowledgement. The author wishes to thank for the useful discussions with Professor Gyula Béda on the energy view of the shimmy phenomenon. This research was supported by the Hungarian National Science Foundation under Grant No. OTKA T030762/99.

References

1. Böhm, F. and Kollatz, M.:*Some Theoretical Models for Computation of Tire Nonuniformities*, Fortschrittberichte VDI, **12.124**, VDI Verlag, Berlin, 1989.
2. Coleman, M. J., Garcia, M., Ruina, A. L., Camp, J. S. and Chatterjee, A.: *Stability and chaos in passive-dynamic locomotion*, in Applications of Nonlinear and Chaotic Dynamics in Mechanics (Ed.: F. C. Moon), Kluwer Academic Publisher, Dordrecht, 407-416, 1999.
3. Fratila, D. and Darling, J.: *Improvements to car/caravan handling and high speed stability through computer simulation*, in Proceedings of the ASME International Mechanical Engineering Congress (San Francisco, 1995) **95-WA/MET-9** pp. 1-15., 1995.
4. Gantmacher, F.: *Lectures in Analytical Mechanics*, Moscow, Mir Publishers, 1970.
5. Kalker, J. J.: *Wheel-rail rolling contact*, Wear, **144**, (1990), 243-261.
6. Limebeer, D. J. N., Evangelou, S. and Sharp, R. S.: *Stability of motorcycles under acceleration and braking*, in Proceedings of 18th ASME Biennial Conference on Mechanical Vibration and Noise (Pittsburgh, 2001) (Eds: S. Sinha, B. Balachandran) DETC01/VIB-21603 pp. 1-9., 2001.
7. O'Railley, O. M. and Varadi, P. C.: *A traveller's woes: some perspectives from dynamical systems*, in Applications of Nonlinear and Chaotic Dynamics in Mechanics, (Ed.: F. C. Moon), Kluwer Academic Publisher, Dordrecht, pp. 397-406, 1999.
8. Pacejka, H.: *Modelling of the pneumatic tyre and its impact on vehicle dynamic behaviour*, Research report **i72B**, TU Delft, 1988.
9. Plaut, R. H.: *Rocking instability of a pulled suitcase with two wheels*, Acta Mechanica, **117**, (1996), 165-179.
10. Scheidl, R., Stribersky, A., Troger, H. and Zeman, K.: *Nonlinear stability behaviour of a tractor-semitrailer in downhill motion*, in Proceedings of the 9th IAVSD Symposium (Linköping, 1985), pp. 509-522.
11. Schlippe, B. v. and Dietrich, R.: *Shimmying of a pneumatic wheel*, Lilienthal-Gesellschaft für Luftfahrtforschung, Bericht **140**, 1941. (Translated for the AAF in 1947 by Meyer & Company, 125-160.)
12. Sharp, R. S. and Jones, C. J.: *A comparison of tyre representations in a simple wheel shimmy problem*, Vehicle System Dynamics, **9**, (1980), 45-57.
13. Stépán, G.: *Chaotic motion of wheels*, Vehicle System Dynamics, **20**, (1991), 341-351.
14. Stépán, G.: *Delay, nonlinear oscillations and shimmying wheels*, in Applications of Nonlinear and Chaotic Dynamics in Mechanics (Ed.: F. C. Moon), Kluwer Academic Publisher, Dordrecht, pp. 373-386, 1999.

Journal of Computational and Applied Mechanics, Vol. 3., No. 1., (2002), pp. 93–101

VOLUME DEPENDENT STRENGTH OF POROUS MATERIALS AND STRUCTURES

Surot Thangjitham and Robert A. Heller
Department of Engineering Science and Mechanics
Virginia Tech, Blacksburg, Virginia, USA
thangjitham@vt.edu

[Received: April 6, 2002]

Dedicated to Professor Gyula Béda on the occasion of his seventieth birthday

Abstract. The size effects in reliability problems of porous materials and structures are considered in this study. The proposed analysis relies on a modified Weibull distribution with mean strength-volume relations obtained from experiments. The procedure is then applied to finite plates with circular holes of increasing diameters. Because of the nonlinearity of the stressed volume in the vicinity of the holes, the volume dependence of the strength becomes pronounced. The probability of survival of such plates is calculated and indicates a strong dependence on the stressed volume of the plate.

Mathematical Subject Classification: 74K20, 74M99, 74R99
Keywords: Weibull distribution, volume dependent, stress concentration, reliability analysis

1. Introduction

It is common knowledge that engineering materials are prone to size effects. Carefully prepared laboratory size specimens are usually stronger than full size structural components. This occurrence is especially true for brittle and porous materials such as ceramics and concrete. In previous studies, this phenomenon was treated on the basis of the Weakest Link Theory and the Weibull distribution [1-2]. According to the analysis, a component is assumed to be composed of a large number of elements (characteristic volume) of random strength that are connected in a series combination. The random variation of the element strength is mainly characterized by the number and geometry of initial flaws contained in the element. The failure of the component is assumed to occur when any one of the elements fails. The reliability of the component decreases, therefore, as the number of the elements (material volume) increases. Consequently, the reliability approaches unity as the volume of the material is reduced to zero and approaches zero as the volume increases. While this type of analysis gives reasonable results for intermediate size elements, it predicts an unlimited increase in strength as the volume approaches zero [3-8].

Recent researches have been focused on the development of mathematical models to predict size effects in materials [9-14]. Both micro- and macro-mechanical models have been proposed to relate material and geometrical parameters to size effects. However, no unified relation applicable to a large class of materials has yet been established. Instead, many empirical models have been used to extrapolate size effects in laboratory specimens to size effects in practical components.

A hyperbolic function has been used to define the size effect phenomenon [9-11] in ceramics and cementitious materials. Such a relationship assumes that the smallest volume is strongest while for large volumes the strength diminishes to zero. Observations on porous materials, however, indicate that strength does not increase monotonically for small volumes. As the volume approaches the size of the pores, its strength becomes weaker. A maximum strength, on the other hand, is observed for intermediate sizes, diminishing again to a nonzero value for structural components. As a result, a hyperbolic function for size effect, where strength is monotonically increasing with decreasing volume, is no longer applicable. To account for such observations, a modified size effect function is introduced and is used in the reliability analysis of porous structures.

2. Size Effect Function

The mean strength of a given volume v, $\bar{r}(v)$, is expressed in terms of the characteristic mean strength, $\bar{r}_c$, and the size effect function $\xi(\rho)$ as

$$\bar{r}(v) = \bar{r}_c \xi(\rho) \tag{2.1}$$

where $\rho = v/v_c$ is the volume ratio with v_c the characteristic volume of the material. Size effect is modelled as a combination of a classical hyperbolic relationship [11] and a Rayleigh type function

$$\xi(\rho) = \alpha_\infty + \frac{\alpha_1}{\sqrt{1+\beta_1 \rho}} + \alpha_2 \exp[-\beta_2 (\ln \rho - \gamma_2)^2] \tag{2.2}$$

with α_∞ the minimum value asymptotically approached for larger volumes, α_1 and β_1 the parameters for the classical hyperbolic size effect function, and α_2, β_2, and γ_2 the parameters for the Rayleigh type size effect function. These parameters characterize the size effects of materials such that

$$\lim_{\rho \to 0} \xi(\rho) = \alpha_\infty + \alpha_1 = \frac{\bar{r}_0}{\bar{r}_c} \qquad \text{(micro mean strength)} \tag{2.3}$$

$$\lim_{\rho \to \infty} \xi(\rho) = \alpha_\infty = \frac{\bar{r}_\infty}{\bar{r}_c} \qquad \text{(macro mean strength)} \tag{2.4}$$

$$\lim_{\rho \to 1} \xi(\rho) = \alpha_\infty + \frac{\alpha_1}{\sqrt{1+\beta_1}} + \alpha_2 e^{-\beta_2 \gamma_2^2} = 1 \qquad \text{(characteristic strength)} \tag{2.5}$$

where $\bar{r}_0$, $\bar{r}_\infty$, and $\bar{r}_c$ are the micro-, macro-, and characteristic mean strengths of materials, respectively.

For the purposes of illustration, the following coefficients $\alpha_\infty = 0.3587$, $\alpha_1 = 0.5380$, $\alpha_2 = 0.2690$, $\beta_1 = 0.2$, $\beta_2 = 0.3$, $\gamma_2 = 2$ are used. Figure 1 shows the variations of the size effect function $\xi(\rho)$ and of the hyperbolic function.

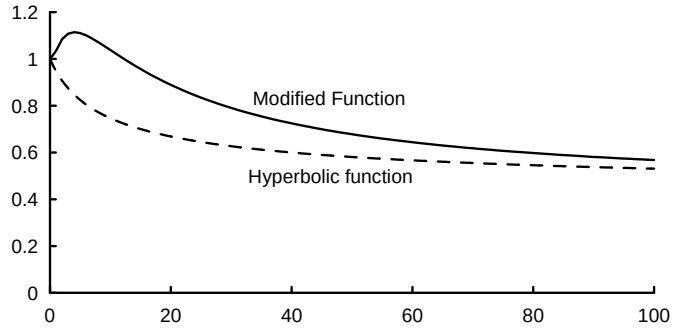

Figure 1. Size effect $\xi(\rho)$ as a function of volume ratio $\rho = v/v_c$.

The parameters in the above equations are obtained from experiments on specimens of various sizes where mean strength and dispersion (standard deviation) are measured. To analyze the reliability of a component with a given size, its mean strength is obtained from (2.2) and is then used in a two parameter Weibull distribution given as

$$f_R(r,\rho) = \frac{\eta}{\lambda}\left(\frac{r}{\lambda}\right)^{\eta-1} \exp\left[-\left(\frac{r}{\lambda}\right)^{\eta}\right] \tag{2.6}$$

where the parameters η and λ are obtained as

$$\frac{1}{\Gamma\left[1+\frac{1}{\eta}\right]^2}\left(\Gamma\left[1+\frac{2}{\eta}\right] - \Gamma\left[1+\frac{1}{\eta}\right]^2\right) - \delta^2 = 0\,, \tag{2.7}$$

$$\lambda(\rho) = \frac{\bar{r}_c \xi(\rho)}{\Gamma\left[1+\frac{1}{\eta}\right]} \tag{2.8}$$

where δ is the coefficient of variation and $\Gamma[.]$ is the gamma function.

The corresponding reliability function for a given level of induced stress, σ, is obtained as

$$L(\sigma,\rho) = \exp\left[-\left(\frac{\sigma}{\lambda}\right)^{\eta}\right] \tag{2.9}$$

As an illustration, a set of density functions, $f_R(r,\rho)$ is presented in Figure 2 for a characteristic mean strength, $\bar{r}_c = 30$ MPa, a coefficient of variation, $\delta = 0.2$ and various volume ratios, $\rho = v/v_c$. Figure 3 is a three dimensional plot of the density function $f_R(r,\rho)$. Reliability functions are plotted in Figure 4.

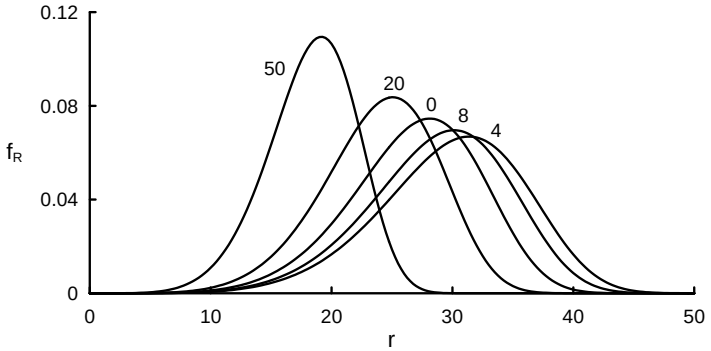

Figure 2. Probability densities $f_R(r, \rho)$ as functions of strength, r, for various volume ratios, ρ.

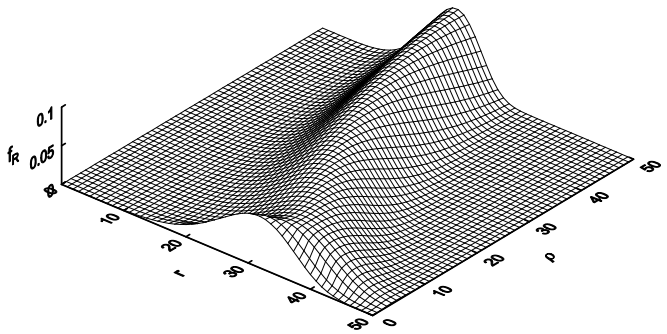

Figure 3. Variations of probability densities $f_R(r, \rho)$ as functions of strength, r, and volume ratio, ρ.

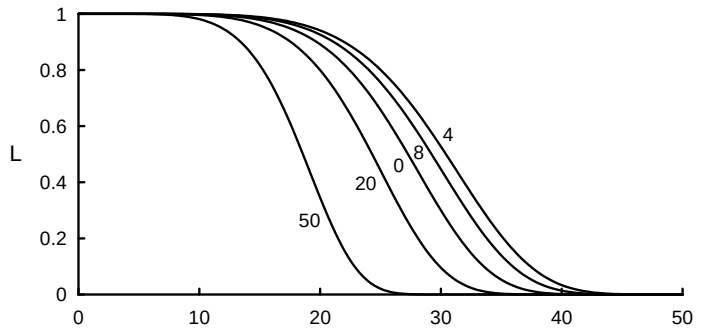

Figure 4. Reliabilities, $L(\sigma, \rho)$, as functions of applied stress, σ, for various volume ratios, ρ.

It is seen that the reliability of a component is volume dependent, first increasing and then decreasing with increasing volume. The reliabilities for a uniform plate

subjected to far-field applied uniform stress σ_0 along the x_2-direction (Figure 5 as $a \to 0$), are plotted in Figure 6 as functions of plate volume ratios ρ for various values of applied stress.

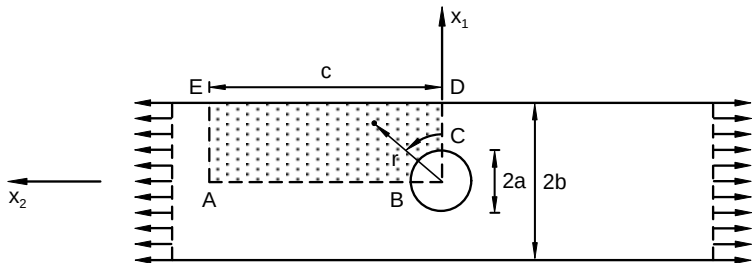

Figure 5. Plate geometry.

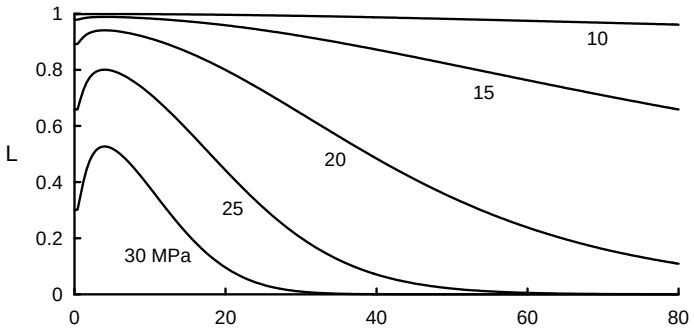

Figure 6. Reliabilities as functions of plate volume ratio, ρ, for various levels of applied stress σ_0.

3. **Analysis of Plates with Circular Holes**

Plates of unit thickness with various hole sizes, as shown in Figure 5, are analyzed. As the hole diameter is varied, the stressed volume of material in the vicinity of the hole also changes.

Stresses in terms of the stress functions, $\Phi(r,\theta)$, in polar coordinates (r,θ) are given by

$$\sigma_{rr}(r,\theta) = \frac{1}{r}\frac{\partial \Phi}{\partial r} + \frac{1}{r^2}\frac{\partial^2 \Phi}{\partial \theta^2}\,, \tag{3.1}$$

$$\sigma_{\theta\theta}(r,\theta) = \frac{\partial^2 \Phi}{\partial r^2}\,, \tag{3.2}$$

$$\sigma_{r\theta}(r,\theta) = -\frac{\partial}{\partial r}\left(\frac{1}{r}\frac{\partial \Phi}{\partial \theta}\right)\,. \tag{3.3}$$

The general solution for the stress function

$$\Phi(r,\theta) = \phi_0 + \phi_1 e^{i\theta} + \sum_{n=1}^{\infty} \phi_n e^{in\theta} \tag{3.4}$$

where

$$\phi_0(r) = a_0 + b_0 \ln r + c_0 r^2 + d_0 r^2 \ln r\,, \tag{3.5}$$

$$\phi_1(r) = a_1 r + b_1 r^{-1} + c_1 r^3 + d_1 r \ln r\,, \tag{3.6}$$

$$\phi_n(r) = a_n r^{-n} + b_n r^{2-n} + c_n r^n + d_n r^{2+n} \tag{3.7}$$

with integration constants a_n, b_n, c_n, and d_n; $n = 0, 1, 2, \ldots$, to be evaluated by applying the proper boundary conditions.

For an infinite plate subjected to far-field uniaxial stress, σ_0, in the x_2-direction, equations (3.1)-(3.3) are reduced to

$$\sigma_{rr}(r,\theta) = \frac{1}{2}\sigma_0 \left[\left(1 - \frac{a^2}{r^2}\right) - \left(1 - 4\frac{a^2}{r^2} + 3\frac{a^4}{r^4}\right)\cos 2\theta \right], \tag{3.8}$$

$$\sigma_{\theta\theta}(r,\theta) = \frac{1}{2}\sigma_0 \left[\left(1 + \frac{a^2}{r^2}\right) + \left(1 + 3\frac{a^4}{r^4}\right)\cos 2\theta \right], \tag{3.9}$$

$$\sigma_{r\theta}(r,\theta) = \frac{1}{2}\sigma_0 \left(1 + 2\frac{a^2}{r^2} - 3\frac{a^4}{r^4}\right)\sin 2\theta\,. \tag{3.10}$$

The stress functions ϕ_n; $n = 0, 1, 2, \ldots$, for a semi-infinite plate (Figure 5), also loaded with far-field uniaxial stress σ_0, in the x_2-direction, satisfying the traction-free boundary conditions at the hole surface of radius a, are given as

$$\phi_0(r) = a_0 + b_0 \left(\ln r - \frac{r^2}{2a^2}\right), \tag{3.11}$$

$$\phi_1(r) = a_1 r + b_1 \left(\frac{a^4 + r^4}{a^4 r}\right), \tag{3.12}$$

$$\begin{aligned} \phi_n(r) \;=\; & a_n \left(r^{-n} - (n+1)\, a^{-2n} r^n + n a^{-2(n+1)} r^{n+2}\right) + \\ & b_n \left(r^{2-n} - (n+1)\, a^{-2(n-1)} r^n + n a^{-2n} r^{n+2}\right). \end{aligned} \tag{3.13}$$

It is noted that only two integration constants (a_n and b_n) remain to be determined by the traction-free boundary conditions on the free edges at $x_1 = \pm b$ and the far-field stress boundary conditions at $x_2 \to \infty$.

Because of symmetry of loading and plate geometry, the stress function is reduced to

$$\Phi(r,\theta) = \phi_0 + \sum_{n=2,4,6,\ldots}^{\infty} \phi_n(r)\, e^{in\theta}\,. \tag{3.14}$$

Depending on the level of accuracy required, the stress function is truncated to a finite number of N functions, ϕ_n; $n = 0, 1, 2, \ldots, N$. This leads to a total number of $2N + 1$ constants (a_0 is not required in the stress expressions) that need to be evaluated. To accomplish this, the method of least squared boundary collocation is used.

The rectangular stress components, σ_{11}, σ_{22}, and σ_{12} are obtained as

$$\sigma_{11}(r,\theta) = \frac{\sigma_{rr}+\sigma_{\theta\theta}}{2} + \frac{\sigma_{rr}-\sigma_{\theta\theta}}{2}\cos 2\theta - \sigma_{r\theta}\sin 2\theta\,, \tag{3.15}$$

$$\sigma_{22}(r,\theta) = \frac{\sigma_{rr}+\sigma_{\theta\theta}}{2} - \frac{\sigma_{rr}-\sigma_{\theta\theta}}{2}\cos 2\theta + \sigma_{r\theta}\sin 2\theta\,, \tag{3.16}$$

$$\sigma_{12}(r,\theta) = \frac{\sigma_{rr}-\sigma_{\theta\theta}}{2}\sin 2\theta + \sigma_{r\theta}\cos 2\theta\,. \tag{3.17}$$

The average normal stress in the net area $(b-a)$ is calculated as

$$\sigma_{\text{avg}} = \frac{1}{b-a}\int_a^b \sigma_{rr}(r,0)dr\,. \tag{3.18}$$

4. **Probability Analysis of Plates with Holes**

The stresses in semi-infinite plates with various widths $(2b)$ and hole sizes $(2a)$ have been calculated using (3.11)-(3.17). The average stress has also been obtained from (3.18). In order to examine the volume effects created by the presence of holes, average stresses were calculated for applied stresses σ_0 of 20 MPa and 25 MPa and their reliabilities were computed from (2.9).

The results are plotted in Figs. 7 and 8 as functions of the plate volume ratio ρ for several plate width to hole size ratios, b/a. The effective plate volume, v_e, per unit length along the x_2-direction, corresponding to a finite hole size is greater than the actual plate volume per unit length along the x_2-direction of the plate. This effective volume is given as

$$v_e = \kappa v \tag{4.1}$$

where the non-dimensional factor κ is computed using the average stress

$$\kappa = \frac{\sigma_{\text{avg}}}{\sigma_0}\,. \tag{4.2}$$

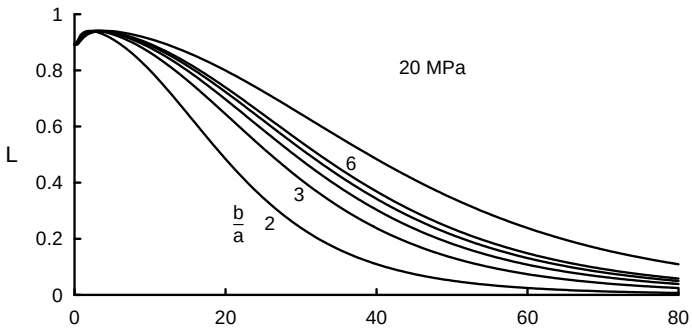

Figure 7. Reliabilities as functions of plate volume ratio, ρ, for various hole size ratios, b/a, subjected to applied stress $\sigma_0 = 20$ MPa

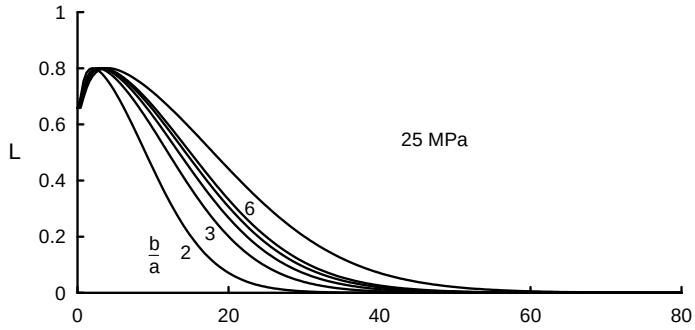

Figure 8. Reliabilities as functions of plate volume ratio, ρ, for various hole size ratios, b/a, subjected to applied stress $\sigma_0 = 25$ MPa

Table 1 presents the conventional stress concentration factor, $k = \sigma_{\max}/\sigma_0$ and the effective volume ratio κ.

Table 1. Stress concentration factor, k, and effective volume factor, κ, for various plate width to hole diameter ratios, b/a

	b/a					
	2	3	4	5	6	∞
k	4.141	3.444	3.224	3.133	3.082	3
κ	1.999	1.501	1.339	1.256	1.204	1

Because this effective volume, v_e, is greater than the actual volume, v, the size effect (larger size is weaker) is apparent. As the hole size ratio, b/a, increases, the curves approach the reliability function of a solid plate.

5. Conclusions

Experimentally observed size effects have been modelled by a modified hyperbolic function that indicates strength variations as a function of stressed volume. Applied to the reliability of porous materials, these reliability functions also show the effects of volume. The analysis of plates containing circular holes of various sizes indicates that as the plate width to hole diameter ratio increases, i.e., as the hole becomes smaller, the reliability of the plate increases. This is due to the fact that the critical stressed volume around the hole is also smaller. Experiments are needed in order to determine the coefficients of the size effect relationships.

References

1. Weibull, W.: *A Statistical Theory of the Strength of Materials*, Proceedings of the Royal Swedish Institute for Engineering Research, No. 151, Stockholm, (1939).
2. Weibull, W.: *A Statistical Distribution Function of Wide Applicability*, ASME Journal of Applied Mechanics, 18, (1951), 293.

3. Davies, D. G.: *The Statistical Approach to Engineering Design of Ceramics*, Proceedings of the British Ceramic Society, 22, (1973), 429-452.
4. Stanley, P., Fessler, H. and Sivill, A. D.: *An Engineer's Approach to the Prediction of Failure Probability of Brittle Components*, Proceedings of the British Ceramic Society, 22, (1973), 453-487.
5. Trantina, G. G. and deLorenzi, H. G.: *Design Methodology for Ceramic Structures*, ASME Journal of Engineering for Power, 99 (4), (1977), 559-566.
6. Stanley, P. and Margetson, J.: *Failure Probability Analysis of an Elastic Orthotropic Brittle Cylinder Subjected to Axisymmetric Thermal and Pressure Loading*, International Journal of Fracture, 13, (1977), 787-806.
7. Margetson, J.: *Failure Probability Evaluation of an Anisotropic Brittle Structure Derived from a Thermal Stress Solution*, in Thermal Stresses in Severe Environments, D. P. H. Hasselman and R. A. Heller, eds., Plenum Press, New York, (1980), 503-519.
8. Heller, R. A., Thangjitham, S., and Yeo, I.: *Size Effects in Brittle Ceramics*, AIAA-90-113, Proceedings of the 31st AIAA/ASME/ASCE/ASC Structures, Structural Dynamics, and Materials Conference, Long Beach, CA, (1990).
9. Bažant, Z. P. and Kazemi, M. T.: *Size Effect in Fracture of Ceramics and Its Use to Determine Fracture Energy and Effective Process Zone Length*, Journal of American Ceramic Society, 73 (7), (1990), 1841-1853.
10. Mazars, J., Pijaudier-Cabot, G. and Saouridis, C.: *Size Effect and Continuous Damage in Cementitious Materials*, International Journal of Fracture, 51, (1991), 159-173.
11. Bažant, Z. P. and Planas, J.: *Fracture and Size Effect in Concrete and Other Quasibrittle Materials*, CRC Press, Boca Raton, Florida, (1997).
12. Hoshide, T. Murano, J. and Kusaba, R.: *Effect of Specimen Geometry on Strength in Engineering Ceramics*, Engineering Fracture Mechanics, 59 (5), (1998), 655-665.
13. Labuz, J. F. and Biolzi, L.: *Characteristic Strength of Quasi-Brittle Materials*, International Journal of Solids and Structures, 35, (31-32), (1998), 4191-4203.
14. Guinea, G. V., Elices, M. and Planas, J.: *Assessment of the Tensile Strength through Size Effect Curves*, Engineering Fracture Mechanics, 65, (2000), 189-207.

Notes for Contributors

to the Journal of Computational and Applied Mechanics

Aims and scope. The aim of the journal is to publish research papers on theoretical and applied mechanics. Special emphasis is given to articles on computational mechanics, continuum mechanics (mechanics of solid bodies, fluid mechanics, heat and mass transfer) and dynamics. Review papers on a research field and materials effective for teaching can also be accepted and are published as review papers or classroom notes. Papers devoted to mathematical problems relevant to mechanics will also be considered.

Frequency of the journal. Two issues a year (approximately 80 pages per issue).

Submission of Manuscripts. Submission of a manuscript implies that the paper has not been published, nor is being considered for publication elsewhere. Papers should be written in standard grammatical English. Two copies of the manuscript should be submitted on pages of A4 size. The text is to be 130 mm wide and 190 mm long and the main text should be typeset in 10pt CMR fonts. Though the length of a paper is not prescribed, authors are encouraged to write concisely. However, short communications or discussions on papers published in the journal must not be longer than 2 pages. Each manuscript should be provided with an English Abstract of about 50–70 words, reporting concisely on the objective and results of the paper. The Abstract is followed by the Mathematical Subject Classification – in case the author (or authors) give the classification codes – then the keywords (no more than five). References should be grouped at the end of the paper in numerical order of appearance. Author's name(s) and initials, paper titles, journal name, volume, issue, year and page numbers should be given for all journals referenced.

The journal prefers the submission of manuscripts in LaTeX. Authors should prefer the standard LaTeX article style and are not recommended to define their own LaTeX commands. Visit our home page for further details concerning the issue how to edit your paper.

For the purpose of refereeing, two copies of the manuscripts should initially be submitted in hardcopy to an editor of the journal. The eventual supply of an accepted-for-publication paper in its final camera-ready form (together with the corresponding files on an MS–DOS diskette) will ensure more rapid publication. Format requirements are provided by the home page of the journal from which sample LaTeX files can be downloaded:

`http://www.uni-miskolc.hu/home/web/pumns/mechanics`

These sample files can also be obtained directly (via e-mail) from a member of the Editorial Board, Gy. Szeidl (Gyorgy.SZEIDL@uni–miskolc.hu), upon request.

Twenty offprints of each paper will be provided free of charge and mailed to the correspondent author.

The Journal of Computational and Applied Mechanics is abstracted in Zentralblatt für Mathematik and in the Russian Referativnij Zhurnal.

Responsible for publication: Rector of the Miskolc University
Published by the Miskolc University Press under the leadership of Dr. József PÉTER
Responsible for duplication: works manager Mária KOVÁCS
Number of copies printed: 200
Put to the Press on June 25, 2001
Number of permission: TU 02-760-ME **HU ISSN 1586–2070**

A Short History of the Publications of the University of Miskolc

The University of Miskolc (Hungary) is an important center of research in Central Europe. Its parent university was founded by the Empress Maria Teresia in Selmecbánya (today Banska Štiavnica, Slovakia) in 1735. After the first World War the legal predecessor of the University of Miskolc moved to Sopron (Hungary) where, in 1929, it started the series of university publications with the title *Publications of the Mining and Metallurgical Division of the Hungarian Academy of Mining and Forestry Engineering* (Volumes I.-VI.). From 1934 to 1947 the Institution had the name Faculty of Mining, Metallurgical and Forestry Engineering of the József Nádor University of Technology and Economic Sciences at Sopron. Accordingly, the publications were given the title *Publications of the Mining and Metallurgical Engineering Division* (Volumes VII.-XVI.). For the last volume before 1950 – due to a further change in the name of the Institution – *Technical University, Faculties of Mining, Metallurgical and Forestry Engineering, Publications of the Mining and Metallurgical Divisions* was the title.

For some years after 1950 the Publications were temporarily suspended.

After the foundation of the Mechanical Engineering Faculty in Miskolc in 1949 and the movement of the Sopron Mining and Metallurgical Faculties to Miskolc, the Publications restarted with the general title *Publications of the Technical University of Heavy Industry* in 1955. Four new series - Series A (Mining), Series B (Metallurgy), Series C (Machinery) and Series D (Natural Sciences) - were founded in 1976. These came out both in foreign languages (English, German and Russian) and in Hungarian.

In 1990, right after the foundation of some new faculties, the university was renamed to University of Miskolc. At the same time the structure of the Publications was reorganized so that it could follow the faculty structure. Accordingly three new series were established: Series E (Legal Sciences), Series F (Economic Sciences) and Series G (Humanities and Social Sciences). The latest series, i.e., the series H (European Integration Studies) was founded in 2001. The eight series are formed by some periodicals and such publications which come out with various frequencies.

Papers on computational and applied mechanics were published in the

Publications of the University of Miskolc, Series D, Natural Sciences.

This series was given the name Natural Sciences, Mathematics in 1995. The name change reflects the fact that most of the papers published in the journal are of mathematical nature though papers on mechanics also come out.

The series

Publications of the University of Miskolc, Series C, Fundamental Engineering Sciences

founded in 1995 also published papers on mechanical issues. The present journal, which is published with the support of the Faculty of Mechanical Engineering as a member of the Series C (Machinery), is the legal successor of the above journal.

Journal of Computational and Applied Mechanics

Volume 3, Number 1 (2002)

Contents

Preface 3–4

Contributed Papers

Péter BÉDA: A dynamic theory of material instability 5–13

Sung R. CHOI and John P. GYEKENYESI: Effect of load rate on ultimate tensile strength of ceramic matrix composites at elevated temperatures 15–26

Yura KABISH and Vasil LAVRENYUK: Investigation of the equations of motion in terms of displacements, constructed on the basis of the Lennard-Johns law, under the action of harmonic loading 27–35

Imre KOZÁK and Tamás SZABÓ: Calculation of the work done by deformation dependent tractions 37–49

Gennadiy LVOV and Sergey LYSENKO: Contact problem for the autofrettage of thick cylinders 51–60

István PÁCZELT and Attila BAKSA: Examination of contact optimization and wearing problems 61–84

Gábor STÉPÁN: Appell-Gibbs equations for classical wheel shimmy — an energy view 85–92

Surot THANGJITHAM and Robert HELLER: Volume dependent strength of porous materials and structures 93–101